Doctoral Dissertation
Doctoral Program in Metrology (33th Cycle)

New insight in biomedical measurements

...

Alessio Gullino
* * * * * *

Supervisors
Prof. Sabrina Grassini, Supervisor
Prof. Marco Parvis, Co-Supervisor

Doctoral Examination Committee:
Prof. Francesco Di Franco, Referee, Università degli Studi di Palermo
Prof. Lorenzo Ciani, Referee, Università degli Studi di Firenze

Politecnico di Torino
January 26, 2021

I hereby declare that, the contents and organisation of this dissertation constitute my own original work and does not compromise in any way the rights of third parties, including those relating to the security of personal data.

…….....

Alessio Gullino

Turin, January 26, 2021

Summary

This dissertation deals with new insight in biomedical measurements and applications. In particular, thin films technologies are employed for the developments of sensors and sterile biomedical tools. At this scope, a metrological approach is required for the study and evaluation of three topics for biomedical applications. First of all, the main topic faces the realization of sensors for breath analysis based on niobium oxide thin film obtained via plasma deposition. Then, the second topic deals with the deposition of silicon oxide thin film enriched with copper nanoparticles in order to obtain sterile tools with high barrier properties. Eventually, the last topic regards the effect of a controlled CO_2 atmosphere on the corrosion of a magnesium (Mg) alloy formed by yttrium and neodymium (WE43 alloy). Actually, the corrosion characterization of Mg alloys, for biomedical applications, requires a trustable methodology able to simulate in the best way a biological environment. The latter has been carried out during the research period at Monash University in the frame of Erasmus+/Partner Countries 2018/2019.

Starting from the main topic, it is focused on the development and characterization of sensors for breath test analysis, especially for the detection of acetone, ethanol and hydrogen. Nowadays, breath test measurements are gaining more importance since they allow to obtain fast responses avoiding invasive procedures. In fact, it is possible to diagnose several different diseases by detecting specific biomarkers from the human breath aerosol. Among the different gas sensor technologies, conductometric gas sensors are an interesting low-cost solution because of their small dimensions, which allow to implement them into portable measurement system devices. In this dissertation, conductometric gas sensors formed by a small alumina substrate (about 6 mm x 3 mm) are developed by depositing a small niobium oxide (NB_2O_5) thin film on it as sensing material. From a complete sensing characterization, noteworthy results in terms of sensitivity and selectivity have been obtained toward the detection of acetone and ethanol. The

sensitivity, observed by proposed sensors, allows to detect a linear response toward acetone in the concentration range from 1 ppm to 3 ppm making them suitable for breath analyser for diabetes diagnosis. In fact, it is well-known that diabetes can be correlate with acetone concentrations higher than 2 ppm inside the exhaled human breath. Furthermore, high selectivity is achieved; in fact, the sensors show responses only towards acetone and ethanol. The latter is not involved in metabolic human processes avoiding possible interference during the breath test, which could lead to false positive diagnosis. Furthermore, such niobium oxide thin film has been characterized toward ethanol sensing as well. The results exhibit quite good responses making such sensors suitable for ethanol analyser.

Moreover, sensors obtained by depositing NB_2O_5 enriched with platinum (Pt) nanoparticles have been developed in order to modulate the selectivity toward hydrogen detection. In fact, the Pt enrichment turns out in excellent responses toward H_2 at high concentrations, up to 80000 ppm. In addition, the selectivity shows interesting results since such sensors do not exhibit any responses toward others interferent gases.

The second topic is a proof of concept about the possibility to combine electrochemical impedance spectroscopy and inductively coupled plasma – atomic emission spectroscopy measurements for the evaluation of both corrosion protection effect and antifungal effect of SiO_x thin films enriched with copper nanoparticles obtained by plasma deposition. In fact, fungi and bacteria infections are still an important concern in the hospital environments, which could lead to clinical complications. Nevertheless, Cu has an interesting antifungal effect, and it can be employed for the realization of engineered thin films enriched with Cu nanoparticles, which can be gradually released by a tailored degradation of the film itself. The thin films have been obtained by plasma enhanced chemical vapour deposition for obtaining SiO_x thin films and, at the same time, by a magnetron sputtering in order to embedded Cu particles inside the SiO_x matrix. The analyses were carried out employing simulated body fluids as electrolyte and collecting 5 cc of solution every day in order to monitor the Cu release and comparing it with the results of EIS measurements. The preliminary results are promising and shows a specific correlation between the two techniques.

The third and last topic deals with the effect of CO_2 atmosphere on corrosion of a WE43 magnesium alloy in two different minimum essential medium electrolytes. Nowadays several studies face the possibility to tailor the corrosion of magnesium alloys in order to obtain a controlled bioreassorbtion of implants (e.g. stents). At this scope, a wide number of magnesium alloys have been characterized in simulated body fluids in order to simulate a biological environment.

Unfortunately, there is not a common agreement or specific guideline about the methodology to carry out the experimental set up, which can turn out to non-confrontable results. One of the aspect that is commonly ignored is the effect of CO_2 on the corrosion mechanism of magnesium alloys. In fact, CO_2, has an important role as buffering inside the human body, maintaining the pH at about 7.3. At this scope, the comparison between a controlled CO_2 atmosphere and an open-air environment on the corrosion of a WE43 alloy has been carried out, performing both long term and short-term measurements. The results highlight an important difference between the two cases since the corrosion mechanisms are affected both by the buffering effect and by the inhibition of the cathodic particles by the carbonates generated by the CO_2 controlled atmosphere.

To conclude, the interesting results, reported in this dissertation, highlight the importance of appropriate measurement techniques for the characterization of devices and materials for biomedical applications.

Acknowledgment

And I would like to thank my supervisors and all my office colleagues for the fantastic time spent together here in Torino and around the world.

A special thanks to Prof. Nicola Donato and Prof Giovanni Neri of Università di Messina for their collaboration on sensing characterization of the conductometric gas sensors.

I would like to acknowledge Prof. Nick Birbilis to give me the opportunity to join his group at Monash University and all the brilliant people that I met there, in particular my supervisors Dr Zhuoran Zeng and Dr. Mohsen Esmaily.

Thanks also to all the people met in Politecnico di Torino, in particular the "third floor guys" for the nice moments we shared together.

At the end, I would like to thank to my fantastic partner Luisa Racca, which has been by my side, helping me to face all the difficulty met during the whole PhD period.

To my parents

Contents

List of Tables

List of Figures

Introduction

A “metrological” approach, based on measurement methods and error evaluation, is of a paramount importance for the correct interpretation of the results obtained in several different fields. In particular, a metrological point of view is becoming important for biomedical purposes, where small measurement errors could not only affect the effective results, but also be dangerous for the human health.

In this dissertation, three examples, of the use of a metrological approach for biomedical applications, are exposed, all based on the application of plasma technology for the development of sensors and devices for biomedical measurements.

The main topic regards the development of novel breath sensors for acetone and ethanol detection. Breath test is an important tool for the diagnosis of several diseases since it is non-invasive and it can give fast response. It is based on the detection of specific biomarkers present inside the breath aerosol exhaled by the body. Such biomarkers can be put in correlation with the insurgence of diseases, but their concentration are quite low (from few ppm to ppb) thus a sensor with high sensitivity and selectivity is required. In this case, the proposed sensors are conductometric sensor, based on a sensing nano-composed Nb_2O_5 thin film, obtained by means of plasma deposition. Moreover, such thin film is further enriched with platinum nanoparticles, revealing a high sensing toward H_2.

The second topic deals with the possibility to involve two different measurements techniques (electrochemical impedance spectroscopy and inductively coupled plasma) in order to assess the effective antifungal and antibacterial effects of nanostructured thin films obtained via plasma enhanced chemical vapour deposition (PECVD). Such films are formed by two layers: the first one in pure copper and the second one in glass-like silica oxide (SiO_x) with copper nanocluster embedded in it.

The last topic has been carried out at during the period at Monash University in the frame of Erasmus+/Partner Countries. It is related on corrosion of magnesium

alloys employed in the fabrication of implants (such as stents). In particular, it is focused on the evaluation of the best condition to test such material, since in bibliography several case studies are present but there is not a defined method to evaluate its corrosion properties in the biological environment. For this reason the effect of CO_2, often not concerned during the corrosion tests, has been assessed on the corrosion on a magnesium alloy formed by yttrium and neodymium called WE43.

Chapter 1

Nb_2O_5 based sensors for breath analysis

This chapter partially contains materials from previously published work of the author [1][2][3]

Aim of this chapter is to provide a description of novel gas sensors for breath analysis highlighting their peculiarity to be able to detect several different diseases being totally no-invasive, in particular regard to a specific sensor typology called conductometric sensor, based on Metal Oxide (MOX) thin film. Thereafter, the realization and the characterization in terms of microstructure and chemistry of the proposed sensor are provided.

In particular, this thesis chapter deals with realization of MOX sensors obtained by plasma deposition of niobium penta-oxide (Nb_2O_5) thin film with high sensibility to detect gases as acetone and alcohol. All these compounds have a great medical relevance for health monitoring, and their detection can lead to a fast diagnosis avoiding further invasive analysis. The chosen of Nb_2O_5 as sensing film was led by its interesting properties about the electrical transport properties [4] as well as the sensing performances [5][6].

The correlation between the breath aroma and the possibility of a disease diagnosis has been well known since ancient times. Actually, first testimonies on the concept that the human breathe can be a health indicator are reported in the writings of Hippocrates. Moreover, always in ancient times, the breath smell has been correlated to “evil humours”, nowadays recognized as liver or renal diseases, bacterial infection or diabetes.

Nowadays breath analysis is becoming an important diagnosis method for the evaluation and monitoring of health-status and disease, due to it is non-invasive approach, which results in a more comfort for the patient. In particular, MOX sensors achieve interesting features such as an instant results response as well as the possibility to customize the sensor by using different thin films. For these reasons, several works have been published in recent years, employing and characterizing different MOX thin film, sometimes enriched by noble metals, as reported in the next sections.

Despite such rich bibliography, there is a lack in study of Nb_2O_5 thin layer, which is an interesting material for the realization of sensor for breath test, in

particular toward the detection of acetone and ethanol [7]. In this work, two different kind of sensors are proposed, based on:

1. *Nb_2O_5 thin film*
2. *Nb_2O_5 thin film enriched with platinum (Pt) nanoparticles*

Several different prototypes were developed by employing different plasma deposition parameters in order to detect the sensors with the best performances. In fact, the deposition parameters can drastically affect both the morphology and the thickness of the deposited film. In this dissertation are exposed the results about the sensors that show the best performances.

In this chapter are also exposed the thin film characterizations obtained by means of SEM analyses to assess the microstructure and X-Ray photoelectron spectroscopy (XPS) to evaluate the film chemistry.

1.1 Breath analysis for medical diagnosis

Among the several diagnosis tools for medical screening, breath analysis is gaining importance and interesting since it allows the prediction and the monitoring of some diseases by means of a non-invasive and painless approach, which leads to a fast diagnosis without further stress for the patient [8][9][10][11]. Actually, samples for such analysis are easy to collect and require only a simply blow of the patient inside of a specific inlet avoiding painful access to the body. This is an important aspect, for people affected by debilities like elders, especially if they have to effort daily monitoring of chronic diseases, such as diabetes. Moreover, breath does not need to be disposed after the analyses unlike other samples as blood or urine, leading to reduction of biohazard waste. Additionally, breath analysis procedures are easier, making it less expensive with respect to other conventional diagnostic techniques. Another important point, worthy to be highlighted, is the rapid process-time of such test which can give a real time monitoring, while several hours are required for other kind of tests.

For a better comprehension of the principles on which breath test is based, it is important giving some information about the human breath composition and how it can be employed for medical diagnosis.

First of all, for every single exhaled breath thousands of different volatile molecules and compounds are released outside the human body in an aerosol formed by a heterogeneous mixture of gases having different nature [12][13]. These can be catalogue as follow:

- *Inorganic gases* – they represent the breath bulk matrix, which is mainly formed by nitrogen (N_2), oxygen (O_2), carbon dioxide (CO_2), water vapour and other inert gases.
- *Volatile organic compound (VOCs)* – such fraction is formed by thousands of different compounds contained in trace inside the inorganic bulk. Among the most important VOCs there are acetone,

ethane, isoprene and they have different concentration in the range from ppm to ppt.

- *Non-volatile substances* – they can be isoprostanes, peroxynitrite and cytokines.

Moreover, these gaseous species can have both exogenous and endogenous origins, which means that a portion is inhaled from the external environment while the other part can be produced by the human body metabolism respectively. These last are generally called biomarkers, and play an important role for the detection of possible diseases because they are the result of metabolic processes inside the human body and an unjustified variation of their typical concentrations can be correlated to a body dysfunction, providing evidences of specific health illness [14]. Table 1 resumes the main important biomarkers and the diseases correlated to their increasing in term of concentration.

Table 1: Examples of biomarkers and related diseases.

Biomarkers	**Diseases**
Acetone	Diabetes, lung cancer, dietary fat losses, brain seizure
Hydrogen	Bacteria infection, lactose and fructose intolerance, liver dysfunction
Pentane	Liver diseases, breast cancer, oxidative stress, asthma
Ethane	Oxidative stress, vitamin E defiance, breast cancer
Nitric oxide	Asthma, lung injury and/or infection, lung cancer
Ammonia	Kidney failure, cirrhosis, hepatitis, halitosis asthma
Methane	Intestinal problems, colonic fermentation
Hydrogen sulphide	Airway inflammation
Carbon disulphide	Schizophrenia, coronary disease
Formaldehyde	Breast cancer

Being involved in determined body processes the biomarkers concentration, inside the breath aerosol, is fixed in a range of few ppm. In Table 2, it is exposed a typical breath composition exhaled by a healthy adult person, but it is important to say that such concentrations can be different for each individual case. Until now, it has been possible to identify the arising of anomalous concentrations of one or more biomarkers and correlate them with the insurgence of specific diseases and/or dysfunctions. An example is the detection of high concentrations of acetone, which

is commonly attributed to the presence of diabetes [15]. The reason behind this anomalous behaviour has a metabolic dysfunction explanation, since the inadequate insulin level results in two different metabolic malfunctions, which involve an increasing in glucose concentration in blood. Subsequently the acetone is exchanged from the blood to the alveolar air increasing its concentration inside the breath aerosol.

Other important cases where breath analysis can be usefully applied is for diagnosing gastro-enteric diseases by means of the detection of hydrogen [16][17], or a possible kidney failure by presence of ammonia (NH_3) [18].

Table 2: Human breath details and typical range concentrations.

Exhaled breath	**Concentration**
Nitrogen	78%
Oxygen	16%
Carbon Dioxide	4-5%
Carbon monoxide	0-6 ppm
Ammonia	0.5 ppm – 2 ppm
Acetone	300 ppb – 900 ppb
Hydrogen sulphide	0- 1.3 ppb
Nitric oxide	1 ppb – 20 ppb
Carbonyl sulphide, pentane and ethane	0-10 ppb
Relative humidity (oral exhalation)	91% - 96%
Temperature	34 °C – 36 °C

To sum up breath analysis possesses intriguing properties, which makes it an important tool for biomedical applications. It is completely safe and non-invasive, suitable for the diagnosis of several kind of diseases and metabolic dysfunctions. In conclusion, the final purpose of a breath analysis test is to identify one or more specific biomarkers, from the breath aerosol, and provide information about its concentration, in order to understand if the conditions are suitable for a disease evidence.

Despite these advantages and the continuous research of more performant sensors for breath analysis, several drawbacks limit the effective use of such test in real live medical applications [8]. First of all, there is a lack on standard analytical methods, which lead to a low accuracy in quantification of the interested biomarker, thus in a high range variation of results affecting the real value concentration. The main consequence is the unacceptable reliability of the obtained results that can provide a wrong diagnosis. As said before, the breath aerosol is a heterogeneous system formed by thousands of different compounds and most of them have a concentration lower than few ppb. Nowadays is still a challenge to obtain suitable results from the detection of such compounds for both sensibility and selectivity due to a limited sensing by the available apparatus. Moreover, for some methods sample preconcentration is required with a relative increasing of the final analysis

cost. Furthermore, the similarity (in term of chemistry and structure) of two or more biomarkers can interfere and lead to a single signal from the detector then causing a possible false diagnosis.

1.2 Breath sensors for human health diagnosis

Several metabolic processes inside the human body generate many different endogenous compounds, which are exchanged from the blood to the alveoli air, thus exhaled from the breath. Such compounds lay in a specific concentration range (see Table **2**) therefore an unjustified variation can be a disease insurgence symptom.

Unfortunately, a correct detection of the desired biomarkers is limited by the heterogeneous composition of the breath aerosol, formed by several compounds inside combined by their very low concentration (from ppm to ppb). Therefore, for a reliable diagnosis high selectivity and sensibility are mandatory.

In recent years, several breath sensors have been developed and part of them are already employed in real medical applications; they are based on different selective technologies.

More details regarding the main techniques already involved in breath analysis are provided in next sub-sections, especially focusing on conductometric metal-oxide gas sensors, which are the typology, employed in this dissertation.

1.2.1. Gas chromatography based techniques

Gas chromatography (GC) is a consolidated technique widely employed in several fields where high sensibility and selectivity are required. A schematic block diagram is showed in Figure 1. The instrument is composed by two main components: the chromatographic column and the detector. The mixture of pre-collected breath sample is forced to pass through the chromatographic column, by means of an inert carrier gas (generally He), allowing the separation of the different compounds. The separation mechanisms, which occur inside the column, are related to the nature of the used substrate coating. Non-polar substrates (e.g. silicon) can provide a separation in according to the different boiling points of the compounds. Otherwise, the GC column can be characterized by a polar coating and the separation is due to the different interaction among the compounds and the column itself.

The separated compounds are flowed toward the detector in order to recognize the different VOCs. The detectors generally combined with GC, they are Mass Spectrometry (MS), Flame Ionized Detection (FID) and Ion Mobility Spectroscopy (IMS).

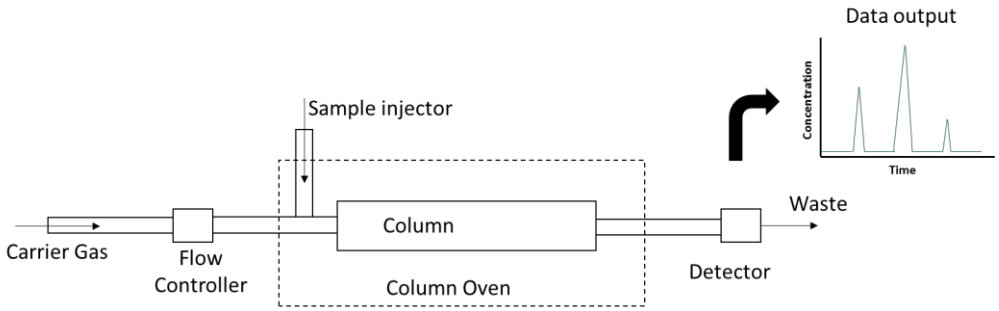

Figure 1: Schematic block of a gas chromatography system.

GC-MS method is currently employed as standard technique for the VOCs assessment in exhaled human breath [19] and provides information about the mass-to charge (m/z) values obtained by the ionization of atom and/or molecules. First, it is necessary to ionize the compounds that can be carried out by several different methods [20]. Thus, the ionized compounds are accelerated toward a magnetic field, and deflected in function of their m/z ratio. In this way, The VOCs detection can be identified by the fragmentation pattern, quantifying the measured selected daughter ions [21].

FID is a technique introduced the first time in New Zealand in 1958 with the goal to identify carbon-based compound [22]. The method is based on the production and the analysis of ions by burning the organic compounds by means of a hydrogen flame. Burning pure hydrogen is mandatory for this kind of method since it does not produce ions that can lead to a base line with high noise. Two electrodes are located close the flame and maintained at a suitable potential. The ionized compounds generate by the flame generate an electric current that is proportional to the ion concentration. In this way, it is possible to correlate the electrical signal to the effective VOCs concentration. This technique is characterized by high sensitivity and selectivity.

IMS method is employed in several fields thanks to its high operation speed and high sensitivity [23]. It involves a drift tube, having a suitable electric field, which acts on the ionized compound mobility in function of their mass, charge size and shape. In this way, it is possible to measure the VOCs concentration according to the velocity drift that is characteristic of every compounds.

1.2.2. Proton-transfer reaction mass spectroscopy

Proton-transfer reaction mass spectroscopy (PTR-MS) is a technology developed in the mid-1990 with the specific aim to detect and measure VOC. Nowadays the main employed method to measure and quantify VOCs is by gas chromatography because of its high selectivity and sensitivity. Nevertheless, it is worthy to be noted that such technique suffers some drawbacks such as it takes several minutes before completely separating the different components as well as it necessities to preconcentrate the sample if the desired VOC analyte is in traces. PTR-MS methods is based on chemical ionization of the target organic fraction,

avoiding the inorganic one, by proton transfer. In this way it is possible to eliminate the inorganic fraction from the detected count improving the selectivity of the process [24].

A schematic block diagram of such technique is exposed in Figure 2. The proton source is generally H_3O^+ generated by the ionization of aqueous vapour by the primary ion source. Such ion source is normally a hollow-cathode discharge which guarantees an efficiency protons generation (> 99.5%). The generated protons are led toward the drift tub where can approach the VOC and the proton-transfer reaction occurs as follow in eq.1

$$VOC + H_3O^+ = VOCH^+ + H_2O \qquad \text{eq. 1}$$

The drift tube is characterized by an electric field, generated by different ring electrodes put in series. The protonated VOC are accelerated by the electric field trough the detector that is a mass spectrometer (already mentioned in 1.2.1)

It is important taking in account that also the aqueous vapour that does not generate protons is flowed toward the drift tube leading the formation of $H_3O^+(H_2O)_n$ cluster ions then such peak can appear in mass spectra.

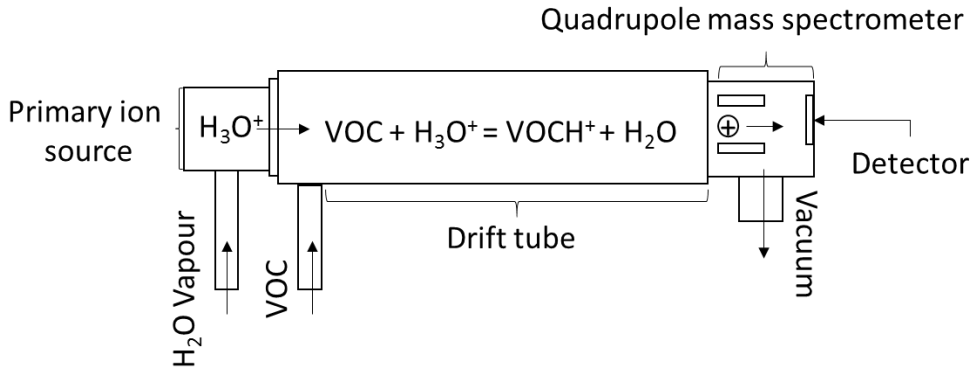

Figure 2: Schematic block of a proton-transfer reaction mass spectroscopy system.

The efficiency and sensitivity of such technique has been demonstrated by Boschetti et al.[25], by the detection of 30 VOCs at low concentrations (ppt level)

1.2.3. Laser spectroscopy based techniques

Laser spectroscopy based techniques are becoming an important breath analysis test because of their high resolution, which allows the detection of VOC analytes at low concentration [26]. Moreover, unlike gas chromatography, it does not need any sample preparation allowing a real-time monitoring (sub-second time resolution) associated with the possibility to detect one or more VOCs with concentration in the range of part-per-billion (ppb). Such method can be organized in two macro groups that differ by the laser response measured by the detector. Such groups are:

- *Laser absorption spectroscopy*
- *Laser photoacoustic spectroscopy*

Generally, laser absorption spectroscopy techniques are based on a laser beam, which is absorbed by the gaseous VOC molecules. The adsorption follows specific rules since it is possible to assign a specific wavelength to an appropriate specie. The detector is able to measure the absorbed amount from the laser beam, and then quantify the effective amount of the determined species. Among these techniques, the tunable diode laser, multipass absorption spectroscopy and cavity-enhanced absorption spectroscopy can be cited.

In the case of laser photoacoustic spectroscopy, the background signal is missing in absence of VOCs and the VOC detection is not based on the decrease in intensity by the laser beam, but on measurement of acoustic wave generated by the analyte after the laser excitation. The VOCs are excited by a laser beam characterized by infrared wavelength. In this way, the energy level de-excitation passes through collision phenomena (the florescence effects have long lifetime by infrared excitation) causing an increment in gas temperature. Therefore, it is possible to change the gas temperature periodically, by means of a laser source modulation. Consequently, also the gas pressure undergoes periodical changes, generating acoustic waves that can be detected and measured by a devoted microphone.

1.3. Conductometric Metal Oxide (MOX) gas sensors

Nowadays, conductometric metal oxide gas sensors are one of the most studied kind of sensor for gas detection [5] [27] . The reason behind this high interest can be correlated to their low cost production as well as the possibility to customize the sensing material toward the detection of suitable target gases [28] [29]. In this way, the obtained sensors can be addressed to detect a large number of gasses, improving their selectivity and the sensibility. Therefore, this group of sensors are widely investigated and employed in several different field such as in biomedical applications as breath test sensors [30].

In Figure 3, a generic conductometric gas sensor structure is exhibited. It is formed by a sensing thin film, which generates a bridge between two electrodes. The sensing film is generally a metal oxide characterized by high resistance. Such resistance can be modulated by the absorption of a specific gas by the film itself. In this way, it is possible to correlate the gas detection with the measured resistance. Nevertheless, the sensing film resistance can reaches values higher than GΩ at room temperature, making impossible the measurement without involving high performance ohmmeter. In addition, the high resistance generates high background noise affecting the measurement results. For avoiding this problem, high working temperature are required (between 200 – 500 °C) in order to decrease the sensing film resistance. Thus, a heater is required on the sensor bottom side, in order to lead and maintain the suitable working temperature during the measurements.

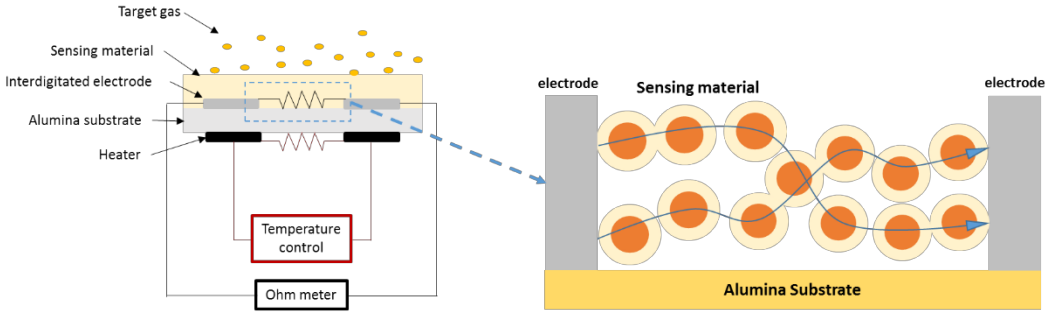

Figure 3: Representation of a conductometric gas sensor based on sensing thin film.

Several different sensing films are reported in literate. They can have different origins, such as polymer, nanotube or metal oxide. In this work, a focus on metal oxide sensing film is provided. Such films are usually a nanostructured n-type metal oxide formed by several different grains assembled in porous or compact structures.

The surface is not uniformed but it is characterized by vacancies and broken bonds that can be involved as ionosorption sites by the environmental gas. In open air, oxygen species (O_2^-, O^- and O^{2}) can be adsorbed by the film surface, extracting electrons , from the conduction band (E_c) as described below [31]:

$$O_2 + e^- \leftrightarrow O_2^- \qquad \text{eq. 2}$$

$$O_2^- + e^- \leftrightarrow 2O^- \qquad \text{eq. 3}$$

$$O^- + e^- \leftrightarrow O^{2-} \qquad \text{eq. 4}$$

In particular, O_2^- species are commonly adsorbed at temperature lower than 200 °C while O^- and O^{2-} adsorption is promoted at higher temperature[32]. However, such electron extraction arises a depletion zone around the grain and a subsequent generation of a potential barrier among the grain boundaries, as exposed in Figure 4, which act as obstacle for the charge carriers decreasing the film conductivity.

The depletion layer thickness is described by eq. 5 as follow:

$$w = \sqrt{\frac{\varepsilon_r \varepsilon_0 e V_{surface_s}}{n_b}} \qquad \text{eq. 5}$$

Where: ε_r is the relative permittivity of the MOX film, ε_0 is the dielectric constant of vacuum, $eV_{surface}$ is the band bending, and n_b is the charge carrier density.

The presence of a reducing gas (e.g. acetone or H_2) can modulate the depletion zone thickness by affecting the charge carrier density. In fact, such gas can remove the absorbed oxygen from the film surface by a competitive ionosorption process and acting as donors for these n-type MOX. As consequence, a reduction of the depletion zone thickness and relative decrease of the potential barrier occurs. Thus,

the film conductivity improves in function of the reducing gas absorption onto film surface.

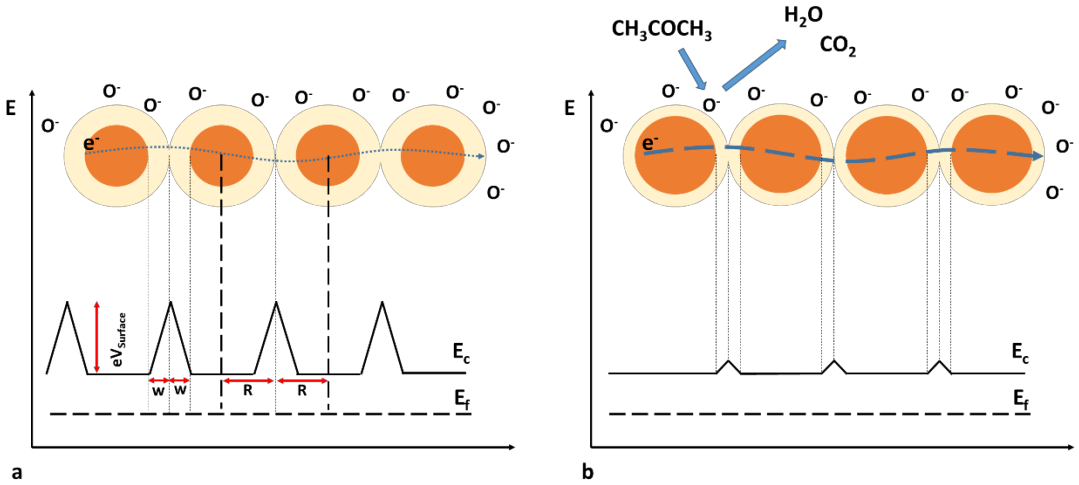

Figure 4: Representation of the deplation zone and related energy gap in open air (a) and in presence of the reducing gas (b).

The film sensing performance can be established by the sensitivity (S) parameter, which can be correlated with the sensor response. It is defined as follow:

$$S = \frac{R_a}{R_g} \qquad \text{eq. 6}$$

Where: R_a is the sensor resistance in presence of reference gas and R_b is the sensor resistance with the presence of the target gas.

The sensing response can be affected by several different factors; one of them is the grains dimension [30]. In fact, as exhibit in Figure 5, their dimension can act on the film conductivity mechanism. In particular, three cases can be detected:

- *Grain boundary control* – when the grain diameter is much higher than the depletion zone thickness, the conductivity of the film is controlled by the Shottky barriers at the boundaries.
- *Neck control* – it arise when the depletion zone is comparable to the grain dimension. In this case, the conductivity is controlled by the necks presents between each grain.
- *Grain control* – when the grain size is smaller than the depletion zone, the conductivity of the film is controlled only by every single grains.

It is clear that it is important to control the morphology during the sensing film realization. In particular, a nanostructured morphology is suggested in order to obtain sensor with higher response. Moreover, the sensing mechanism occurs onto film surface, thus thin films or films having high free surface (e.g. with high porosity or with columnar morphology) are required with respect to thick film characterized by high ratio between bulk and surface.

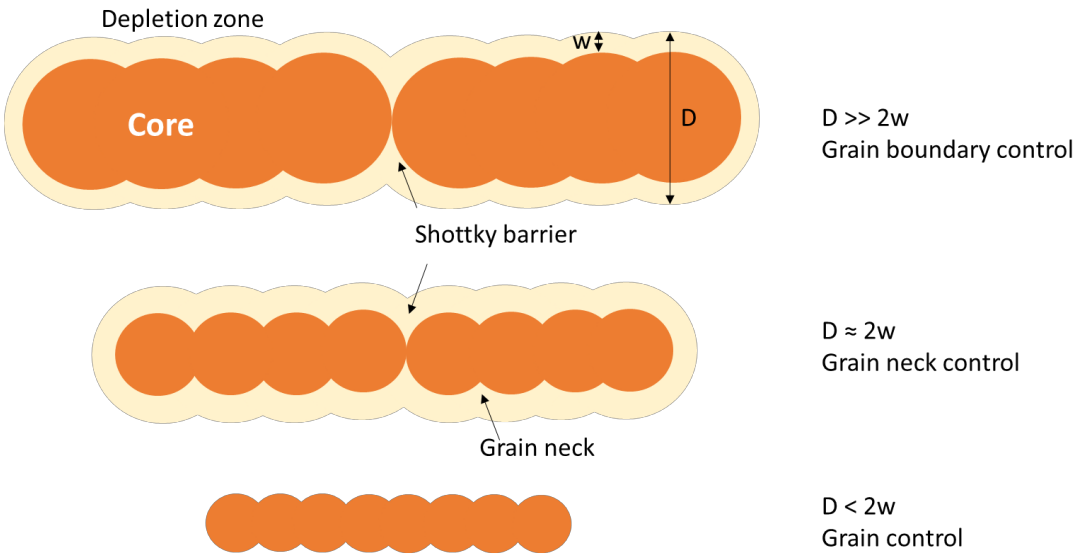

Figure 5: Effect of grains dimension on film conductivity mechanism.

As said before, the temperature control is extremely important in this kind of sensors since the film resistance is lower at higher temperature. Nevertheless, the temperature can also affect the absorption and desorption of the gases from the film surface. In fact, the temperature affects the absorption reaction rate, improving the reactivity increasing the temperature. However, a higher temperature generates an amount of thermal energy enough to break the bonds between surface and gas. Therefore, the MOX sensitivity is strongly affected by the working temperature and it is important to find out the optimal one. In Figure 6-a is exposed the typical bell-shape dependence where the sensitivity increases gradually, because of the improving in reaction rate, until reaching the optimal temperature, then it starts to decrease due to the low penetration depth by the gas. The optimal temperature is the temperature where these two effects are balanced.

The surface reaction between the film and the gas depends by the nature of the sensing film and the target gas themselves. Therefore can be different optimal temperature in function of the system (film and gas) investigated as showed in Figure 6-b

In order to improve the response, the sensor thin films are often enriched by noble particles. Actually, such particles play an important role in the generation of surface oxygen vacancies, which cause a modification of the electronic properties of the thin film. In fact, it causes a decrease of the surface potential barrier stimulating the chemical interaction between the thin MOX layer and the target gas [33] [34] [35]. Adding noble nanoparticles can also enhance the sensor response by a chemical effect called-spill over phenomenon [35] [36] [37]. Such particles act as catalytic site, promoting the adsorption and dissociation of oxygen from the atmosphere into atomic species (Figure 7). After that, the new species migrate toward the MOX thin film causing an increase of the depletion zone by extracting further electrons from the conduction zone. Nevertheless, the catalytic effect,

provided by the noble particles, acts also toward the target gas which will be dissociated and easily provides electrons into the conduction band. Therefore, a noteworthy decrease of the depletion zone is observed, resulting in a lower sensor resistance.

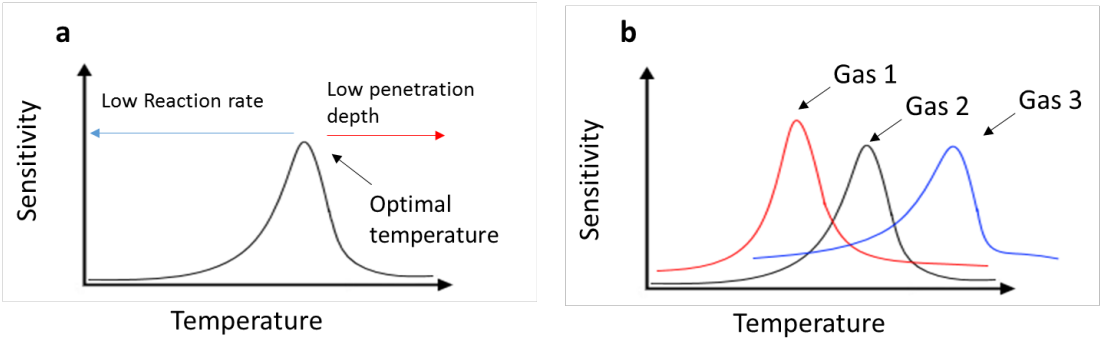

Figure 6: Typical temperature effect on conductometric gas sensors (a) and dependence of different target gas on the optimal working temperature (b).

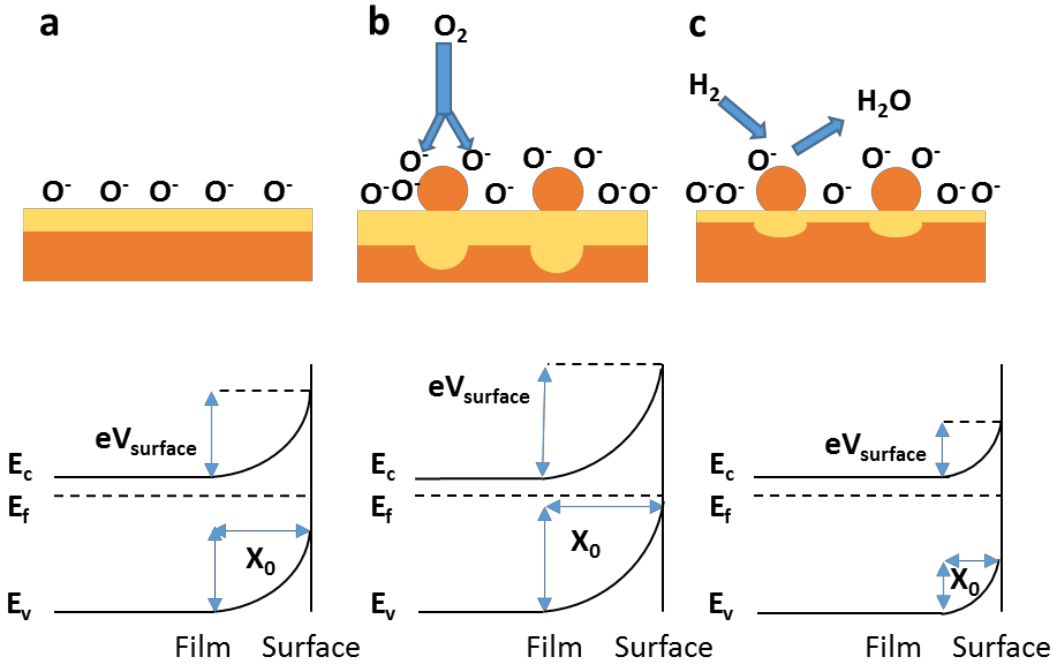

Figure 7: Surface film without noble particles (a), surface film enriched with noble particles and spill-over effect (b), surface film enriched with noble particles in presence of reducing gas (c).

1.4. Plasma Deposition of metal oxide films for gas sensors

Given its high number of advantages, such as high deposition rate, high purity film, high substrate coverage and adhesion as well as the possibility to sputter a large number of metals and compounds, magneto sputtering plasma deposition

gained importance in several fields and, nowadays, it is largely employed for several industrial applications [38] [39] [40].

Such technique is also involved for the realization of nanostructured thin film for the realization of conductometric sensor sensing materials. Actually, it can achieve thin films with high thickness uniformity and, modulating the process parameters during the deposition, it is also possible to obtain porous films [41] [42] or to achieve different structures [43]. Moreover, complex structures composed by different layers, are easily achieved. In fact, it is possible to perform more depositions in order to enrich the film with noble particles (e.g. platinum or palladium) [37] [44] or with other transition metal particles [34].

Magnetron-sputtering plasma deposition is based on ionic bombardment of a cathodic electrode (target) caused by a plasma glow in a low-pressure deposition chamber. The substrate, on which the film will grow on, is placed onto the anodic electrode. The two electrodes are connected to a power supply that provides a proper voltage (DC or AC) able to generate and confine the plasma discharge close the cathodic electrode. The generated ions are accelerated by a magnetic field toward the target and the collision extracts material (sputtering) that will deposit onto the substrate. It is clear that the target electrode has to be composed by the required material. Moreover, the target bombardment leads the formation of secondary electrons that have an important role to maintain the plasma glow. The sputtered atoms have to be able to reach and adhere the substrate to be coated avoiding any collision with other molecules along their path. Therefore, a pumping system, to guarantee low pressure, is required.

Magnetron sputtering is characterized by the employment of magnetrons, which create a magnetic field able to constrain the emitted electrons close to the target. In particular, a pole is located in the centre of the target while the other pole is arranged as a ring along the target perimeter. Such arrangement allows to increase the collision probability against the target, thus improve the deposition rate. The magnetrons configuration and position play an important role to tuning the magnetic field and the distribution of the plasma discharge [38]. They are generally arranged in three configuration that are summarized in Figure 8 and consist in:

- Balanced magnetron sputtering – the two magnetron poles have almost the same strength; generating flux lines close to the target. In this way the plasma glow is confined in the target proximity and only small plasma density is in contact with the substrate. Then, the ion current at the substrate is generally lower than 1 mA/cm^2. This configuration is not suggested for the realization of dense films.
- Unbalanced magnetron-sputtering, type 1 – in this configuration the magnetron pole located in the centre is stronger than the external ring one. In this way, the field lines are directed toward the chamber walls causing the presence of low current density at the substrate.
- Unbalanced magnetron-sputtering, type 2 – the outer magnetron is characterized by higher strength with respect to the centre one. In this

case, the flux lines are no longer confined close the target zone then they can flow toward the substrate increasing the ion current density.

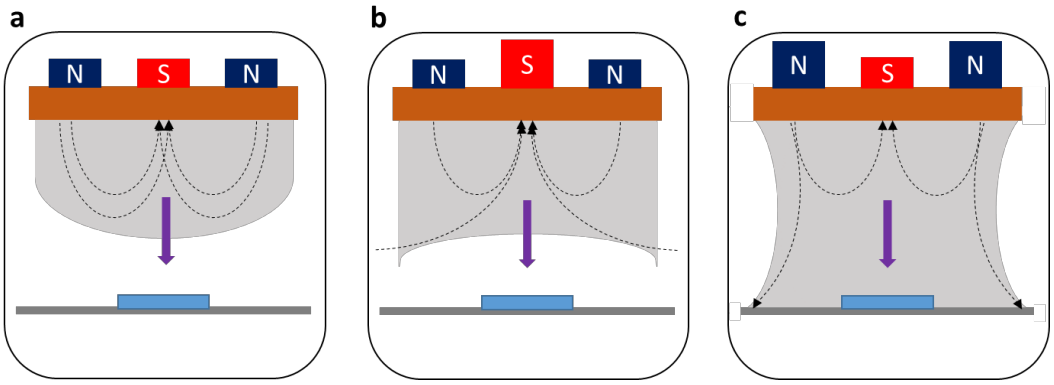

Figure 8: Balanced magnetron sputtering configuration (a), Unbalanced magnetron-sputtering type 1 (b), Unbalanced magnetron-sputtering type 2 (c).

The plasma discharge is generated by the ionization of an inert gas properly flowed inside the chamber. Such gas is usually a noble gas (e.g. neon or argon) that does not react with the target material avoiding undesired products. Nevertheless, an alternative magnetron sputtering method provides the deposition of a thin film formed by compounds or oxide by means of a reactive sputtering [45]. It consists to flow inside the chamber a second reactive gas (RG), which will react with the target generating the desired film. Unfortunately, the reactive sputtering is penalized by a low deposition rate with respect to the classic magnetron sputtering. The reactive gas injected inside the deposition chamber reacts with the metallic target generating the relative compound. In this situation, the target is called poisoned and the sputtering deal no longer with the pure metal but with the relative compound, causing the already mentioned low deposition rate. This effect is strongly affected by the reactive gas flow inside the chamber as exposed in Figure 9. Low RG flow reflects in a really low increase in reactive gas partial pressure (P_{RG}) inside the chamber. In this situation, all the reactive gas is gattered by the sputtered metal and expelled from the chamber by the pump system. By increasing the gas flow until the transition point, the P_{RG} suddenly arise and the reactive sputtering occurs. At this point, the deposition rate decrease and further RG flow will linearly increase the P_{RG} without affecting the deposition rate itself. The transition point is reached when the RG flow is enough to compensate the sputtered metal from the target electrode and the poisoning arise.

When the gas flow is decreased, the P_{RG} does not follow the previous path until the transition point, but it decrease at lower RG flow values and the metallic sputtering is delayed. The reason behind this behaviour can be found by the presence of compound that remain on the target surface not allowing to sputter the pure metal. After the complete compound removal the transition between reactive and metallic sputtering can occur. This behaviour is called hysteresis and it is an undesirable effect since next to the transition point it can prevent the $MeRG_x$

compound film with stoichiometry x according to the used RG as well as the arise of unstable deposition.

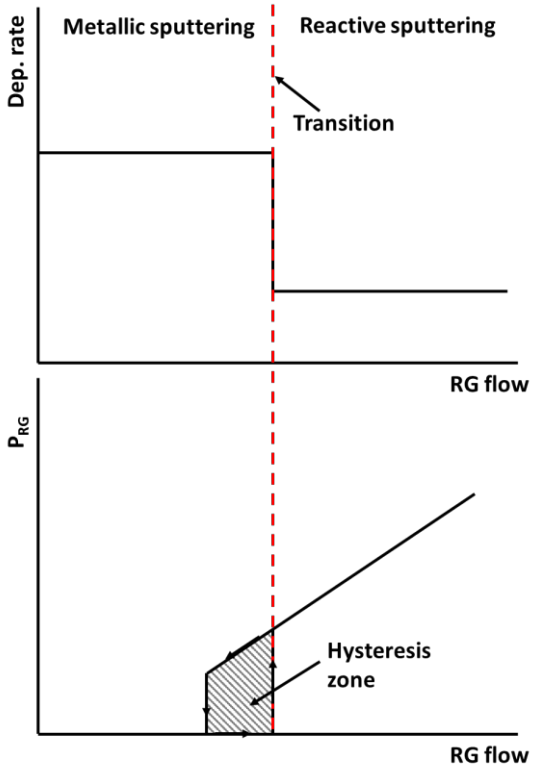

Figure 9: Transition between metallic sputtering and reactive sputtering in function of RG flow.

1.5. Sensor prototype realization

1.5.1. Proposed conductometric sensors

All the sensors proposed in this dissertation are generally formed by an alumina substrate characterized by a couple of interdigitate electrodes (IDEs) on the top side and a heater on the bottom side, both in platinum screen-printed, as exposed in Figure 10. The heater located on the bottom face plays an important role for such kind of sensor since, as reported in section 1.3, metal oxide sensors (MOX) work at high temperature (from 100 °C to 600 °C). Therefore, a heater is required to set and maintain the working temperature of the sensor. In particular, it should guarantee a stable temperature value during the entire measurement time. For those reasons, even the heater has been characterized in section 2.3.

Regarding the interdigitate electrodes, they provide the effective sensor response, since they allow the measurement of the resistance modulation, of the sensing material, by the target gas. As a matter of fact, the sensing material is deposited, by plasma deposition, on the interdigitate area only, on an area of about 10 mm^2, guaranteeing the contact free in order to be able to link the sensor with the measurement apparatus.

Two different sensing films are proposed in function of the target gas to detect. In particular, this work deals with the possibility to modulate the sensitivity and the selectivity of the sensors by enriching the sensing film with noble particles. The first proposed layer is formed by Nb_2O_5, obtained by reactive sputtering plasma deposition and it allows to obtain excellent results on the detection of acetone and ethanol (see below). Enriching such layer with Pt surface agglomerates the selectivity turns toward hydrogen detection. Such nanoparticles are obtained by a second plasma deposition on the first Nb_2O_5 layer, covering a smaller area (about 9.5 mm^2) in order to avoid a conductive bridge between the electrodes causing a short-circuit.

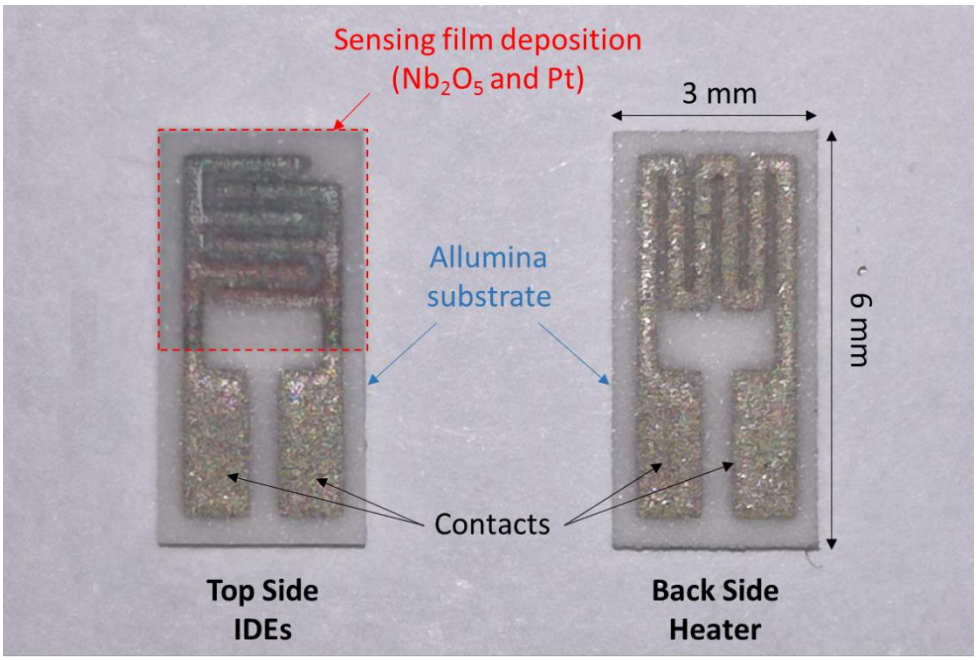

Figure 10: Illustration of the proposed gas sensor: on the left, the IDEs are exposed, highlighting the sensing Nb_2O_5 film within the red dash line. On the right, it is possible to observe the Pt heater.

In order to guarantee a suitable design for its implementation in gas detecting, the interdigitate electrodes were designed with a specific geometry as showed in Figure 11. Generally, such sensors are commercially available at low-cost and are characterized by small dimension, about 6 mm x 3 mm. The characteristic sensor dimensions are highlighted in Table 3.

Nonetheless, the effective response area is confined between the two inter-digitate electrodes since such small portion creates the effective link between them (the yellow paths in Figure 11-C and D) with a final dimension of about 2.06 mm^2. Such area can be described as a single path having a total resistance R_p that, neglecting border and corner effects, is formed by two basic contributes connected in parallel 5 times: R_a and R_b.

By such approach, it is possible to consider the interdigitated path into a linear one, as illustrated in Figure 11-D. To simplify, the sensor is analysed in a single

passage since their effective R_s can be determinate by using ρ. In this way, the equivalent active areas are formed by a length L_{eq} and a width W_{eq}, which can be extrapolated by the interdigitated dimensions:

$$W = \mathrm{j} \qquad \text{eq. 7}$$

$$L = 5\,(\mathrm{o} + \mathrm{k}) + 9\,\mathrm{j} \qquad \text{eq. 8}$$

$$S = L \cdot \mathrm{w_f} \qquad \text{eq. 9}$$

$$A = L \cdot W \qquad \text{eq. 10}$$

Where w_f S and A are the film thickness, the equivalent section and the effective area of the sensing film respectively. At this point, the equivalent total sensor resistance can be calculated as:

$$R_S = \rho \frac{\mathrm{W}}{\mathrm{S}} = \frac{\rho}{w_p} \cdot \frac{\mathrm{W}}{\mathrm{L}} = \frac{\rho}{w_p} \cdot \frac{\mathrm{e}}{5\,(\mathrm{o} + \mathrm{k}) + 9\,\mathrm{j}} \qquad \text{eq. 11}$$

Thus, it is possible to replace the interdigitated dimensions obtaining:

$$R_S = \frac{\rho}{51.5 \cdot w_p} \qquad \text{eq. 12}$$

A different result is obtained working with equivalent active area and equivalent substrate dimension (L and H), even if the linear structure in Figure **11**-D is being keep in consideration, as follow:

$$A_{ef} = L_{eq} \cdot W_{eq} = 2.06\ \mathrm{mm}^2 \qquad \text{eq. 13}$$

$$L^*_{eq} = HF - s = 3.0\ \mathrm{mm} \qquad \text{eq. 14}$$

$$W^*_{eq} = \frac{\mathrm{Aef}}{\mathrm{Leq}} \approx 690\ \mathrm{nm} \qquad \text{eq. 15}$$

Obtaining a total effective sensor resistance of:

$$R^*_S = \rho \frac{\mathrm{W}}{\mathrm{S}} = \rho \cdot \frac{\mathrm{W}}{w_p \cdot \mathrm{L}} = \frac{\rho}{4.35 \cdot w_p} \qquad \text{eq. 16}$$

Comparing eq. 12 and eq. 16 it is possible to observe that film resistance is clearly affected by the interdigitated structure by a factor of about 12 with respect to a linear structure. Therefore, interdigitated configuration allow gaining noteworthy benefits in terms of measurements equipment costs and noise reduction.

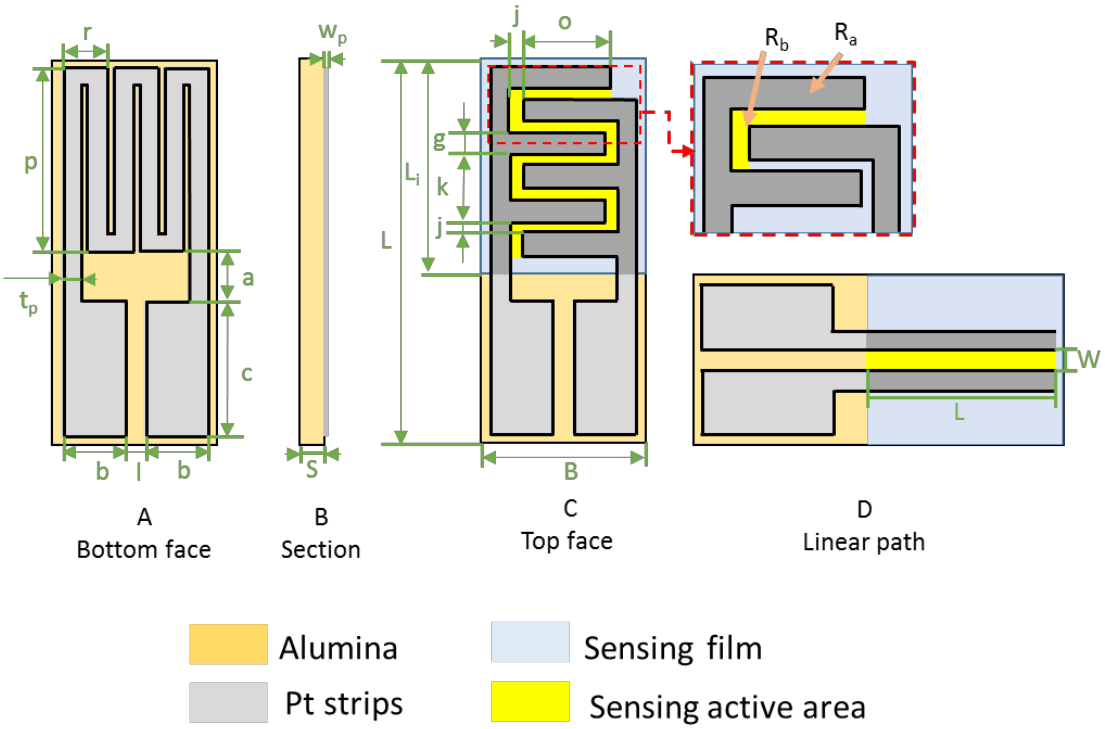

Figure 11: Sensor design details of bottom face (A), section (B), top face (C) and the linearized path (D).

Table 3: Sensor dimension details.

Label	Dimension (mm)	Label	Dimension (mm)	Label	Dimension (mm)
L	6.0	j	0.2	c	2.0
B	3.0	g	0.3	a	0.6
S	0.5	t_p	0.3	o	1.4
L_i	3.3	l	0.4	w_p	5.0×10^{-3}
k	1.0	r	0.7		
p	2.8	b	1.0		

1.5.2. Plasma deposition of the sensing layers

The sensing Nb_2O_5 and Pt films are deposited by means of two different plasma deposition systems, both employed at the Department of Applied Science and Technology, Politecnico di Torino, Turin, Italy.

First Nb_2O_5 deposition is carried out by a customized lab-scale RF-plasma system (Figure 12), characterized by a capacitively coupled parallel-plate-reactor, which involves an unbalanced magnetron configuration. As it is possible to see in Figure 14, such plasma system involves a cylindrical-shape deposition chamber where are located, on the top, the cathode electrode and, on the bottom the anode

electrode. In particular, the cathode electrode is fixed on the top section of the deposition chamber, featured by a motion system useful to open and close easily the chamber itself. Figure 15 shows the two main cathode components:

- *First part* is the electrode body in copper (99.99% purity). On the bottom side is located the niobium target (99.99% purity) while on the top side the cooling system is present and all around are place the magnets sets (the second part).
- *Second part* is formed by the magnets sets that are disposed in type II unbalanced mode. In the outer circle, N orientation magnets are disposed while in the inner circle P orientation magnets are present. In this particular case, there is a third magnets (N-orientated) set located in the centre of the electrode in order to maximize the deposition rate in the middle of the opposite anode electrode.

On the bottom of the chamber is located the anode where the substrates are placed during the deposition process. Under the anode, there are seven heaters, which allow to control the deposition temperature, to a maximum of 600°C. The vacuum system allows to create and keep the interested pressure inside the chamber. It involves a rotary pump (PFEIFFER, model: DUO20C) and a turbo molecular pump (PFEIFFER, model: TPH261PC). The mass flow system, actually, controls the gas mixture and its flow inside the chamber in order to obtained the work atmosphere. In particular, the gases involved for such depositions are argon, the main constituent of the plasma glow discharge at a constant pressure of 50 sccm[1], and oxygen, which reacts with sputtered Nb in order to obtain the reactive deposition of Nb_2O_5, at a constant pressure of 20 sccm. Such high oxygen concentration guarantees a reactive sputtering mode of the plasma deposition, allowing to obtain a dense film with the stoichiometry Nb_2O_5 [46]. A RF power supply (TRUMPF, model: PFG1000RF) with a frequency of 13.56 MHz is employed to bias the electrodes, which are connected by a RF matching system (TRUMPF, model: PFM1550A). The whole apparatus is controlled by a dedicated software. Regarding the mass flow meter system and the resistive heaters exposed in Figure 12, they are required for the realization of thin films by Plasma Enhanced Chemical Vapour Deposition, thus they will be better introduced in chapter 3.

Before the deposition, the substrates are heat treated in oven at 400 °C for 4 h in order to release every stress residue caused by the Pt screen-printing. After that, the substrate are sonicated in ethanol for 15 min and dried by pressure air.

1 sccm: “standard cubic centimetre per minute”. 1 sccm = 1690 cm^3/s

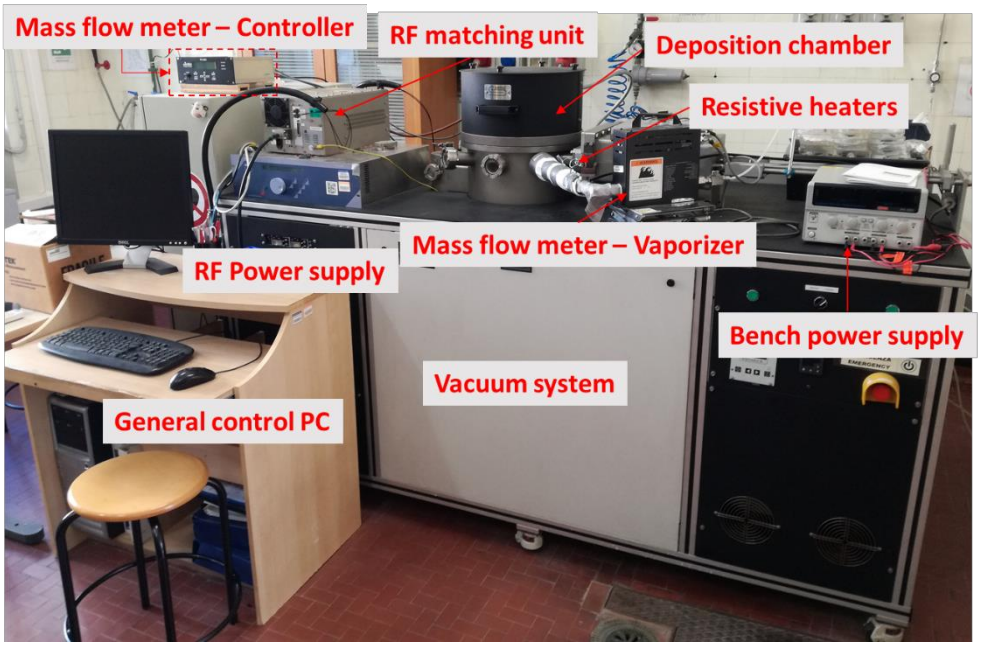

Figure 12: Employed plasma reactor system.

At this point, the substrate is arranged in the centre of the anode with the interdigitated electrode side towards the Nb target, as showed in Figure 13. A small alumina slice is used as cover to protect the contacts from the deposition, and then it is manually located onto the substrate. Beside the substrate is even placed a small N-doped Silicon rectangle in order to characterized the obtained film, since the alumina substrate surface is not smooth enough to make possible a FESEM observation (see 1.6.2.). On the contrary, silicon wafer is characterized by a very smooth surface making it suitable for further film analysis. As for the alumina substrate, even Si slice is cleaned by ultrasound in ethanol and airy dried before the deposition.

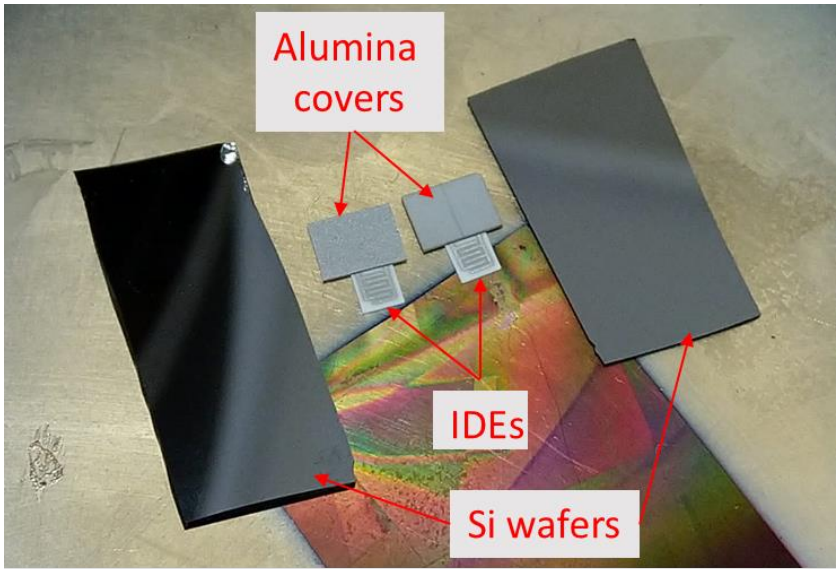

Figure 13: Substrates and Si wafer arranged inside the deposition chamber.

Reached a suitable vacuum level (in the range of $5x10^{-6}$ mbar), the chamber undergoes a pre-conditioning treatment, which involve an Ar flow for 10 minutes. Such process allows to clean the chamber and adjust the atmosphere. Thus, the O_2 flux is flown inside the chamber and the plasma glow discharge starts. The parameters involved for Nb_2O_5 films deposition are listed in Table **4**.

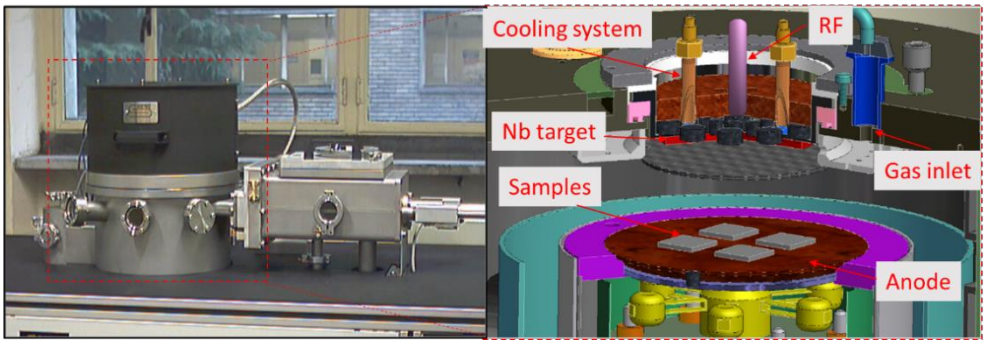

Figure 14: Deposition chamber details.

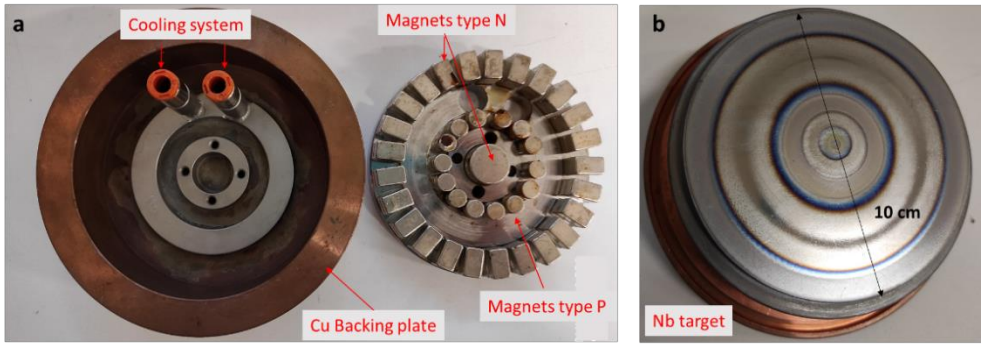

Figure 15: Electrode body, cooling system and magnets details (a) and niobium target (b).

Table 4: Plasma deposition parameters employed for the Nb_2O_5 depositions.

Sample	Ar/O_2 (sccm)	Power (W)	Deposition Time (min)
1	50/20	250	30
2	50/20	500	60
3	50/20	150	60
4	50/20	500	60
5	50/20	500	60

The second Pt deposition is carried out by means of a commercial plasma system (QUORUM; model: Q150T S). Such deposition are carried out onto samples labelled 4 and 5, as reported in Table 5, by using the same parameters. Both samples and the relative Si wafers are arranged, with the interdigitate electrodes side toward the target, onto a stub where a thin carbon tape strip is used for fixing them and avoid their eventually movements during the deposition. In fact, such

apparatus is characterized by a rotating anodic base plate in order to obtain a more homogenous deposition. The alumina covers are placed to protect the contacts in order to avoid the formation of a conductive link between them. The deposition process is completely automatized and lasts only 5 minutes to finish since it needs a lower vacuum level than the first plasma deposition system, at the range of $5x10^{-4}$ mbar. Only Ar is fluxed in such deposition processes since, in this case, a reactive sputtering is not required.

Table 5: Plasma deposition parameters employed for the Pt depositions.

Sample	Power (W)	Deposition Time (s)
4	30	10
5	30	10

Only sample 5 underwent to a second Nb_2O_5 and Pt deposition respectively, in order to obtain a sandwich structure. These depositions are obtained employing the same parameters already used for the first layers.

1.5.3. Heat treatments

After Pt depositions, samples 4 and 5 achieved a resistance, measured between the interdigitates electrodes, in the range of few Ω. In fact, the Pt deposition process leads to the formation of a thin and compact film onto the Nb_2O_5 one. In order to guarantee an effective response by a conductometric sensor, the baseline resistance should be high enough to appreciate the modulation of the depletion zone by the target gas. For this reason, a heat treatment is carried out in order to increase these resistance values. In fact, a thermal driving force can reorganize the surface Pt film in nanometric agglomerates, which are no longer in connection causing an increase of the sensor resistance.

The heat treatment is performed by means of a tubular furnace (THERMO SCIENTIFIC; Model: Lindberg/blue M), in inert Ar atmosphere (pure at 99.99%) at 600 °C for 30 minutes. Both the samples and the relative Si wafers are placed in the middle of the alumina tube in order to guarantee the effective working temperature.

1.6. Films characterization

The different deposited films are characterized in term of microstructure, morphology and chemistry by several techniques.

First step is the thickness and the superficial morphology investigation by means of a Field Emission Scanning Electron Microscopy (FESEM) model Supra 40 Zeiss. Regarding the thickness, the Pt deposition film is negligible for the final thickness results since after 10 seconds only few nm are deposited (less than 2 nm) and such layer cannot be observed by FESEM.

The chemical composition of the films is evaluated by X-ray Photo-electron Spectroscopy (XPS), by means of a PHI model 5000 electron spectrometer combined with a monochromatic aluminium source (1486 eV). All the measurements are carried out employing 25W as power, in an operating pressure lower than $5x10^{-6}$ Pa. In addition, a high-resolution analysis was performed on C 1s, O 1s and Nb 3d peaks employing 11.75 eV as pass-energy.

1.6.1. Chemical characterization

In order to confirm the deposition of niobium penta-oxide layer, the chemical composition analysis of the films by means of XPS analysis was carried out. The analyses were only performed on niobium oxide layers of each samples and no important differences were observed among them. For this reason, only the spectra related to sample 1 are exposed in Figure 16. The spectra is correct with respect to the C 1s peak as energy reference. Therefore, all the binding energy peaks are shifted from the centre of the C peak, having an energy of 284.6 eV. As a matter of fact, such carbon peak is caused by environmental contamination and it is characterized by this binding energy.

Besides C line, in Figure 16 on the right are showed the typical binding energy peaks of Nd and O. In particular is worthy to be highlighted the presence of peak of Nb 3d3/2 and Nb 3d5/2, at 209.8 eV and 207.1 eV respectively, that are characteristic of Niobium with oxidation state equal to 5, confirming that the film is mainly formed by Niobium (V) pentoxide, Nb_2O_5

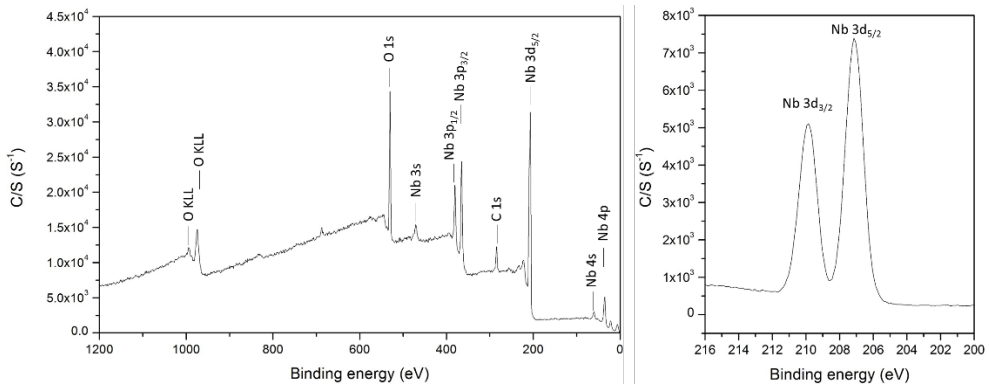

Figure 16: XPS spectra of the Nb_2O_5 sensing film obtained at 250 W for 30 minutes (sensor 1).

1.6.2. Morphology and thickness characterization

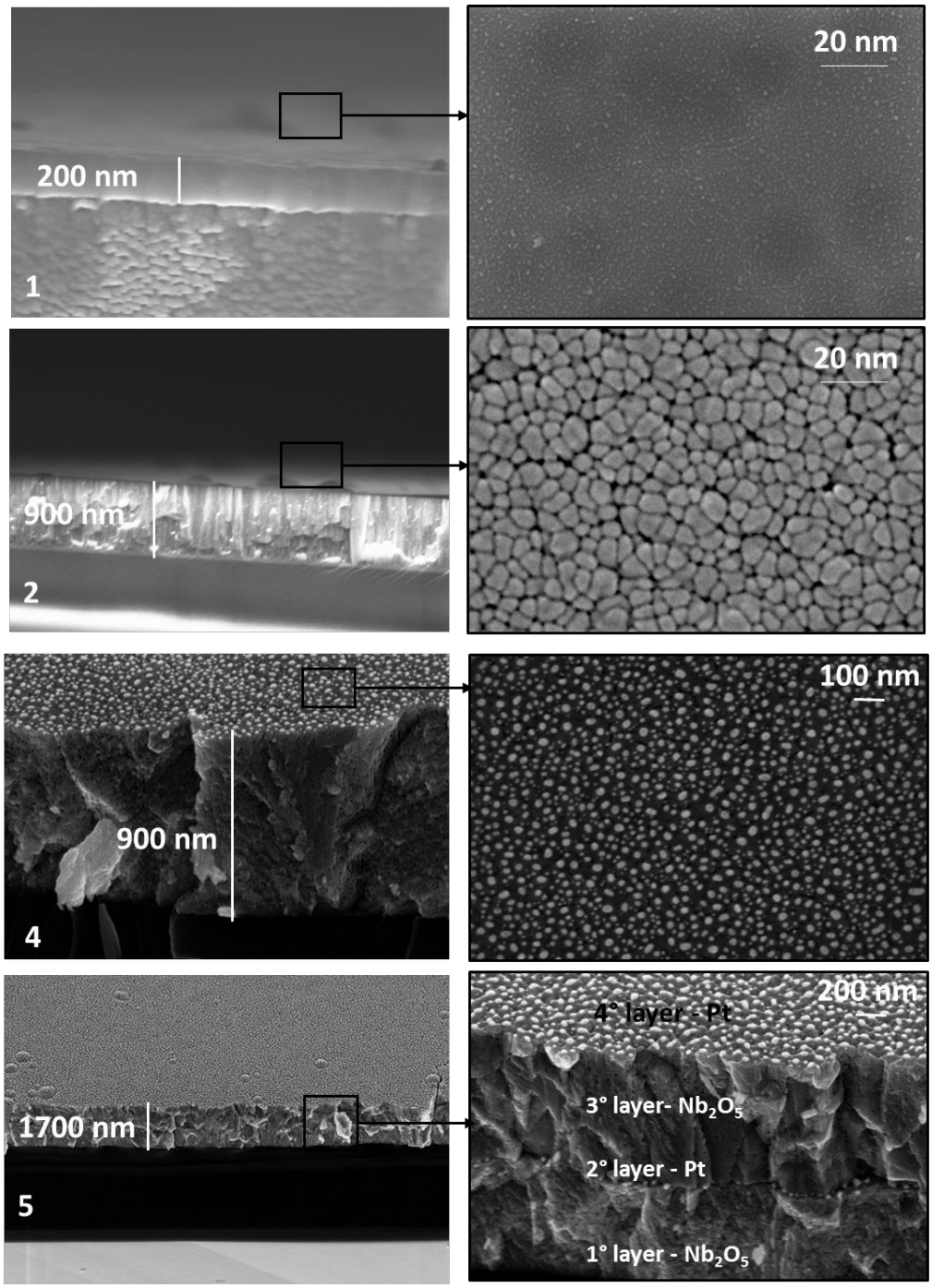

Figure 17: Cross section and morphology details acquired by FESEM analysis.

An important contribution to the effective sensors response is to attribute to the film morphologies and thickness. Such aspects are strongly affected by the parameters involved during the first Nb_2O_5 deposition process as well as the by the heat treatment carried out after the Pt deposition. From the collected images was clear that RF-power, employed during the first deposition, is the main important parameter that affect the film microstructure. Actually, as exposed in Figure 17, samples 1 and 3 obtained at 250 W and 150 W respectively show a thin and compact

layer while sample 2 realized at 500 W reveals a thick columnar microstructure characterized by vertical rods having a diameter of about 15 nm. It is an example of such behaviour the comparison of sample 1 and 2 exhibited in Figure 17. After Pt deposition and heat treatment, the morphology undergoes a drastic change whit respect to the previous situation. By an observation of sample 2 and 4 it is possible to observe that the achieved thickness still the same (about 900 nm) but the morphology is completely different. First, the Pt thin film is rearranged in nanoparticles (white islands), with diameters of few, nanometers homogeneously distributed onto the Nb_2O_5 layer surface. Moreover, also the Nb_2O_5 underwent to a morphological modification. In fact, after the heat treatment the surface is no longer characterized by vertical rod but by a more uniform surface. Nevertheless, by cross section observation, it is possible to observe the presence of high presence of porosity. Details about the achieved thickness are listed in Table 6.

Concerning sample 5, the microstructure is identical to sample 4 but the double deposition processes lead to a sandwich structure. In particular, it is possible to observe that both the Pt layers are rearranged to Pt islands. Therefore the two niobium oxide layers are separated by a non-continuous Pt layer.

Table 6: Measured thicknesses by FESEM cross section analysis.

Sample	RF-Power (W)	Dep. Time (min)	Thickness (nm)
1	250	30	200
2	150	60	160
3	500	60	900
4	500	60	900
5	500	60	1700

Chapter 2

Sensing characterization of MOX sensors for biomedical applications

This chapter partially contains materials from previously published work of the author [1][2][3][47]

2.1. Introduction

In this chapter, a detailed description of the proposed sensors sensing toward acetone, ethanol and hydrogen is provided. All the measurements have been carried out at Università di Messina at the laboratories of prof. Giovanni Neri and Nicola Donato.

2.2. Instrumentation set up

The electrical and sensing characterization of the prototypes were obtained by means of a customized measurement bench, realized with the specific scope to evaluate conductometric gas sensors. The details about the employed bench test are exposed in Figure 18. It involves a small test chamber of about 5 cm^3, suitable to obtain fast response by few concentrations of the target gas. The sensor is placed inside the chamber with the interdigitate electrode toward the inlet on the top of the chamber. Such inlet allows to flow inside the chamber the proper gas flow while the outlet, located at the bottom of the chamber, to flow out the gas. The interested gas mixture is obtained in function of the target gas sensing by means of five mass flow meters (BRONKHORST, model: F-201C-FAC-22), which control the gas flows, from certified gas bottles, in order to obtain the suitable gas ratio. Such mass flow meters are controlled by a dedicated computer and are characterized by an uncertainty of 2%. Nonetheless, the implement of only the mass flow meters does not guarantee a fast control of the gas flow inside the test chamber since a stabilization delay time is not present. Therefore, each mass flow meter is coupled with a valve that allows to open and close immediately the gas flow. In this way, it is possible to measure the sensors response time with higher accuracy. Another important point is the relative humidity inside the chamber, which is possible to modulate by a humidity probe that controls the gas bubbler connected to the gas inlet. The platinum heater is connected by a bench power supply (AGILENT, model: E3632A), in order to control the working temperature by a close-loop. In

this way, the heater can act as actuator as well as temperature probe. In fact, the power supply controls in parallel the output voltage and the read out output current of the Pt heater. Such information are read and stored by the computer, connected to the power supply by a GPIB interface and a dedicated software computes the instant heater resistance as:

$$R_h = V_0/I_0 \qquad \text{eq. 17}$$

Thus, it extrapolates the effective heater temperature from the resistance vs temperature curve of the heater. Finally, the working temperature is stabilized by means of a closed-loop proportional integral derivative control (PID), which controls the output voltage.

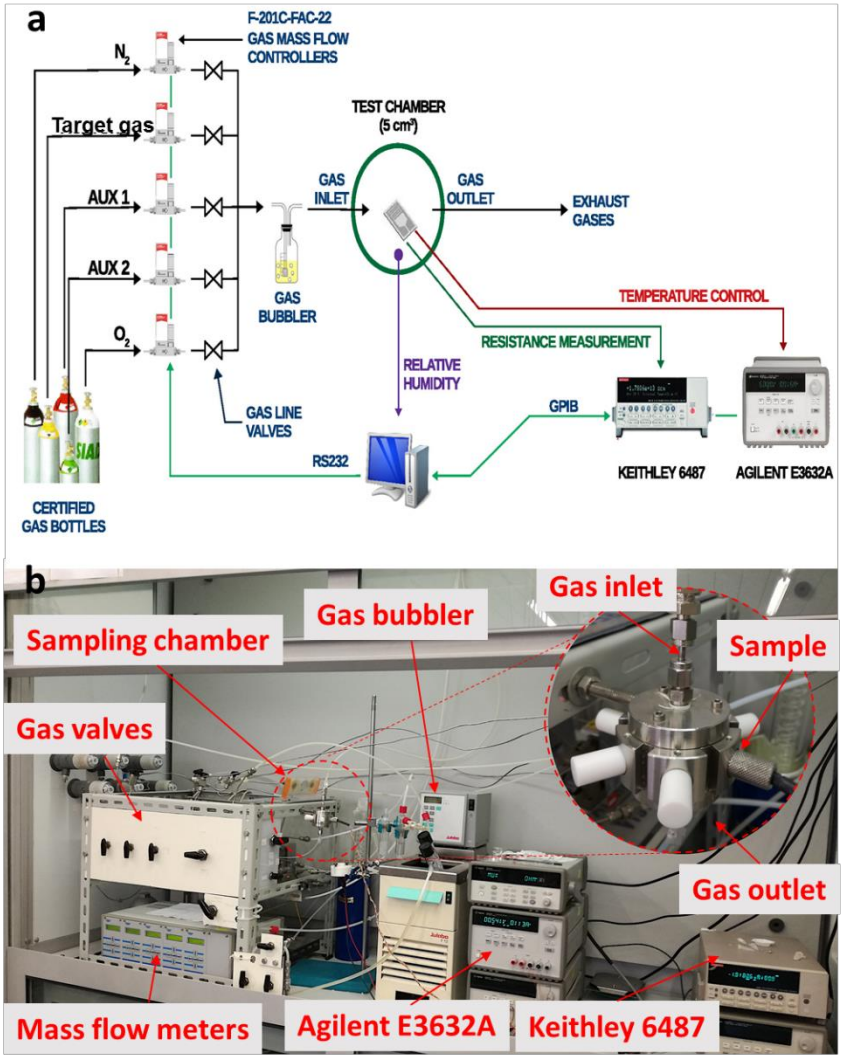

Figure 18: Schematic block of the employed measuring system (a) and details of the effective measurement bench (b).

The sensing film resistance is monitored by a picometer (KEITHLEY, model: 6487) connected to the computer via GPIB Interface and allows to obtain resistance

measurements with an uncertainty of about 0.2%, negligible with respect to the uncertainty related to the mass flow controllers.

All the measurements, carried out for the sensors characterization, involve dry synthetic air, obtained by a mixture of oxygen and nitrogen at 20% and 80% respectively, as carrier. The target gas flow is controlled by a dedicated mass flow meter, which guarantees the proper concentration during the test.

2.3. Heater calibration

Before starting the sensing characterization of the sensors, it is extremelly important to estimate the uncertanty of the set temperature obtained by the Pt heater, since it can affect the accuracy of the working temperature. For this reason, a calibration campaign has been carried out in order to minimize such uncertainty, collecting the heaters resistance at difference temperatures up to 400 °C. Each sensor was connected to the already mentioned power supply (AGILENT, model: E3632A) by the heater contacts. The temperature was monitored by means of a thermocouple fixed to the substrate by a thermal paste and the typical resistance vs temperature curves were achieved for each substrate. From these curves, the linear fitting was extrapolated, obtaining the characteristic values related to the resistance at room temperature (R_r) and the temperature coefficient (α) of the heaters. Such values were stored in the PID control software, which controls the working temperature using eq. 19, obtained by inverting eq. 18 to measure the sensor resistance.

$$R = R_r + \alpha\,(T - T_r) \qquad \text{eq. 18}$$

$$T = T_r + \frac{1}{\alpha}(R - R_r) \qquad \text{eq. 19}$$

The stored values allow a better control of the temperature of the sensor, minimizing the uncertainty, which is estimated of about 10 °C. Regarding the power supply, it can guarantee a temperature control with an uncertainty less than 2 %. An example of the collected calibration curves for three samples are showed in Figure 19 and the relative values in Table 7.

From the extrapolated values, it was observed a large dispersion of the R_r and α values among the different substrates of about 0.5 Ω and 10^{-4} K^{-1} respectively. It follows that without an accurate calibration the large dispersion leads to an unacceptable uncertainty of the set temperature.

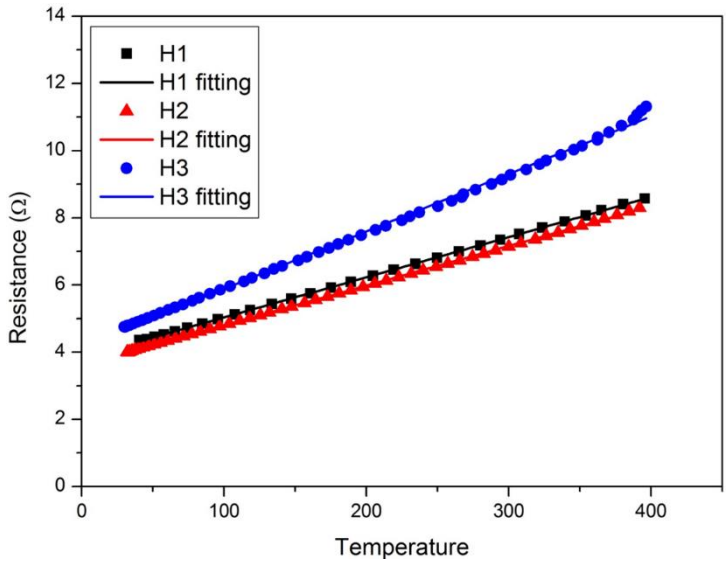

Figure 19: Calibration curves of three different heaters and related fitting.

Table 7: Resistance at room temperature and temperature coefficient extrapolated for the three heaters calibrated in figure 19.

Substrate	R_r (Ω)	α (K^{-1})
H1	4.23	17.36×10^{-3}
H2	3.92	12.03×10^{-3}
H3	4.61	11.70×10^{-3}

2.4. Acetone sensing

Acetone is a molecule regularly produced by the human metabolism. It is mainly produced by the liver under the Krebs cycle and by lipid peroxidation and it can be detected in the exhaled human breath in the range from 300 ppb to 900 ppb [48]. The arising of diabetes conditions can increase this concentration up to 2 ppm. For this reason, a sensitive and selective acetone sensor is required in order to detect such low concertation from the exhaled breath. The following characterizations are focused on the evaluation of the proposed prototypes performances. The employed prototypes are exposed in Table 8

Table 8: Details of the samples employed for acetone sensing.

Sample	RF-Power (W)	Dep. Time (min)	Thickness (nm)
1	250	30	200
2	150	60	160
3	500	60	900

2.4.1. Temperature dependence of the sensor response toward acetone

First step for a complete sensing characterization of the proposed sensors concerns the detection of the optimal working temperature. In fact, as explained in section 1.3, the working temperature changes in function of the target gas as well as the used sensing material. At this scope, each prototype was located inside the test chamber with the presence of a constant flow of synthetic air (see 2.2) and tested from 400 °C to 200 °C in five steps of 50 °C each. Starting from 400 °C, after the temperature is stabilized, a pulse of 5 ppm of acetone is flown inside the chamber and the response (resistance variation) is recorded. The same process was repeated for the others temperature steps. The curves related to the temperature dependence are exposed in Figure 20 and the results show a drastic decrease of the baseline resistance increasing the temperature, which is a typical metal-oxide behaviour. Moreover, at 200 °C it is clear that the temperature is too low for an appropriate acetone detection measurement. Actually the baseline resistance is extremely high (10 GΩ) and it is characterized by high background noise. As expected the response increases increasing the substrate temperature, obtaining results more clear for each sensor as well as lower baseline resistance, in the range between 100 MΩ for temperature higher than 300 °C.

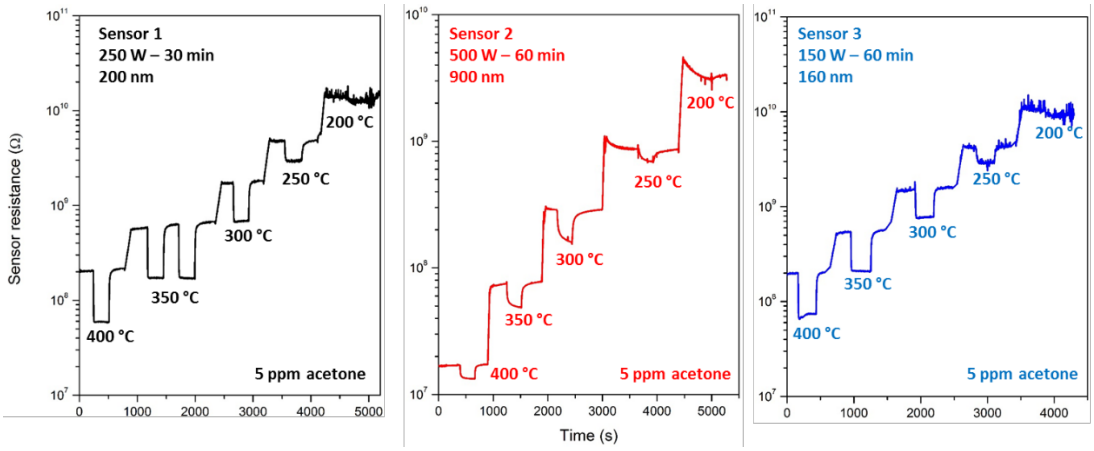

Figure 20: Sensors responses toward 5 ppm of acetone at different temperatures.

As last consideration, it is possible to observe how sensor 1 and 3, having lower thickness, reach better results than sensor 2 characterized by a thickness of about 900 nm. It can be better observed in Figure 21, where the calculated responses for each sensor are plotted against the set temperature, in order to obtain a direct comparison among the sensor responses. First of all, the curves exhibit the typical bell shape temperature dependence of the sensors (see 2.2) and it highlights the effect of the thickness on the optimal working temperature as well as the effective sensors response. Actually, sensors 1 and 3 reach the working temperature at about 350 °C and are characterized by higher response (especially sensor 1) while sensor 2 shows the best response at 300 °C but it is drastically lower than the others.

Such behaviour can be justified focusing on the sensing mechanisms that occurs during the target gas adsorption in this kind of sensors. The resistance variation is function of the modulation of the depletion zone by the target gas, which removes the adsorbed oxygen species (O_2^-, O^- and O^{2-}) from the film surface, releasing electrons into the conductive band as described in eq. 20 [49] [50]:

$$CH_3COCH_3 + 8O^- \leftrightarrow 3CO_2 + 3H_2O + 8e^- \qquad \text{eq. 20}$$

The effect of such mechanism is strictly related to the thickness of the sensing film since it involves only the bonds created at the surface and not at the bulk. Sensors 1 and 3 present a thin layer and the ratio between the depletion zone and the thickness can reach the unity, making the film most depleted (as described in section 1.3). On the contrary, Higher thickness leads to a predominate effect of the bulk conduction and subsequent smaller relative response with compare to thin films one. However, it is clear that the sensor response is affected from different factors and not only by the film thickness. In fact, sensor 1, characterized by a film thickness of about 200 nm, achieves the best response toward acetone detection with respect to sensor 3, characterized by a thinner film of about 160 nm. It is worthy to be note that, even if their thickness is quite similar, the deposition parameters, employed for the realization of sensor 1 and 3, were different, which can lead to a different morphology of the deposited Nb_2O_5 grains. It turns out that there is an optimal combination between the sensing film thickness and the related deposition parameters employed to obtain it, which leads to best sensing response.

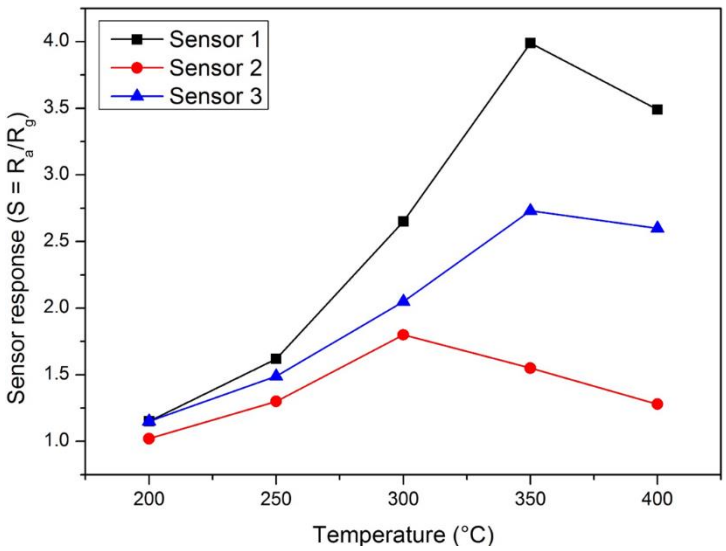

Figure 21: Temperature dependence of the three proposed sensor at 5 ppm of acetone in the range between 200 °C and 400 °C.

The film thickness as well as the deposition parameters do not affect only the sensor response but also the base line resistance in pure air atmosphere. Figure 22 shows the baseline resistance R_a, evaluated for each sensors, in function of the working temperature involved for the temperature depending characterization. How

it was expected, the R_a values decrease, decreasing the working temperature according to a quasi-exponential trend. The thickness also plays an important role according to eq. 21:

$$R_a = \rho \frac{j}{A} \qquad \text{eq. 21}$$

Where ρ is the Nb_2O_5 resistivity, j is the distance between the two IDEs, covered by the Nb_2O_5 film (see section 1.5.1.); A is the film area confined between the two IDEs (yellow area in Figure 11-C). As a matter of fact, sample 2 achieves the lower R_a values at each working temperature since it has the thicker sensing film (about 900 nm). Regarding sensor 1 and 3, they have almost the same trend but sample 1 achieves the higher R_a along all the test temperatures. This is an interesting result since it is characterized by a thicker sensing film with respect sensor 1. Even this case can be explained by taking in account the different deposition parameters employed during the deposition processes. Actually, sensor 3 was obtained at lower RF-Power for a longer time (150 W, 60 min.) meaning that the deposition rate was extremely lower than the one achieved for sensor 1 (250 W, 30 min.). The effect of this lower deposition rate reflects to a more compact thin film avoiding the rise of residual stress, which can modify the Nb_2O_5 resistivity. It turns out to a higher conductivity of sensor 3, even if it characterized by a lower thickness.

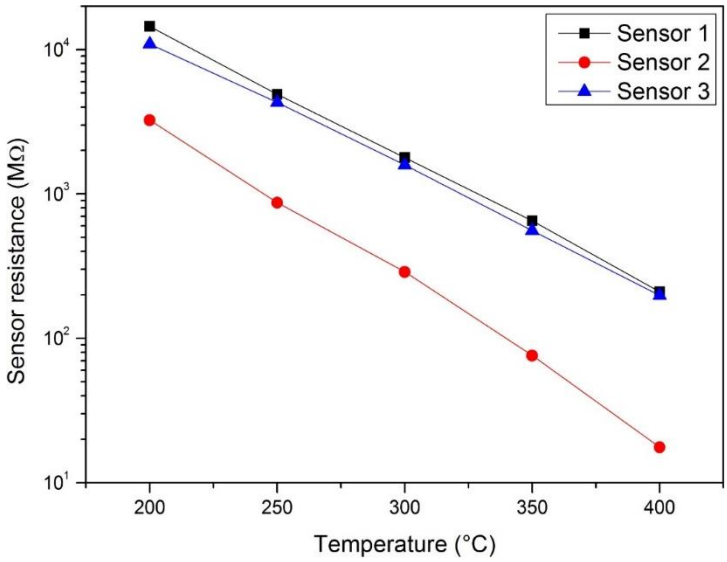

Figure 22: Baseline resistance of each sensor as function of the temperature, from 200 °C to 400 °C.

2.4.2. Response and recovery times

An important feature, for a suitable breath analyser, is to achieve good response and recovery times during the measurement, in order to obtain fast results. In this way, it is possible to improve the accuracy of the measurement by reducing the

variability that can arise during the breath test. They are defined as the time the sensor requires to reach steady resistance values in presence of the target gas (response time) and to return to the initial baseline resistance when the target gas flux is stopped (recovery time). Since the exactly time, required to reach both the steady states, is not easy to estimate, response and recovery time were obtained by calculating the elapsed time in the range between 10 % and 90 % of the transient.

For this characterization, only the responses obtained at the optimal working temperature were taken in account (350 °C for samples 1 and 3 and 300 °C for sample 2). In order to appreciate the differences among the different sensors, all the responses were normalized between 0 and 1 and shifted in time. In this way, it was possible to overlap the curves, as showed in Figure 23. The results, listed in Table 9, show a drastic difference in terms of sensor response achieved by sensor 2 with respect to sensor 1 and 3. In fact, the latter exhibit quite high sensor responses of about 3.6 s and 5 s for sensor 1 and 3 respectively while sensor 2 lasts 46.1 s; about 12 times the time required by sensor 1. The same behaviour can be observed for the recovery time. Actually, sensor 2 takes about 116.8 s to reach the 90% of the initial baseline resistance values. This means that at least 2 minutes of recovery are required among the measurements, increasing the total measurement time. Such recovery time is almost the double with respect to the ones achieved by sensor 1 and 3, since they reach the 90 % of the recovery after 48.8 s and 52.5 s respectively. Such different behaviour can be attributed to the different morphology of the samples. As described in section 1.6.2., sensor 2 is characterized by a thick and porous sensing film. This means that the acetone molecules need time to diffuse inside the microstructure and reacting with the sensing surface. Regarding sensor 1 and 3, they are characterized by compact and thin films, therefore the target gas is immediately in contact with the sensing surface e no further diffusion processes are required. This turn out in a fast response of the sensors toward the target gas.

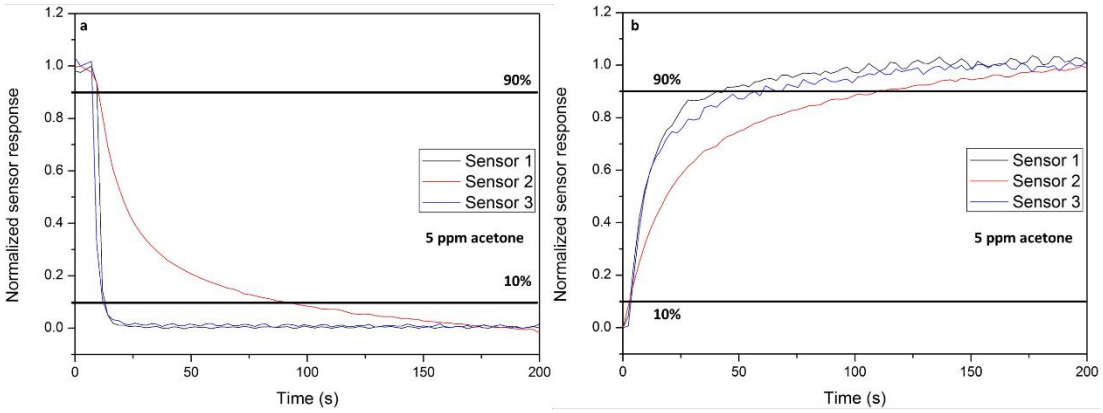

Figure 23: Response time (a) and recovery time (b) for the three sensors obtained at their optimal working temperature.

Table 9: Extrapolated response times and recovery for the three sensors.

Sensor	Response time (s)	Recovery time (s)
1	3.6	48.8
2	46.1	116.8
3	5	52.5

In conclusion, sensor 1 and 3 achieved the best results in terms of response and recovery time being able to provide measurements in quite low time, making them suitable as breath analyser. In fact, they guarantee fast measurement increasing the measurements accuracy.

2.4.3. Sensitivity toward acetone

The previous sections deal with the influence of temperature toward the sensing response in order to detect the optimal working temperature. This allows to characterize the effective sensor 1 and 2 sensitivity versus acetone at their optimal working temperatures that are 350 °C and 300 °C respectively. Such sensitivity response consists to pulse inside the test chamber acetone by adding its specific concentration to the carrier gas. The results curves are collected and exposed in Figure 24. First, it is clear that both the sensors responses increase increasing the acetone concentration and sensor 1 achieved the best sensing results with respect sensor 2, as expected.

Moreover, a linear response can be observed for both the sensors at low acetone concentrations, thus they reach a saturation level that lead to a visible bending of the response, as exposed in Figure 24. In particular, sensor 1 starts to be saturated for acetone concentrations higher than 3 ppm, then the response starts to be out from the linearity up to a complete saturation at 12 ppm. Sensor 2 shows a similar trend but a linear response is visible up to 10 ppm, more than 3 times with respect sensor 1, and the saturation starts to be noteworthy for concentration higher than 20 ppm.

Saturation is a drawback of this kind of sensor since the sensing area is quite small and the response is related to the chemisorption sites available onto film surface. It is obvious that such sites number decreases increasing the target gas concentration. Sensor 1 is characterized by a thin and compact film and the active sites are confined in a small surface area. On the contrary, sensor 2 exhibits a columnar and porous morphology, which leads to a higher surface area. Thus, the morphology of sensor 2 guarantees a high number of chemisorption sites, increasing its capability to adsorb high concentration of acetone.

An empirical fitting of the experimental data is also extrapolated in order to approximate the relationship between the sensors responses in function of the acetone concentrations involved during the characterization. Low acetone concentrations can be described, for both sensors, with a first order fitting:

$$S = bX + a \qquad \text{eq. 22}$$

Where S is the sensor response, X the acetone concentration in ppm. Actually, such linear approximation is suitable for modelling the sensors response for concentration lower to the maximum allowed, X_{max}. Such maximum value turns out being 3 ppm a 10 ppm for sensor 1 and 2 respectively. For higher concentration, a second order fitting is required in order to describe in the best way the sensors response:

$$S = cX^2 + bX + a \qquad \text{eq. 23}$$

The response modelling of both sensors can be extrapolated by inverting such relations and replacing the coefficients obtained by the empirical fitting, exposed in Table 10. The obtained relations are:

$$X = 1.5\ (S-1) \qquad \text{for } X \leq 3 \text{ ppm} \qquad \text{eq. 24}$$

$$X = 13.1 - \sqrt{20.6 - 35.1\ S} \qquad \text{for } X \leq 12 \text{ ppm} \qquad \text{eq. 25}$$

For sensor 1, and:

$$X = 4.2\ (S-1) \qquad \text{for } X \leq 10 \text{ ppm} \qquad \text{eq. 26}$$

$$X = 13.1 - \sqrt{209.2 - 35.6\ S} \qquad \text{for } X \leq 50 \text{ ppm} \qquad \text{eq. 27}$$

For sensor 2.

To conclude, both sensors achieved excellent sensing toward acetone detection, and their saturation limit cannot affect a correct diabetes diagnosis, since it causes an increment of the acetone inside the human breath that none exceed 2 ppm.

Table 10: 1° order and 2° order fitting coefficients extrapolated by the calibration curves in figure 24.

	Sensor 1		**Sensor 2**	
Coefficient	**1° order**	**2° order**	**1° order**	**2° order**
a	1.0014	0.9851	1.010145	1.0156
b (ppm^{-1})	0.6664	0.7465	0.2389	0.2473
c(ppm^{-2})	-	-0.0285	-	-0.0013
X_{max}	3	12	10	50

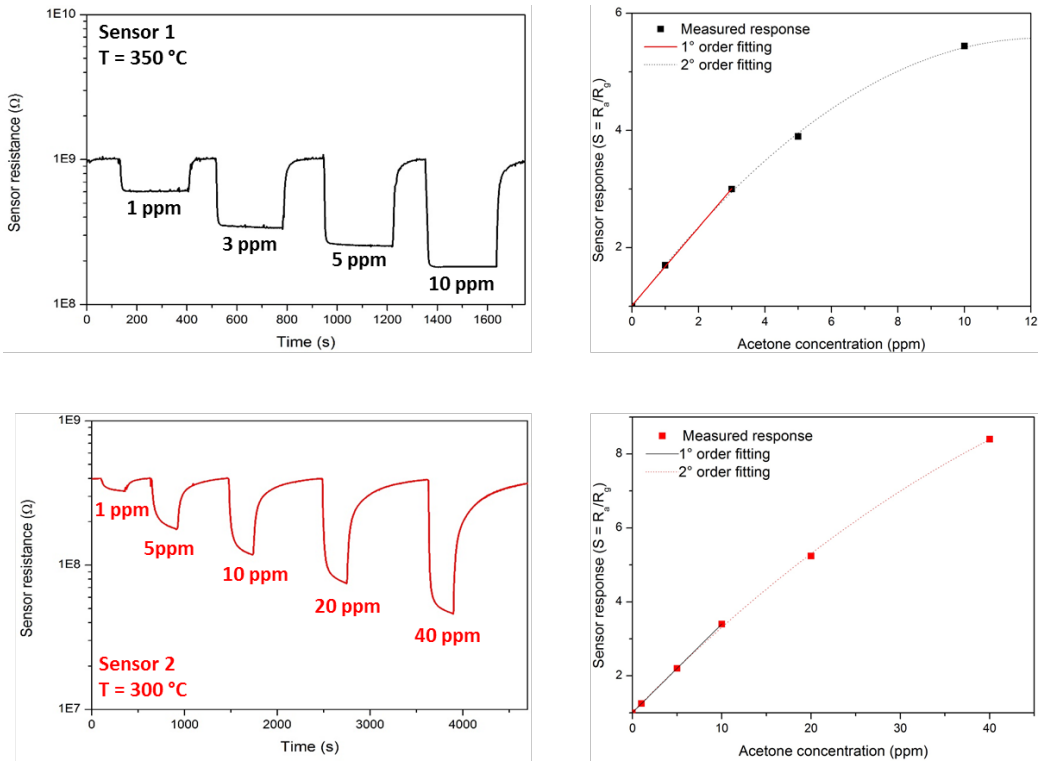

Figure 24: Responses toward different acetone concentrations of sensor 1 and 2 and relative calibration curves.

2.4.4. Sensor selectivity

High performance breath tests, such as gas chromatography and proton-transfer reaction mass spectroscopy, are able to separate and detect several different compounds from a complex gas mixture, which is the human breath, but the results are not immediate and require time to complete the analysis. On the contrary, conductometric gas sensors are characterized by an immediate response but they cannot discriminate the different compounds present inside the breath aerosol. For this reason, such sensors require high selectivity toward the designed compound and low/absent response toward the other gases. As a matter of fact, a conductometric gas sensor characterized by low selectivity would adsorb different gases onto its surface generating a high response, which could relate to a false positive diagnosis. Such problem is, also, emphasized by the really low concentrations of the target gases involved in the human aerosol that are in the range of ppb to few ppm.

At this scope, both sensor 1 and 2 are tested toward different interfering gases, which can be commonly found inside the breath aerosol and then can interfere with the response toward acetone detection. This characterization was carried out by fluxing inside the test chamber the gas carrier (20% N_2, 80% O_2) adding a pulse of the selected gas. In Figure 25, the responses of both sensors toward the interfering gas are showed, normalized with respect to the ppm employed with the pulse. It is clear that some gases such as CO_2, CH_4, O_2 and NO_2 are not detected from both sensors, while a small response can be observed toward CO_2 NH_3 and H_2; especially

for sensor 2 where a response lower than 5% (100 ppm) with respect to the acetone sensing was measured. Regarding sensor 1, even in this case good selectivity was achieved but the hydrogen response reaches the 13% (10 ppm) with respect to the acetone one. Moreover, it is important to mention the high response toward ethanol, which exceed the 27% (5 ppm) of the acetone one. Nevertheless, ethanol is an exogenous compound that cannot be generate by the human metabolism; but it can be only present inside the human breath after the assumption of alcoholic beverage. Therefore, an eventual alcohol interference can be easily prevent by avoiding to intake alcohol some hours before the test.

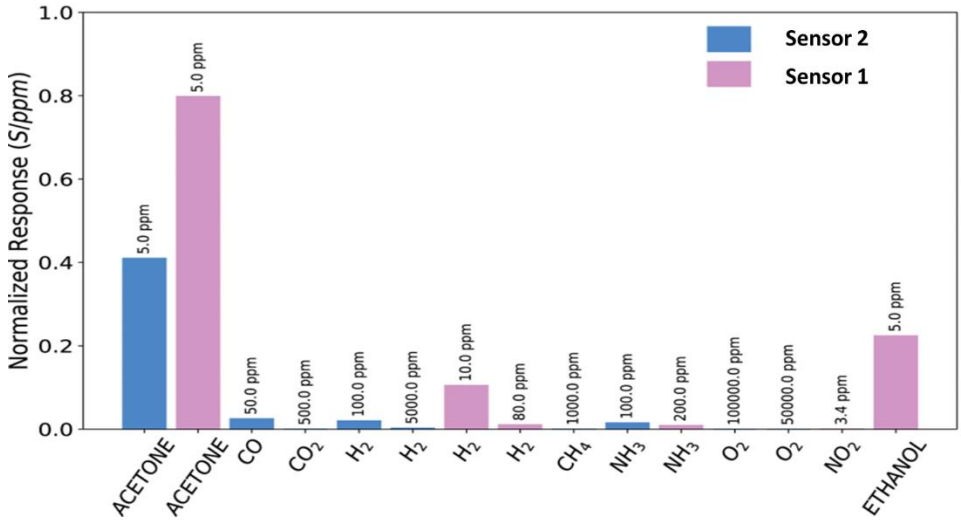

Figure 25: Normalized responses of sensor 1 and 2 towards different target gases.

2.4.5. Sensor stability

Another important feature, which is required from the obtained sensor, is a good stability that means guaranteeing repeatability among measurements over time. In fact, it is possible that the sensor responses can be affected by the modification of the surface sensing material by the exposure of aggressive environments as well as the degradation due to repeated employments over time.

For this characterization, several pulses were fluxed inside the test chamber with an acetone concentration of 5 ppm. An example with 5 pulses is showed in Figure 26 for both sensor 1 and 2 and no visible differences are present such as significant offset of the baseline resistance (R_a) as well as drifts or hysteresis. The responses and the relative error, extrapolated by the empirical data, are listed in Table 11. It is possible to observe that for both sensors the relative error among the repetitions is quite low, about 1.9% and 1.4% for sample 1 and 2 respectively. Another interesting factor is related to the response before and after the sensing measurements of the interfering gases. In fact, as showed in figure 21, for sensor 1 the response was about 3.98 while for the stability test was about 3.66 leading to a variation of about 8%. Actually, sensor 2 exhibits a response modification from

2.28 to 2.13 and a variation of 6.5%. These variations can be attributed to the high repetitions performed during the complete characterization of the sensors, especially from the tests where aggressive gases (e.g. NO_2) were employed at high concentrations. Nevertheless, the results guarantee good stability for both the sensors.

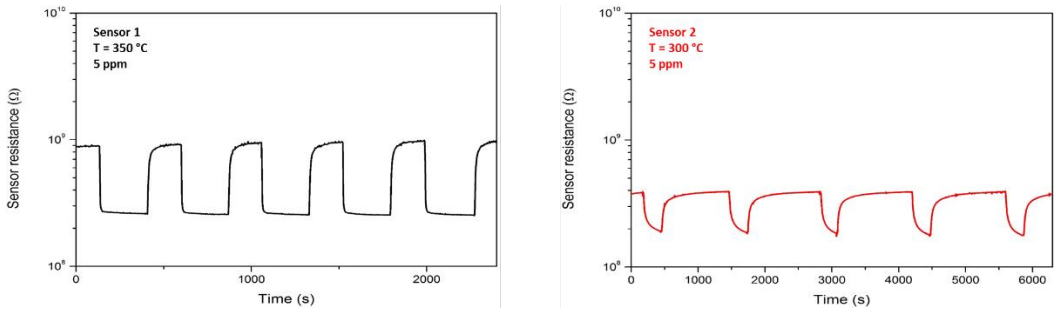

Figure 26: Responses toward repeated pulses of 5 ppm of acetone for sensor 1 and 2.

Table 11: Stability results extrapolated for sensor 1 and 2.

	Sensor 1			**Sensor 2**		
	R_a	**R_g**	**S**	**R_a**	**R_g**	**S**
μ (MΩ)	944.6	255.8	3.69	390.4	182.7	2.13
σ (MΩ)	14	1.1	0.07	1.1	2.18	0.03
ε	1.5%	0.4%	1.9%	0.3%	1.2%	1.4%

2.4.6. Sensor reproducibility

After the complete characterization of sample 1 and 2 toward acetone, it has been necessary assessing the reproducibility. With reproducibility is referred the capability to obtain performances with low variation among devices nominally obtained by using the same processes. This characterization was carried out only for sample 1 since it outperformed sensor 2, making it a suitable candidate for real biomedical applications.

For this scope, a batch of three IDEs, marked as P1, P2 and P3 was deposited by involving the same parameters employed for sensor 1 (250 W, 30 min) and characterized in term of response as function acetone concentration as described in section 2.4.3. In Figure 27, the results and the comparison with the calibrated sensor (sensor 1) are exposed. All of them exhibit the same trend. Actually, it is possible to observe the already cited linear fitting at low concentration (up to 3 ppm), followed by a gradual saturation, which leads to a second order fitting. Even the response are quite similar and the relative maximum error shows small variation among them with an intersensor difference always lower than 2%. Therefore, an individual calibration is not required if a variation of maximum 2% can be tolerated.

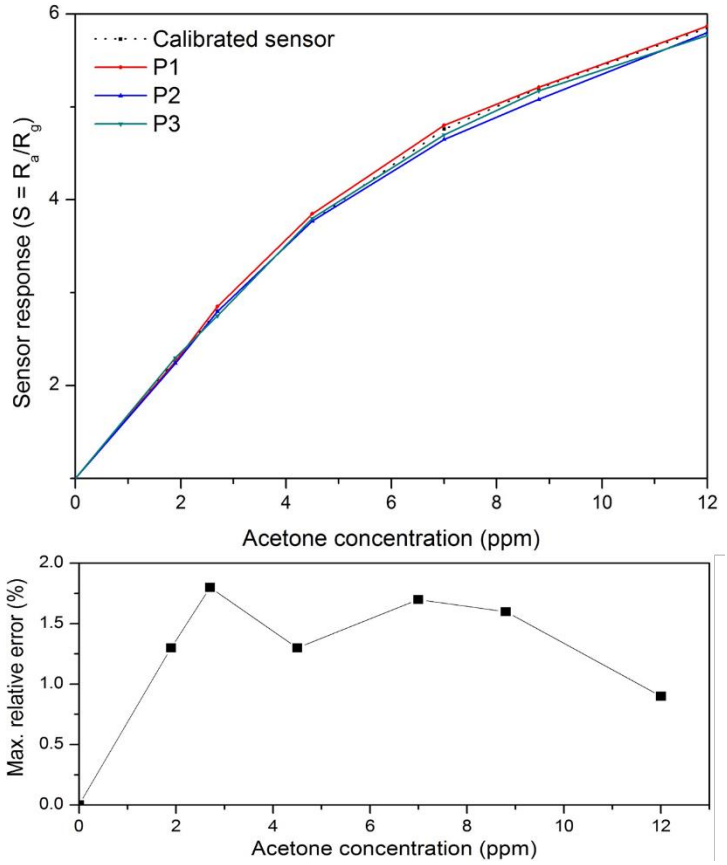

Figure 27: Comparison among responses of sensor 1 with respect to responses of three sensors obtained with the same deposition parameters and their maximum relative error.

2.5. Ethanol sensing

According to World Health Organization, alcohol abuse counts about 3 million of death per year (5.3% of all deaths) as well as it is the responsible of more than 200 different diseases and injuries. Furthermore, driving under alcohol effect is one of the main causes of drive accidents. For this reason, there are specific limits for the Blood Alcohol Content (BAC) for driving in several countries. It is generally 0.5 g/l but it reaches 0 g/l for no experienced drivers. Some examples are showed in Table 12.

Table 12: Examples of BAC limits for different countries.

Country	Experienced drivers	Not experienced drivers
USA	0.05% - 0.08%	0% - 0.02%
Canada	0.08%	0
Germany	0.05%	0
Italy	0.05%	0

The faster way to check the effective alcohol consumption is via breath test that requires being portable and guaranteeing an immediate response about the Breath

Alcohol Content (BrAC). The latter can be converted to BAC by following the conventional eq. 28:

$$BAC = \frac{BrAC}{2600} \qquad \text{eq. 28}$$

Where BrAC is expressed in ppm and BAC in percentage.

The samples employed for ethanol sensing are exposed in Table 13. However, in this dissertation only the results obtained by sample 1 are exposed, since is the prototype that exhibits noteworthy performances. Furthermore, a portable ethanol breath measuring system, based on conductometric gas sensor here exposed, is proposed.

Table 13: Details of the samples employed for ethanol sensing.

Sample	RF-Power (W)	Dep. Time (min)	Thickness (nm)
1	250	30	200
2	150	60	160
3	500	60	900

2.5.1. Temperature dependence of the sensor response toward ethanol

As for acetone, the first characterization deals with the detection of the optimal working temperature. In fact, even if sensor 1 has already undergone this characterization, the response behaviour can be modified by involving a different target gas. Therefore, a flux formed by synthetic air (80% N_2 and 20% O_2) is flown inside the test chamber. A third mass flow meter controls the ethanol concentration, which is added to the carrier mixture gas by pulse of 10 ppm as concentration. In this case, the temperature dependence characterization is performed starting from 400 °C to 250 °C in four steps, as exposed in Figure 28-a. The relative responses are extrapolated from the experimental data and plotted in Figure 28-b in order to compare directly the effective influence of the working temperature. As for the acetone case, the sensor response increases increasing the temperature, but in this case the sensor does not reach the optimal working temperature at 350 °C and the typical bell-shape is not detected. Unfortunately, the employed measurement setup cannot exceed 400 °C as working temperature, and then was not possible to investigate such characteristic. It is worthy to be mentioned that an optimal working temperature of 450 °C was detected for ethanol sensing by using a SnO thin film [51]. Nevertheless, this sensor is also employed for the realization of a customized portable breath measuring system, which requires low power consumption. Therefore, in order to guarantee an acceptable power consumption as well as good a good uncertainty of the working temperature employed by the proposed system, it was chosen as suitable temperature 350 °C.

Furthermore, there is also another important factor to note regarding the baseline resistance in absence of the target gas. In fact, resistance R_a is settled at about 700 MΩ during the entire ethanol characterization, while it was about 900 MΩ during the acetone one. An explanation of this behaviour can be correlated to the high measurement repetitions, which can lead to a microstructural modification of the thin layer due to both the aggressive gases employed and the working temperature involved during the tests. In fact, in section 1.4.4. has been explained how sensor 3 achieved lower R_a with respect to sensor 1, even if its sensing film has lower thickness. The main reason was the lower presence of residual stress due to the lower deposition rate. Therefore, the continuous characterization at high temperature may lead to a stress relaxation of the thin film, thus decrease the R_a values. It can be considered an improvement since in the range of 700 MΩ can be easily measured by low-cost equipment, gaining both in power consumption and in accuracy. In conclusion, such R_a changing is a negligible factor in term of measurement accuracy, actually the sensor response is given by the ration of R_a and R_b (see eq. 6), thus only the relative response is important for such kind of sensor.

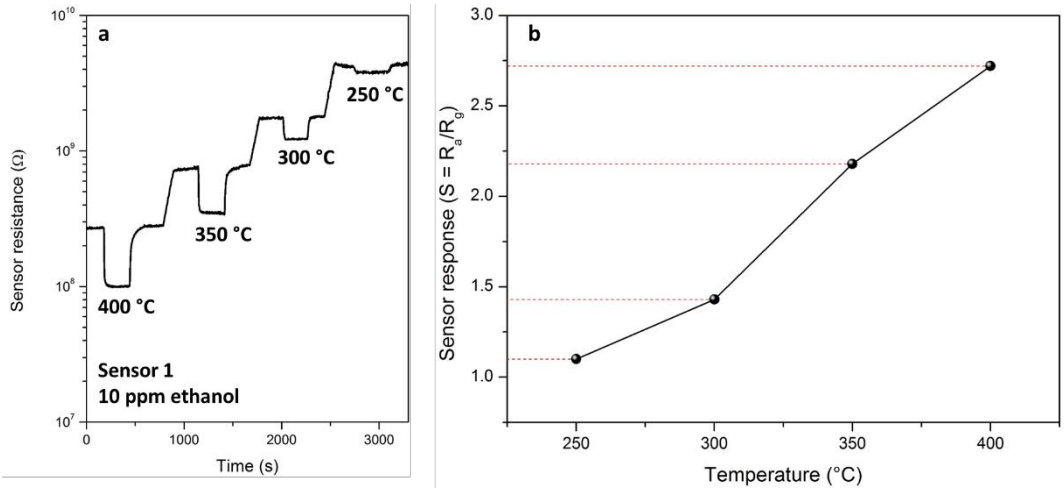

Figure 28: Sensor responses toward 10 ppm of ethanol at different temperatures. Experimental data (a) and relative extrapolated responses (b).

2.5.2. Response and recovery times

Even in this case the response and recovery times were assessed at the working temperature of 350 °C by normalizing the response amplitude between 0 and 1 and calculating the elapse time from between the 10 % and 90 % of the transient time.

The results exposed in Figure 29 exhibit a quite fast sensor response of about 10.3 s; nevertheless, it is about 3 times higher than the response time toward acetone (about 3.6 s). This different behaviour can be attributed to the different affinity between Nb_2O_5 sensing film and the target gas. In fact, such sensing film achieves the best response toward acetone turning out to a faster reaction. The same situation can be observed for the recovery time, which is reached after about 71.5 s while after 48.8 s for acetone cases.

Nonetheless, the results are promising and the sensor achieved suitable response time, faster enough to be implemented on portable measuring systems.

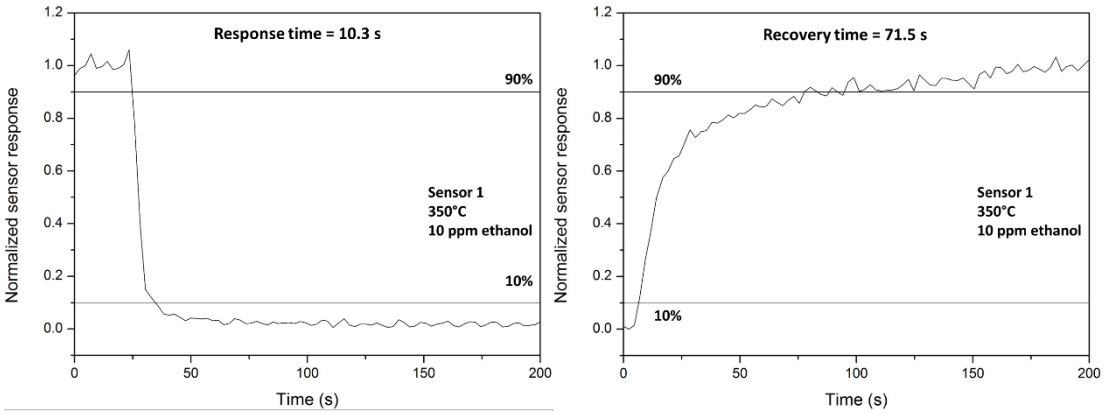

Figure 29: Response time and recovery time for sensor 1 toward 10 ppm of ethanol.

2.5.3. Sensitivity toward ethanol

Another important difference observed during the ethanol sensing was the maximum concentration X_{max} of the sensor before reaching the saturation. In fact, to assess the sensitivity toward the ethanol and evaluate the relative calibration curve several different ethanol pulses were added to the carrier gas up to 400 ppm, as reported in Figure 30. The linear response was observed until 50 ppm, and then a gradual saturation effect is exhibited up to 400 ppm. For acetone case, the saturation was observed for concentration of about 12 ppm and an X_{max}, which lead out from a linear fitting response, of 3 ppm. The comparison of these two results shows a drastic changing in behaviour of the sensor and it can be attributed to the different affinity to the chemi-adsorption sites located onto sensing film surface. In fact, ethanol reacts with the surface O^- as follow [52] [51]:

$$C_2H_5OH_{(vap)} + O^-_{(ads)} \rightarrow CH_3CHO_{(ads)} + H_2O + e^- \quad \text{eq. 29}$$

$$CH_3CHO_{(ads)} + O_{(lattice)} \rightarrow CH_3COOH_{(vap)} + V_O \quad \text{eq. 30}$$

Thus, a ethanol molecule reacts with a single O^- adsorbed onto sensing film surface releasing an electron to the conductive bond. On the contrary, a acetone molecule requires $8O^-$ to react, as described in eq. 20. Therefore, the sensing film is able to interact with a higher ethanol concentrations with respect to acetone ones.

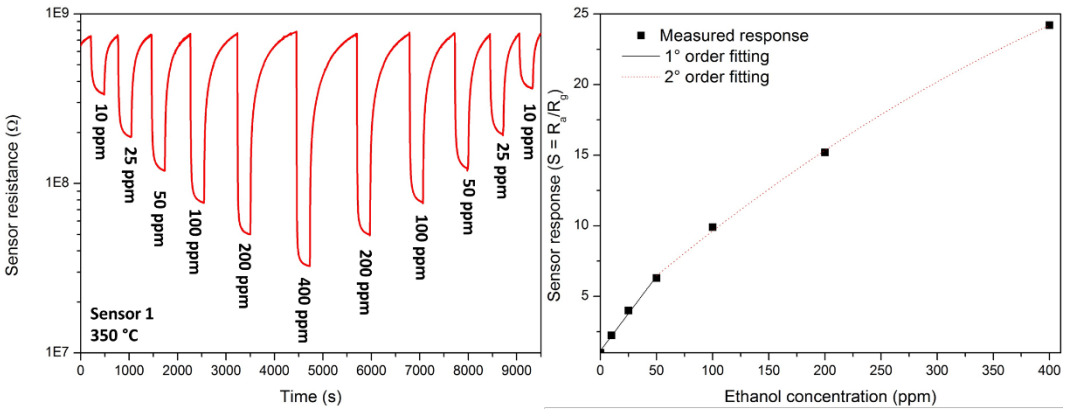

Figure 30: Responses toward different ethanol concentrations and relative calibration curve.

Table 14: 1° and 2° order fitting parameters extrapolated by calibration curve in figure 30.

	Sensor 1	
Coefficient	**1° order**	**2° order**
a	1.147	3.0667
b (ppm^{-1})	0.105	0.0699
c(ppm^{-2})	-	-4.28×10^{-5}
X	0-50	50-400

The possibility to detect ethanol concentrations higher than 400 ppm makes the employment of such prototype suitable for breath test analysis to assess the BAC of the drivers. In fact, the maximum concentration of ethanol in blood, allowed in most countries, cannot exceed the 0.05%. According to equation 25, it turns out that the 0.05% for BAC correspond with 130 ppm in BrAC. Therefore, a suitable alcohol test requires being able to detect ethanol concentration up to 200 ppm at least.

In addition, the first and second order fitting curves were extrapolated by the collected data in order to obtain an empirical correlation and the coefficient are listed in Table 14. It was observed that the linear fitting is verified for concentrations up to 50 ppm, thus a gradual saturation occurs. It is worthy to be note that the second order fitting is not able to describe the concentration lower than 50 ppm, then eq. 31 and eq. 32 describe the response trend only in specific concentration ranges

$X = 9.52\ (S-1.15)$ for $X \leq 50$ ppm eq. 31

$X = 817 - \sqrt{738281 - 23356\ S}$ for $50 \text{ ppm} \leq X \leq 400$ ppm eq. 32

Furthermore, the test consisted to pulse the different ethanol concentration from 10 ppm to 400 ppm then reducing again to 10 ppm following the same steps. In this

way, it was possible to give a first estimation about the sensor stability and repeatability as well. The results show good stability since R_a remains almost the same with a value of about 756 MΩ with a standard deviation of about 4 MΩ. regarding the repeatability, the responses show a maximum response variation of about 0.07 for measurements performed at the same ethanol concentration.

2.5.4. Sensor stability

As last sensor characterization, the stability was assessed fluxing 10 ppm of ethanol inside the test chamber at regular intervals. An example of five pulses is showed in Figure 31.

As already confirmed for acetone sensing and from the previous sensing test, even for ethanol an excellent stability is observed by such sensor and no significant offset as well as hysteresis effects were noted. Such results are also confirmed by the extrapolated data in Table 15. Actually, the baseline resistance R_a shows an average value of about 735 MΩ ± 20 MΩ, while the response S = 2.19 ± 1, confirming the excellent results.

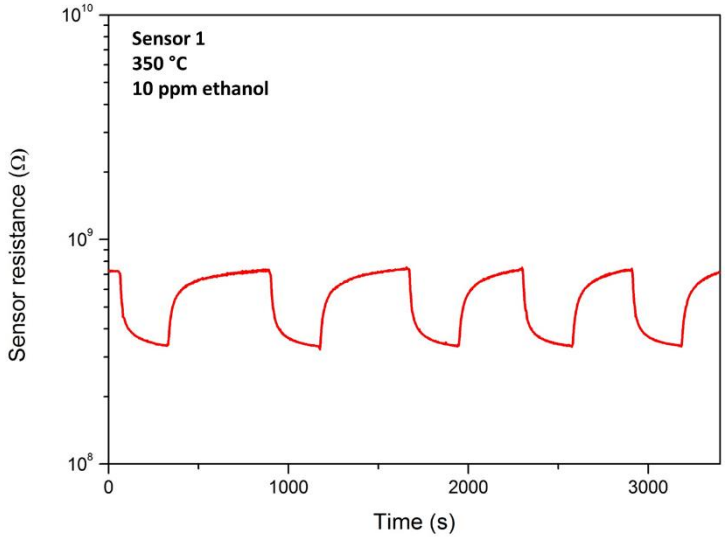

Figure 31: Responses toward different ethanol pulses at the same concentration (10 ppm).

Table 15: Stability results extrapolated by figure 31.

	Sensor 1		
	R_a	**R_g**	**S**
μ (MΩ)	735	334.1	2.19
σ (MΩ)	20	1.9	0.01
ε	2.7%	0.5%	0.4%

2.5.5. Ethanol breath measuring system

The gas sensor developed and characterized in this dissertation requires a suitable measuring system to be interfaced. It should be portable and guarantee an appropriate heating control since the working temperature is an important factor for the sensor performances. Moreover, it must provide response results compared to the ones obtained with the equipment employed for the gas sensing characterization. In this section, a first prototype is proposed; nevertheless, further improvements and characterizations are on-going in order to develop a suitable and portable breath measuring system.

First, in Figure 32, it is shown the block diagram of the proposed measuring system and it is formed by a sensor board, which contains the sensor conveniently connected to the circuits elaborated for both the control of the working temperature and for measuring the resistance variation in presence of the target gas. Such system is controlled by a micro-controller off-the-shelf Teensyduino 3.2, which drives the heater as well as the LCD display and reads the resistance. The battery aliments the system and its duration is strongly related to the heater. While the sensing element has been deeply characterized, in the next subsection a detail description of the sensor board and its relative performances is provided.

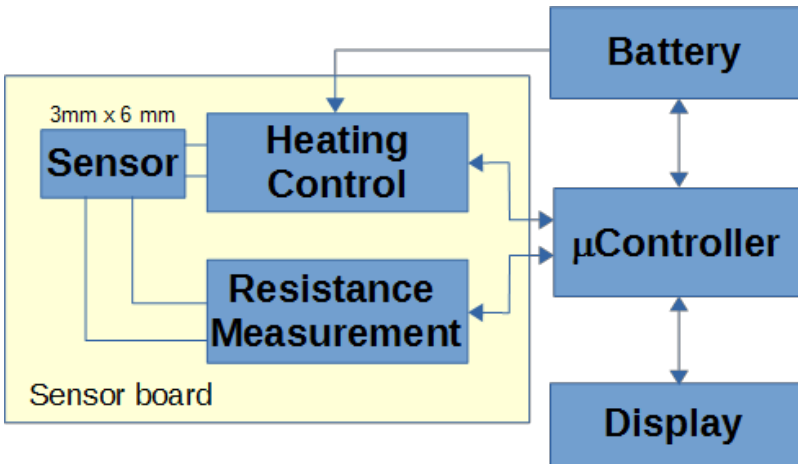

Figure 32: Block diagram of the proposed measuring system.

2.5.5.1. Sensor board

The Teensyduino 3.2 controls the two main components that form the proposed measurements system:

- *Heating control system*
- *Resistance measurement system*

The first component, the heating system, is required in order to maintain the working temperature at 350 °C and the relative circuit is shown in Figure 33. It involves the Pt heater, located on the bottom of the sensor substrate, for heating the sensor itself and, at the same time, as temperature probe by its temperature

coefficient. In particular, it involves a micro-controller Digital to Analog Converter (DAC) output in order to set the suitable heater current by the operational amplifier U1A, the current sense-resistor (R_s) and the current boost bipolar transistor Q. In parallel, the operational amplifier U1B is employed in order to measure the voltage drop across the heater (R_h). It is mounted in a differential amplifier configuration with the analog channel A0 of the micro-controller Analog-to-Digital Converter (ADC).

Such circuit allows to measure the heater resistance, thus the sensor working temperature. In particular, the implementation of a closed-loop temperature control software guarantees a stable working temperature at 350 °C with an uncertainty of about 10 °C, by means of a hysteresis approach. In order to reduce the power consumption and guaranteeing a higher amount of measurements, such system is designed to switch off the heater current with a frequency of about 0.1 s. In this way, it is possible to leave the substrate at a nearly constant working temperature.

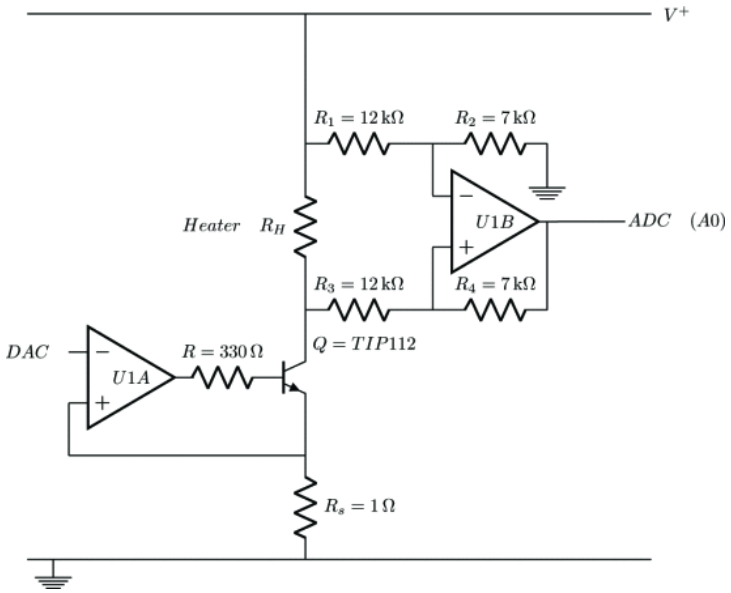

Figure 33: Electronic circuit for the heating system.

Regarding the resistance control circuit, it employs two operational amplifier as exposed in Figure 34. In particular, the system allows the measure the resistance of the sensor by forcing a known and constant voltage across it and measuring the related current flowing across the sensor itself. This is possible involving the first operational amplifier (U2A) as transimpedance circuit, which works with a feedback resistance R_1 of 10 MΩ. From the previous sensor characterization, it was observed that the sensor resistance is comprised in the range of 20 MΩ up to 1 GΩ, then a current in the range of few nanoamperes is expected. For such reason only a low-bias operation amplifiers is required. The employed sensor voltage ΔV is fixed at 1.14 V, controlled by the voltage reference U_2 (V_{ref} = 2.5 V) and a voltage divider (R_3 and R_4). Actually, the second operation amplifier (U2B) is employed as voltage buffer to avoid coupling the transimpedance amplifier with the microcontroller digital noise. Moreover, the output voltage is measured by means of the analog

channel A1 of the microcontroller ADC, which guarantees a resolution of 16-bit. Such output voltage is inversely proportional to the sensor one, following eq. 33

$$V_{out} = V_{bias} - \frac{R_1}{R_x} \Delta V \qquad \text{eq. 33}$$

Where V_{bias} is the voltage at the non-inverting input of A2U. Subsequently, at resistances higher than about 2 GΩ lead to a saturation of the output voltage at the V_{bias}, while for resistance lower than approximately 10 MΩ it saturates at the ground rail.

The first operational amplifier is characterized by stray currents and the current in the order of few pA. Additionally, the voltage offset is of the order of few millivolts. Since the system works for resistance up to 1 GΩ, all these components, even if characterized by small dimensions, they can affect the measurement performances. For this reason, the micro-controller firmware was implemented with a calibration procedure in order to avoid the problems related to both parasitic currents and offset.

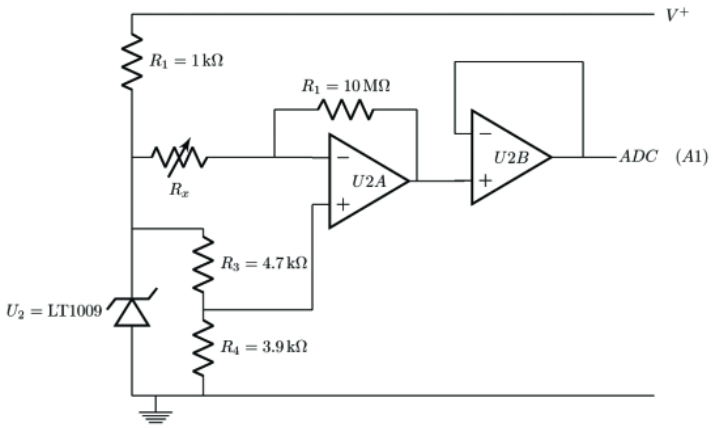

Figure 34: Electronic circuit of the resistance measurement system.

The following preliminary system control characterizations were performed separately for both heater and resistance measurements in order to assess their performances and evaluate their accuracy.

2.5.5.2. Heater system characterization

As first characterization, the heater system was tested in order to control if it is actually able to control and maintain the sensor temperature at the required value with an acceptable accuracy. The characterization was carried out by placing a thermocouple in contact with the gas sensor substrate and measuring the temperature variation by forcing the Teensyduino to maintain the heater resistance in the range between about 4 Ω and 12 Ω. In Figure 35 is reported the temperature measured by thermocouple as function of the resistance requested by the heater and achieved by the scaled measurement carried out by the micro-controlled ADC (Channel A0). The used thermocouple measures is able to measure the temperature

with an uncertainty of about 2 °C while the software that controls the sensor resistance reports measurements with an uncertainty in the order of 0.05 Ω. Nevertheless, the relation between temperature and resistance obtained in Figure 35 is different with respect to the one obtained for a pure Pt material, according to Calendar-Van Dusen equation. Actually, the A coefficient, employed in such equation for pure Pt, is about 3.9×10^{-3} K^{-1}, while for the heater case is about 8×10^{-3} K^{-1}. This difference is to attribute to the porosity structure, which characterizes the Pt heater. The result of the quadratic polynomial fitting, by using the Calendar–Van Dusen relation, is also exposed in Figure 35 with a green line.

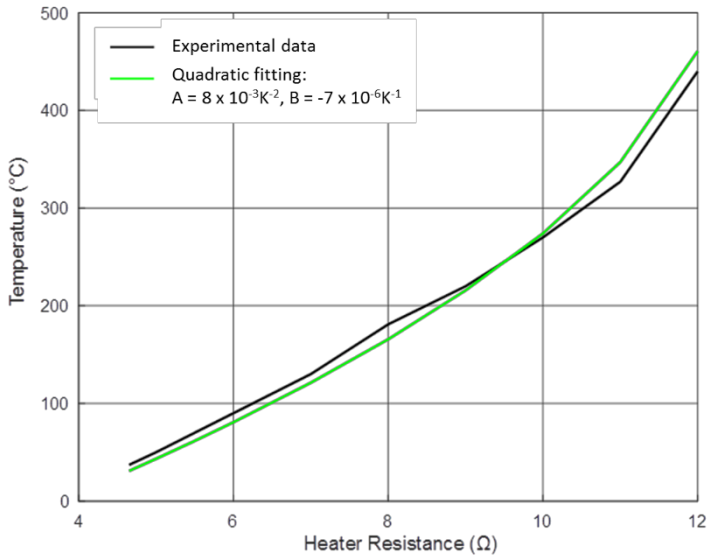

Figure 35: Temperature measured at different heater resistances by the proposed measuring system.

Furthermore, even the power requirement to heat and maintain the sensor at the optimal working temperature was characterized; since the sensor should work at 350 °C in order to guarantee good performances. Examples of measured transient with heater resistance, sensor resistance and the current required by the battery are exposed in Figure 36. First, the warm-up takes less than 5 s to reach the set temperature employing a current in the order of 0.6 A. Then, the software keep the set temperature, maintaining the required resistance, by chopping the involved current, in order to decrease its average consumption. In this specific case, the heater resistance is about 10 Ω and, according to Figure 35, it is almost 300 °C. Regarding the measured sensor resistance, the software saturates at about 2.2 GΩ, showing a decrease in resistance as a function of the increase in temperature by the heater.

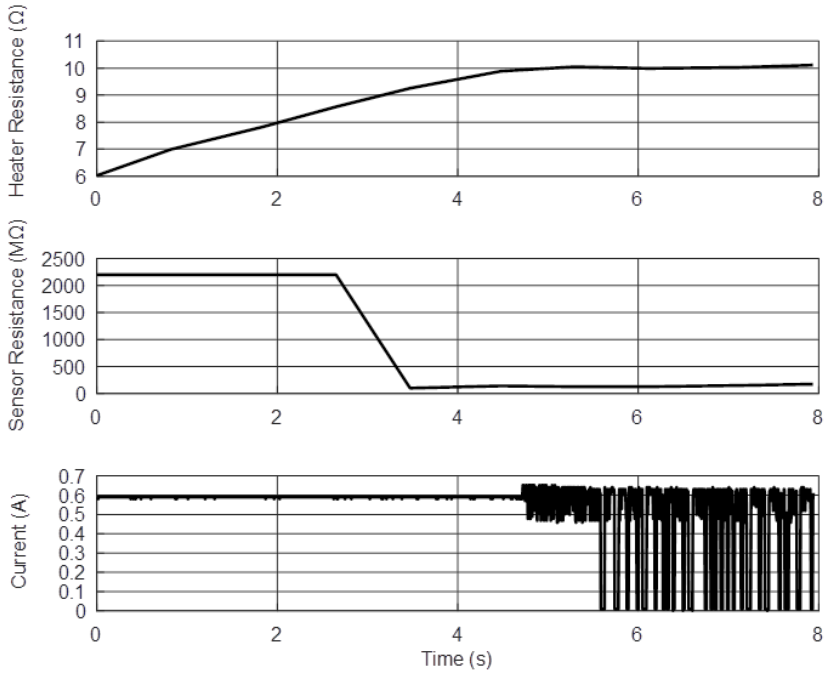

Figure 36: Example of heating transient obtained during the characterization of the heater system.

To better appreciate the chopping of the current on power consumption, a period, after the heating transient was complete, is expanded in Figure 37. It is possible to observe that the chopping occurs after 130 ms, reducing the total amount of current of about 38%. Therefore, the system requires 0.6 A to reach the set resistance during the first 5 s, then about 0.4 A to maintain the temperature during the measurement time.

For this specific case and taking in consideration a measure time of about 10 s plus the warm-up period, the system requires about 2 mAh for each measurement. Therefore, involving a standard AAA battery, with 1000 mAh as capacity, it is possible to perform about 500 measurements. While, using an AAA battery with a capacity of 2400 mAh, turns out a battery life of about 1200 measurements. In both cases, the battery life was improved by the chopping approach employed in the heating system.

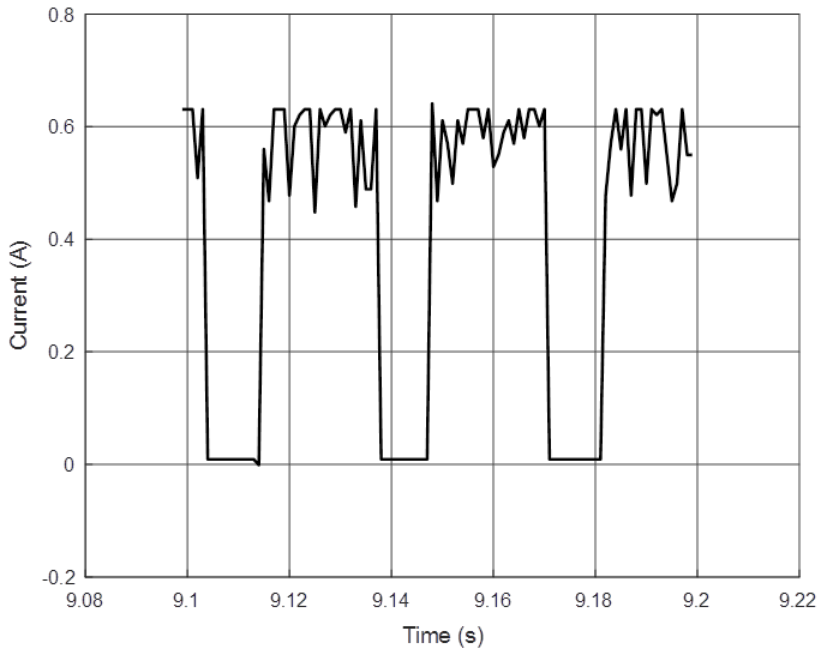

Figure 37: Expanded results of the heater transient obtained during the characterization of the heater system.

2.5.5.2. Resistance measuring system characterization

In order to assess the effective accuracy of the dedicated resistance measuring system, a series of precision resistor, with resistance values from 10 MΩ to 1.3 GΩ, were measured with the proposed system itself and the results were compared with the measurements carried out by a certified bench multimeter (Agilent 34411A). The results about the output voltage of the resistance measuring system measured by means of the micro-controller ADC at the analog channel A1 are exposed as blue line in Figure 38 while, the expected input-output characteristic of the circuit are represented by the black dash line. It is clear that there is an excellent matching between the expected and measured results.

Furthermore, even the relative error between the measurement obtained by the proposed sensor and the results carried out by the certified bench multimeter shows interesting results, as exposed in Figure 39. In fact, the extrapolated relative error is lower than 1 % for al the testes resistance from 10 MΩ to 1.3 GΩ and it is an excellent results considering the both the simplicity of the proposed circuit and the wide measurement range. It is also worthy to be mentioned that the Bench meter achieves accuracy in order of some percent points, making the results promising.

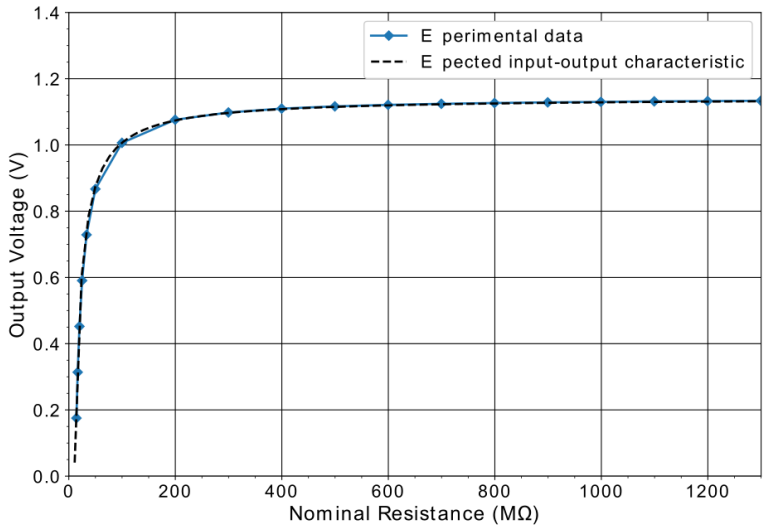

Figure 38: Output voltage of the resistance measurement system.

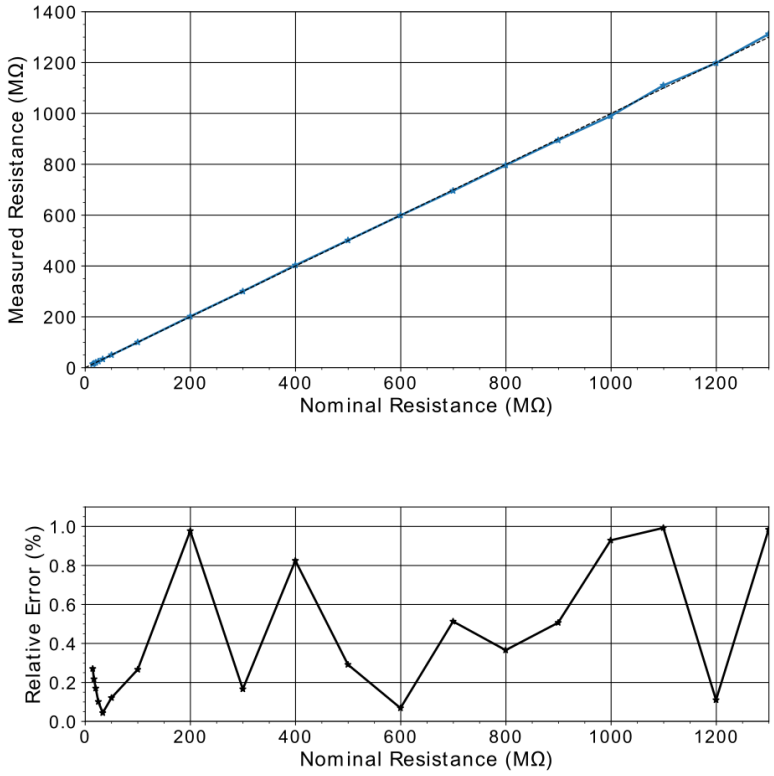

Figure 39: Accuracy of the system and the relative error.

To conclude, the proposed measuring system, characterized by small dimension, can be implemented with the conductometric gas sensor characterized herein and can guarantee hundreds measurements with a single battery. From the characterizations, it was observed that:

- *The heating system* is able to stabilize the heater to the required temperature with an accuracy of about 10 °C.

- *The resistance measurements* highlight that the sensor is able to measure resistance from 10 MΩ to 2 GΩ with a relative error of about 2%.

Thus, such measuring system reveals interesting performances, making it a promising solution for low-cost and portable device for ethanol sensing.

2.6. Hydrogen sensing

Nowadays, several studies are focused on developing gas sensors for hydrogen detection. In fact, an accurate monitoring of hydrogen is required in several fields such as automotive, nuclear energy, mining and for biomedical application as well [53]. In particular, high concentrations of hydrogen in human breath can be correlated to intestinal infection as well as lactose intolerance [54].

As described in section 2.4.4. Nb_2O_5 sensing films can obtain a small response toward hydrogen detection [55] [56] and, even in literature, some works suggest its implementation for this kind of applications. In order to improve the sensitivity toward H_2 several studies highlighted the possibility to enrich the employed sensing film with noble particles such as palladium Pd [57] and platinum Pt [37][58]. Actually, such elements are widely employed for specific H_2 reaction such as catalytic activity and solubility [59]. In fact, in presence of a hydrogen atmosphere, the H_2 molecules are dissociated and dissolved into such particles causing an increase of particles volume and a subsequent increase of the film resistance [60]. Subsequently, they migrates toward the particles interface reacting with the oxygen species present at the film surface. Finally, the electrons are released into the conductive band decreasing the sensing film resistance [60][61][62]. The H_2 sensing mechanism can be resume as follow:

$$H_{2(gas)} \leftrightarrow 2H_{(ads)} \quad \text{eq. 34}$$

$$2H_{(ads)} + 1/2O_2^- \leftrightarrow H_2O + e^- \quad \text{eq. 35}$$

$$H_{(ads)} + O^- \leftrightarrow H_2O + e^- \quad \text{eq. 36}$$

Furthermore, H_2 is an explosive gas characterized by a Lower Explosive Level (LEL) of about 3.6 mol. % at room temperature [63]. Such value decreases as a function of the temperature reaching 1.5 mol. % at 400 °C. Even if such concentrations are quite high for the sensor target, especially for breath test, for a safer point of view, low working temperatures are suggested. For this reason, two sensors, characterized by a thick sensing film, are proposed (Table 16). In fact, for working at lower temperatures it is important decreasing the sensor baseline resistance that, according to section 2.4.1., is strictly correlated to the film thickness. Furthermore, sensor 5 is obtained by a sandwich structure and the first Pt layer was thought to further reduce the effective sensor resistance at open-air environment.

Table 16: Details of the samples employed for hydrogen sensing.

Sample	RF-Power (W)	Dep. Time (min)	Thickness (nm)
4	500	60	900
5	500	60	1700

2.6.1. Temperature dependence of the sensor response toward hydrogen

Even in this case, the detecting of the optimal working temperature is the first and important characterization to carry out. As for acetone and ethanol, the target gas is added to the carrier flux by means of a dedicated mass flow meter at different temperature in the range from 400 °C to 150 °C in 6 steps. For each step, two pulses were fluxed inside the test chamber with a hydrogen concentration of 2000 ppm and the results are showed in Figure 40. The two sensors exhibit a similar trend since the shape and the deep of each pulse are comparable. Only at high temperature, in particular at 400 °C, it is possible to observe a better behaviour for sample 4 with respect to sample 5.

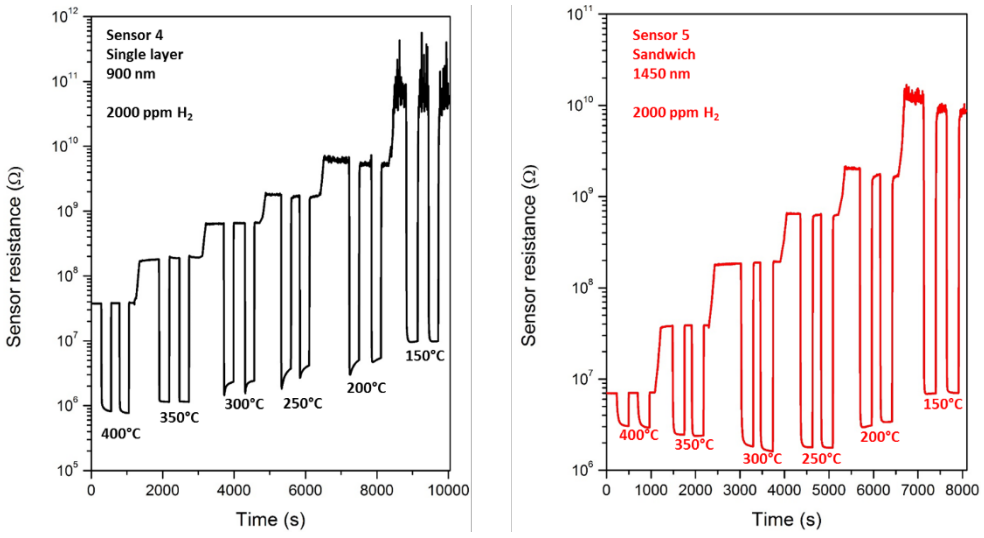

Figure 40: Temperature dependence of sensors 4 and 5 toward 2000 ppm of H_2

The extrapolated responses at each temperate are plotted in Figure 41 and an interesting trend can be observed. In fact, conductometric gas sensors require generally high temperatures in order to achieve suitable performances and a typical bell-shape curve is expected temperature dependence characterization. Nonetheless, both sensor 4 and 5 reach the best results at 150 °C with a response of about 5252 and 1329 respectively, which are two outstanding results for this kind of sensor.

Nevertheless, the temperature with the best sensing responses could be find out at lower temperature with respect to 150 °C here observed, but it is important to take in consideration two important points:

1. As exposed in Figure 42 the baseline resistances reach 52 GΩ and 9.3 GΩ for sensor 4 and 5 respectively at 150 °C. Such high resistance are not easy to measure for common multimeter, especially for ones implemented in portable devices.
2. The measurements carried out at 150 °C show a baseline resistance characterized by not negligible background noise, which can affect the measurements accuracy.

For these reasons, it was chosen 200 °C as working temperature for both sensors. This temperature can also guarantee an acceptable safe level since the LEL of the hydrogen at this temperature is about 3 mol. %

Moreover, it is possible to observe how sample 4, characterized by a thin film of about 900 nm achieves the best responses at each working temperature with respect to sensor 5 characterized by a sandwich structure. Such results can be correlated to the sensors film thickness since the sensor response mechanism is highly affected by the ratio between the depletion zone dimension and the film thickness (see section 2.3.)

Regarding the baseline resistance, sensor 5 reaches the lower value for all the temperatures. This results was expected since it is characterized by a thickness that is the double with respect sensor 4, however the sandwich structure does not provide any outstanding results with respect to a double layer, easier to obtain and cheaper.

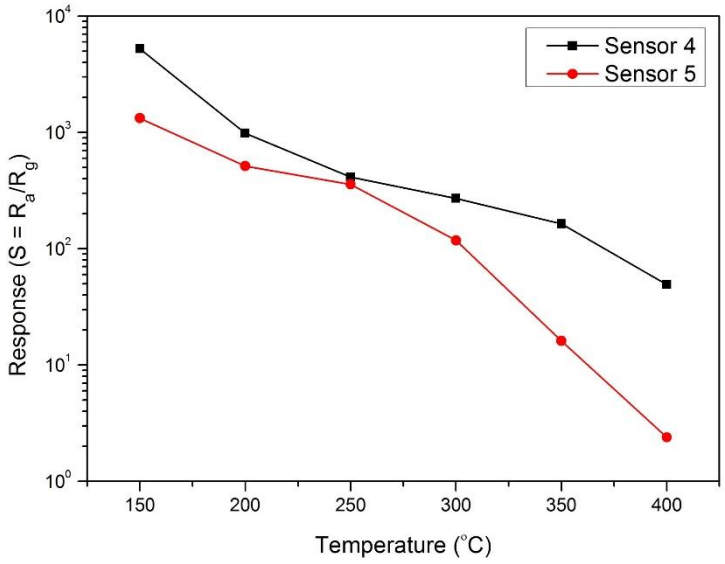

Figure 41: Responses at different temperature extrapolated by figure 41

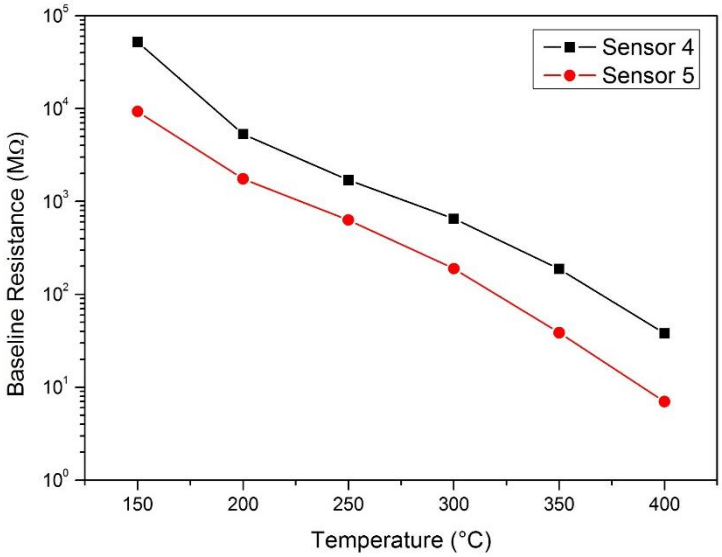

Figure 42: Baseline resistance at different temperature for samples 4 and 5.

2.6.2. Response and recovery times

The response and recovery times were evaluated as describe in section 2.4.2. and the overlapped curves are exposed in Figure 43 while the extrapolated results in Table 17. Even in this case the sensors were characterized at their working temperature (200 °C) and both of them show outstanding results with an identical response time of about 3.6 s and a similar recovery time, about 13.7 s and 15.8 s for sensor A and B respectively. These results, especially the recovery times, exhibit the best values with respect to the acetone and ethanol cases. This means that hydrogen molecules can react easily with the sensing film and fast measurements can be carried out.

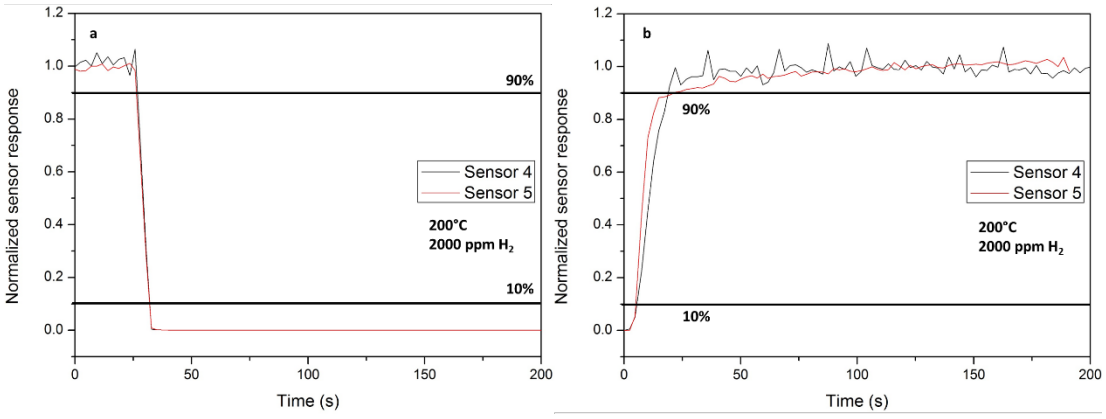

Figure 43: Response time (a) and recovery time (b) for samples 4 and 5 at 200 °C for 2000 ppm of H_2.

Table 17: Response time and recovery time extrapolated from Figure 43.

Sensor	Response time (s)	Recovery time (s)
4	3.6	13.7
5	3.6	15.8

2.6.3. Sensitivity toward hydrogen

After detecting the optimal working temperature and the relative sensor response, the two sensors were calibrated by measuring the sensitivity toward different hydrogen concentrations. For this characterization, hydrogen concentrations from 2000 ppm to 80000 ppm were pulsed inside the test chamber, as exposed in Figure 44, and the relative responses are plotted as function of the hydrogen concentration. Both sensors reach interesting results with responses of about 23000 and 9500for sensor 4 and 5 respectively for concentration of 80000 ppm. However, it is clear that sensor 4 obtain the better results with responses higher than the double with respect sensor 5.

Nevertheless, it is important to highlight that both sensor 4 and 5 do not exhibit any response toward hydrogen at low concentration. In fact, before performing the following characterization at the minimum concentration of 2000 ppm, preliminary test were performed and no response were observed at concentration from 10 ppm to 100 ppm. For this reason, the characterization started directly from 2000 ppm. The stomach diseases lead to a hydrogen concentration inside the human breath test up to 40 ppm, strongly lower than the minim detected by these sensors. However such diseases are also detected by fecal analyses where, in this case, the hydrogen can reach 2.5% [64]. Anyway, such sensor can be employed for further applications such as automotive or for energy storage where high concentrations play important roles.

Furthermore, such kind of enriched film are able to detect quite high H_2 concentration before reaching a complete saturation and. In fact, both sensors shows a linear response dependence toward the H_2 concentration until 10000 ppm, and then a saturation effect can be observed. This high adsorption rate can be related to the capability of noble element, as Pt, to be able to adsorb the hydrogen molecules into the bulk material of the surface aggregates [59] as well as to the catalytic effect of Pt on improving the O_2 species concentration onto sensing film by spill-over effects.

Nevertheless, sensor 4 exhibits a low variation from the linearity up to 40000 ppm, concentration that can assumed being the complete saturation level. In fact, from 40000 ppm to 80000 ppm the 2° order fitting cannot match with the measured responses. Regarding sensor 5, the responses exhibit two different behaviours before and after reached the 10000 ppm as detected concentration. Actually, for concentration from 10000 ppm to 80000 ppm the 2° order fitting is not able to describe the responses obtained for lower concentrations. However, also for

hydrogen the empirical correlation has been obtained employing the coefficient exposed in Table 18. It is also interesting observe that the intercepts obtained from such fitting do not pass through the axes origin because of their do not detect hydrogen at low concentrations.

Even for such calibrations, the linear and quadratic fitting were extrapolated by eq. and eq. 19, obtaining:

$$X = 1.2\ (S + 606) \qquad \text{for } X \leq 10000 \text{ ppm} \qquad \text{eq. 37}$$

$$X = 50809 - \sqrt{2512659610 - 112159\ S} \qquad \text{for } X \leq 40000 \text{ ppm} \qquad \text{eq. 38}$$

for sensor 4 and:

$$X = 2.9\ (S + 128.65) \qquad \text{for } X \leq 50 \text{ ppm} \qquad \text{eq. 39}$$

$$X = 119984 - \sqrt{17701198785 - 1737015\ S} \qquad \text{for } 10000 \text{ ppm} \leq X \text{ 80000 ppm} \qquad \text{eq. 40}$$

for sensor 5

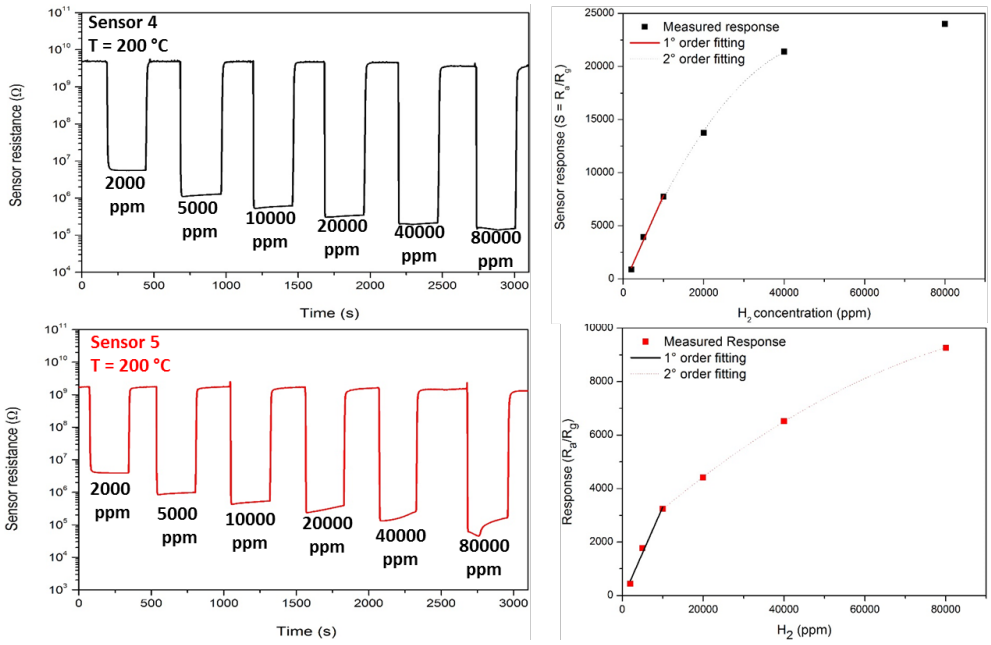

Figure 44: Responses toward different H_2 concentrations for both sensors 4 and 5 and relative calibration curves.

Table 18: 1° and 2° order fitting parameters extrapolated from the calibration curves in figure 45.

	Sensor 4		Sensor 5	
Coefficient	**1° order**	**2° order**	**1° order**	**2° order**
a	-606.67	-614.46676	-128.653	1902.66
b (ppm^{-1})	0.8465	0.90602	0.34394	0.13815
c(ppm^{-2})	-	$-8.9159x10^{-6}$	-	$-5.757x10^{-7}$
X_{max}	10000	40000	10000	10000-80000

As here exposed, sensor 4 exhibits the best results in term of sensitivity since it is able to detect high concentration of hydrogen providing interesting responses. Moreover, such sensor is easier to develop with respect sensor 5 in term of both process time and process cost. For these reasons sensor 4 was selected for the next characterizations.

2.6.4. Sensor selectivity

In section 2.4.4. sensor 2, obtained with the same parameters of sensor 4 regarding the Nb_2O_5 thin film, was characterized in term of selectivity by testing the sensor itself toward several different gases. For sensor 4, the presence of platinum aggregates onto the surface can cause a different sensor sensing toward the already measured gases. At this scope, sensor A was treated with different gases pulses in order to check the effective selectivity and even evaluate if worthy changes are present. Even for this characterization, a gas mixture containing 80% N_2 and 20% O_2 was used as carrier to transport the pulses of the target gases and the results are exposed in Figure 45.

An interesting selectivity of sensor 4 toward hydrogen is visible and only a negligible response toward CO_2 and NH_3 is detected. It is worthy to be note that the sensing toward both ethanol and acetone is drastically decreased. In fact, 100 ppm for both gases reach a response of about 1.1 meaning that the sensing film is no longer able to detect such gases.

The sensor sensing mechanism is based on the adsorption of the target gas by the surface active site and the subsequent release of O_2 previously adsorbed in order to modulate the depletion zone and decrease the film resistance. For making possible this mechanism, the sensing film has to be affine to the target gas in order to be able to adsorb the gas itself. While Nb_2O_5 has an important sensibility toward acetone and ethanol, pure Pt is not able to react with these gases. Therefore, the second Pt plasma deposition and the following heat treatment generate surface agglomerates, which lead to a reduction of a sensing zone towards such gases. To sum up it is clear that such sensor is extremely selective toward H_2 and no effective competitor were detected, which could lead to false positive results.

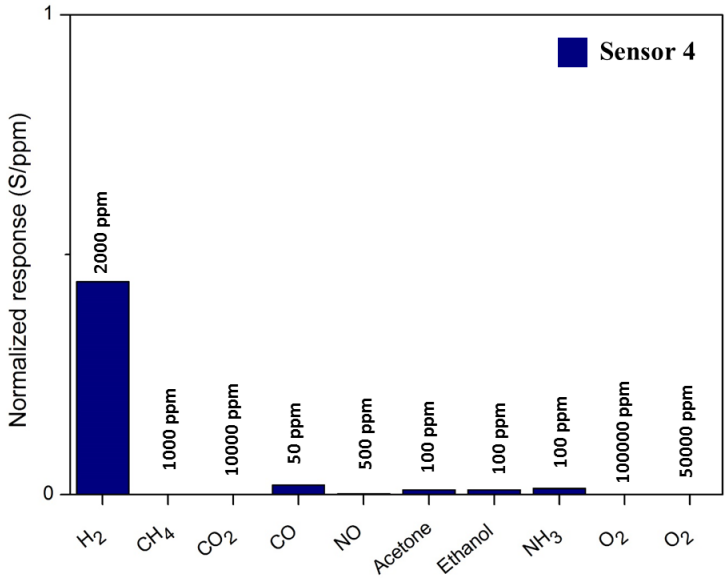

Figure 45: Normalized responses toward different gases obtained by sensor 4.

2.6.5. Sensor Stability

As last characterization, the stability of the sensor was assessed after the exposition toward several different gases and the wide employment during the whole characterization.

The sensor was located inside the test chamber and the responses toward several hydrogen pulses were collected and four repetition are exposed in Figure 46 and the extrapolated results are listed in Table 19. The working temperature was always 200 °C and the pulses were formed of 2000 ppm of hydrogen. No visible hysteresis, offset or general variation are observed and an average response of about 910 was calculated with a variation of about 1%. This is a quite good result since the response exhibits outstanding values with low and acceptable variations. Even R_a and R_g shows stable value over time of about 5 GΩ and 5.5 MΩ respectively. Regarding the variation, R_a shows about 2% due to the noisy base line resistance, which slightly reduce the response accuracy.

In the previous calibration, the sensor response was about 892 that is similar that the one here described and is in the range of calculated variation. This is an important result since Pt is able to adsorb H_2 into the bulk material, which cause a material swelling leading to sensor damages [59].

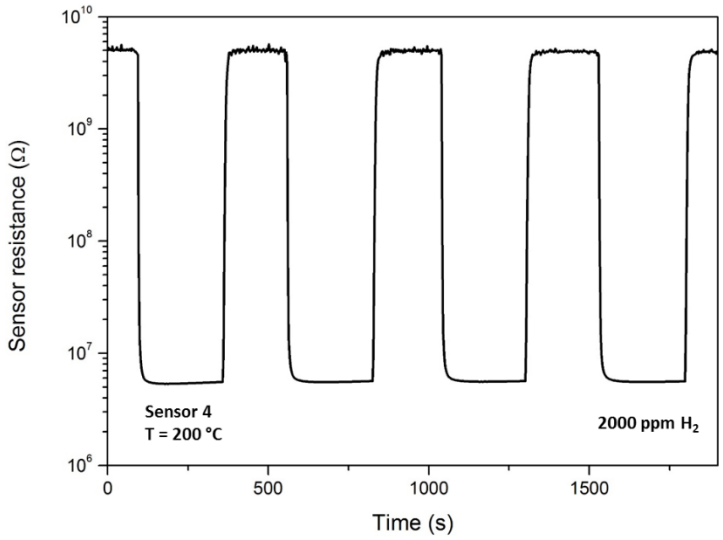

Figure 46: Responses toward different H_2 pulses at the same concentration (2000 ppm).

Table 19: Stability results extrapolated by Figure 46.

	Sensor 4		
	R_a	R_g	S
μ (MΩ)	5015	5.55	910
σ (MΩ)	20	1.9	13.5
ε	2%	1%	1%

2.7 Conclusions and future works

To conclude, different conductometric gas sensors, characterized by Nb_2O_5 thin film and Nb_2O_5 thin film enriched with Pt nanoparticles, has been developed and characterized. The Nb_2O_5 thin films were obtained by reactive plasma sputtering employing different deposition parameters, in order to modulate the thickness and morphology of the sensing films. Regarding the samples enriched with Pt, the nanopoarticles were obtained by a second magneto-sputtering deposition followed by a heat treatment in controlled atmosphere. A pure Nb_2O_5 sensing film is suitable for the detection of acetone and ethanol while introducing Pt nanoparticles the response turns toward the hydrogen detection. Starting with pure Nb_2O_5, it was observed that the sensing film thickness play an important role on sensing response toward acetone. Actually, sensor 1 and 3, characterized by compact films with thickness of about 200 nm and 160 nm respectively, exhibit higher responses with respect to sensor 2, which is characterized by a and columnar film with a thickness of about 900 nm and formed by vertical rods with a diameter of about 15 nm. The microstructure affects also the response time and recovery time of the sensors response. In fact, thin and compact layers allow a faster response since the target

gas can react immediately with the sensing sites onto film surface, with a response time of about 3.6 s. On the contrary, a thick and columnar structure makes the response slower, since the target gas molecules take time to diffuse inside the film microstructure and react with the sensing sites onto surface film. In fact, was evaluated a response time of about 46.1 s. Another consideration regarding the film thickness, it can also affect the optimal working temperature. Actually, sensor 1 and 2, characterized by the thinner films, reach the optimal working temperature at 350 °C while sensor 2 at 300 °C. Nevertheless, a porous morphology can guarantee a linear response toward acetone up to10 ppm and maximum concentration higher than 40ppm before reaching a complete saturation. Actually, a compact thin film can detect acetone up to 3 ppm for obtaining a linear response and a complete saturation was assessed at 12 ppm. Anyway, diabetes diagnosis are provided by breath test by detecting acetone concentration, which reaches values of about 2 ppm. Therefore, all samples, specially sample 1, can be implemented for breath test devices. Last characterizations were carried out in order to assess the stability and selectivity of the samples and the results show excellent results achieved by Nb_2O_5 sensing film. In fact, the sensors can be employed several times with a response deviation lower than 2%. About the selectivity, they give a sensible response only toward acetone and ethanol. The latter is not formed in metabolic processes; therefore it does not interfere with the breath analysis. Finally, the sensor reproducibility was evaluated for sensor 1 since it achieved the best results in terms of sensitivity. In this case, other three samples were obtained by plasma deposition using the same parameters of sensor 1 and the responses toward different acetone concentrations were evaluated. The results were quite reproducible with a maximum relative error lower than 2%.

Sensor 1 was also characterized toward ethanol sensing and the results show quite good results but lower with respect to the acetone ones. Nonetheless, the saturation is reached at drastically higher ethanol concentration, up to 400 ppm. For this reason, such sensor can be implemented for ethanol breath test, since the concentration in play can reach 300 ppm. At this scope, an ethanol breath measuring system has been developed. Herein a first prototype based on a Teensyduino is exposed and the characterization shows a good heater stability with an accuracy of about 10 °C and a capability of the system to measure resistance up to 2 GΩ, with a relative error lower than 2%. These features reveal interesting performance and further efforts can lead to the implement of such measurement system for effective low-cost portable devices.

Adding Pt nanoparticles the selectivity turns toward hydrogen detection and the sensors exhibit excellent results in term of response, response time and saturation, since it is reached for concentration higher than 80000 ppm. However, it is worthy to be mentioned that the such sensors exhibit low sensitivity since they does not give any response for low H_2 concentrations. For this reason, they cannot be employed for breath analysis, since the H_2 concentration generated by stomach diseases, reach about 40 ppm inside the human aerosol. Nevertheless, such diseases are also detect by fecal analyses, where the H2 concentrations detected are higher

than 2.5%. Furthermore, the excellent results in term of response make such sensor suitable also for application where high H_2 concentrations are present.

Future works are lead toward the development and characterization of Nb_2O_5 thin film enriched with Pt nanoparticles characterized by a thinner film in order to increase the sensitivity making possible the detection of low concentration of H_2. In this way, it is possible to implement such sensor for breath test addressed to detect stomach diseases.

Chapter 3

Electrochemical measurements to predict the antifungal effects of nanostructured thin films.

This chapter partially contains materials from previously published work of the author [65]

In this chapter a combination of electrochemical impedance spectroscopy (EIS) and Inductively Coupled Plasma (ICP) spectrometry was involved in order to assess the corrosion protection effect as well as anti bacteria and anti fungal properties of novel SiO_x thin films enriched by Cu particles. The idea, which this proof of concept is based on, is to correlate the EIS measurements (a common technique generaly used for assessing the corrosion protection by protective coatings) with respect to the ICP quantitative analyses related to the Cu ions release. As a matter of fact, Cu acts as anti-bacteria element, then its gradual release can lead to a beneficial effect on infection prevention. This effect can be exploited for the realization of protective coatings for biomedical applications where the infections are an important deal to prevent.

In this study, a double layer coating, formed by a thick Cu layer and a second SiO_x layer enriched by Cu nanoparticle, has been deposited and characterized by the already cited combined EIS and ICP method. Observing the preliminary results, a promising trend between two involved tecniques has been detected and the SiO_x/Cu layer is a fascinating alternative that could be involved in biomedical applications.

3.1. Introduction

Nowadays, fungi and bacteria proliferations and infections remain an important factor responsible of clinical complications despite the high hygienic level achieved by the western hospitals [66][67]. In fact, it has been estimated a continuous growth of infection cases in the last twenty years, in particular towards immune-suppressed patients who are the main targets [67]. Therefore, despite the important achievements reached by the modern medicine, new efforts are mandatory to prevent potential fungi and bacteria outbreaks in order to reduce the mortality rate as well as the healthcare-system costs [66][68]. A possible solution to overcome

this challenge is the implementation of protective coatings, as SiO_x coating characterized by a gradual and controlled Cu ions release, to apply on medical devices and for safe packaging.

SiO_x coatings are widely investigated in several studies since they are characterized by unique features like barrier properties (important for packaging application for reducing the gas permeation through the polymers) [69], and anticorrosion effects (tested on different metals as Mg and Fe) [70]. Furthermore, such films are optically transparent, water resistant and microwaveable.

Copper (Cu) additionally is a well-known element having anti-bacteria and anti-fungi effect, which is already involved in several studies regarding the realization of protective coatings for biomedical purposes [71][72][73]. In particular, such investigations highlight the capability of the copper nanocluster to reduce the proliferation of different bacteria, such as E. coli and S. aureus. Furthermore, Cu is an essential micronutrient element for human health, with multiple metabolic functions but its eventual excess can lead to cellular damage and other diseases [74]. Figure 47 is an example of three anti-fungi polymeric coatings with Cu nanoparticles (CuNPs). The results show a drastic reduction of colony forming unit (CFU) after 4 hours of yeast incubation [73].

According to literature, several different metal clusters were used to obtain functionalized SiO_x coating, such as silver [75][76][77] and copper [72][77][78], all of them obtained through a sol-gel procedure from the reaction of a monomer, e.g. TetraEthyl OrthoSilicate (TEOS), in liquid phase heat treated at 500 °C for some hours. Such method leads to several advantages, in fact, it is easy to realize both in-lab scale experiments and in-large scale ones and no expensive equipment are required. Unfortunately, not all the substrates can be treated at high temperatures avoiding structural degradation and the subsequent worsening of mechanical properties. As an example, polymers, materials widely used for packaging and for the realization of medical devices as they have suitable mechanical properties and a low commercial price, are sensible to thermal treatment with the abovementioned consequences.

An interesting alternative that would overcome this problem is the realization of SiO_x thin film coatings through a low pressure plasma enhanced deposition (PECVD). While in chapter 1 the plasma depositions through magneton sputtering and reactive sputtering are reported, in this case the deposited coating is achieved by the presence of a monomer in gaseous state vaporized inside the deposition chamber that, by means of the electron bombardment, reacts forming the polymer [79]. A more detailed description is present in section 1.5.2. In addition, PECVD works at low temperature (lower than 60 °C) reducing the process time (maximum 1 h is required, depending on the final thickness). To obtain the presence of Cu nanocluster embedded inside the SiO_x coating it is possible to combine the PECVD method with the magnetron sputtering one, using specific discharge conditions. From such combination, it is possible to sputter Cu particles form the Copper target during the realization of the SiO_x network, obtaining a nanostructured film [80].

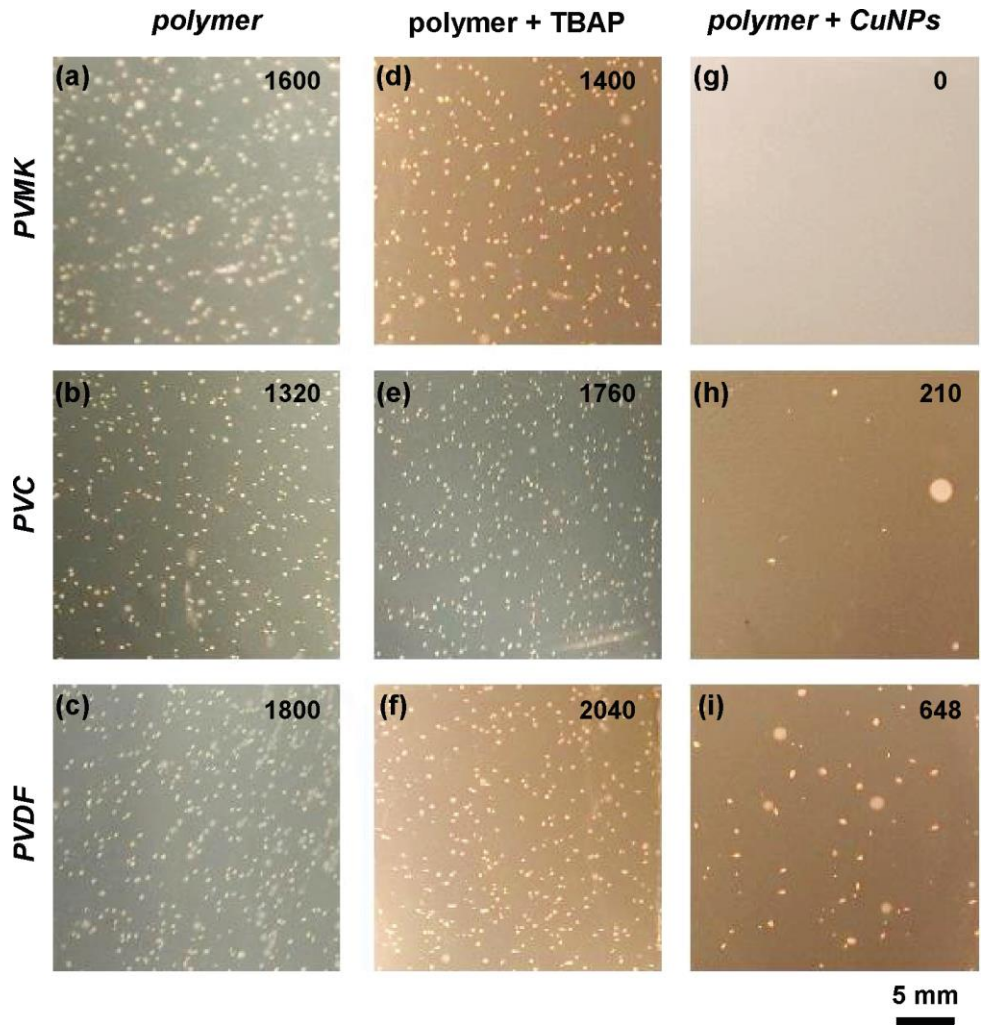

Figure 47: Optical images of three different polymers (PVMK, PVC and PVDF) bare (a, b and c), with TBAP (d, e, f) and with CuNPs (g, h, i) after 4 h of yeast incubation [73].

Moreover, by exploiting a PECVD equipment, it is possible to modulate the film chemistry in function of the final purpose. Actually, the film chemical properties are strictly affected by the O_2 pressure inside the deposition chamber and by the RF-power applied during the discharge. Higher O_2 pressure and higher RF-power generate a diamond-like coating film, with better barrier properties that are suitable for corrosion purposes. Such structure is characterized by high stability even in aggressive environments, making the obtained film not suitable for a slow and controlled Cu release for antibacterial applications. Otherwise, by applying lower RF-power and lower O_2 pressure, the coating would be characterized by the presence of more organic fractions, obtaining a $SiC_xH_yO_2$ layer. This coating presents lower barrier effect, because of its higher affinity to the aqueous compounds, thus it gradually degrades in aggressive environments and, subsequently, a Cu release occurs. Furthermore, by plasma deposition, it is possible to obtain a multilayers structure simply shifting the discharge condition, avoiding to handling the samples between every single step.

For the aim of this work, a compromise between corrosion protection and Cu release is mandatory since, for future applications, a gradual and controlled degradation is requested in order to obtain an anti-fouling effect guaranteeing a suitable corrosion protection over time. For this scope, a double layer thin film is studied in order to obtain a coating capable to release copper ions by gradual degradation. The first layer is formed by pure Cu and it is obtained by magnetron sputtering. The second layer, the main important one, is obtained by PECVD in a mixed sputtering mode in order to deposit SiO_x layer, containing copper clusters. The double layer has a double effect. First, it is necessary for having a lower conductivity layer in order to perform the impedance measurements. Second, it can be a solution in order to have a Cu source, improving the antibacterial effect.

The corrosion protection and Cu release effect are assessed in a simulated biological environment, employing Hank's balance salt solution as electrolyte by the combination of two techniques:

- *Electrochemical impedance spectroscopy (EIS)* – this technique is widely employed for coating protection assessment due to its high versatility and easy realization [81][82]. Moreover, it is a non-destructive analysis, which can provide coating stability information over time [83].
- *Inductively coupled plasma mass spectroscopy (ICP)* – high sensitivity and high selectivity are mandatory for the Cu release analysis. In fact, Hank's balanced salt solution formulation counts several different inorganic salt in order to simulate the body fluids aggressivity. ICP technique provides confident results in the range of part per billion toward the target element.

Form the combination of these two measures it is possible to estimate a correlation between the corrosion protection, especially by the EIS module extrapolated at low frequencies range, and the effective Cu concentration released toward the solution over time. The expected SiO_x behaviour measured by the abovementioned combined approaches would emphasize, in principle, a higher impedance module value, related to high barrier properties, thus a better substrate corrosion protection toward the electrolyte. In this case, the Cu concentration inside the electrolyte is expected to be low since the high barrier effect would not allow to the Cu nanoparticles to dissolve. After a certain immersion time the EIS measurements would reveal a gradual coating degradation by the worsening of the impedance module. The expected Cu concentration measured inside the solution would follow the module trend over time. In conclusion, a Cu release prediction can be extrapolated by a single EIS analysis obtaining a concentration estimation.

3.2. Materials and methods

3.2.1. Film deposition processes

The Cu/SiO_x double layer structure was obtained by means of plasma deposition with the apparatus described in section 1.5.2 onto commercial standard microscope glass slide, previously cleaned with ethanol and air-dried, obtaining a double coated glass sheet, as exposed in Figure 48-b.

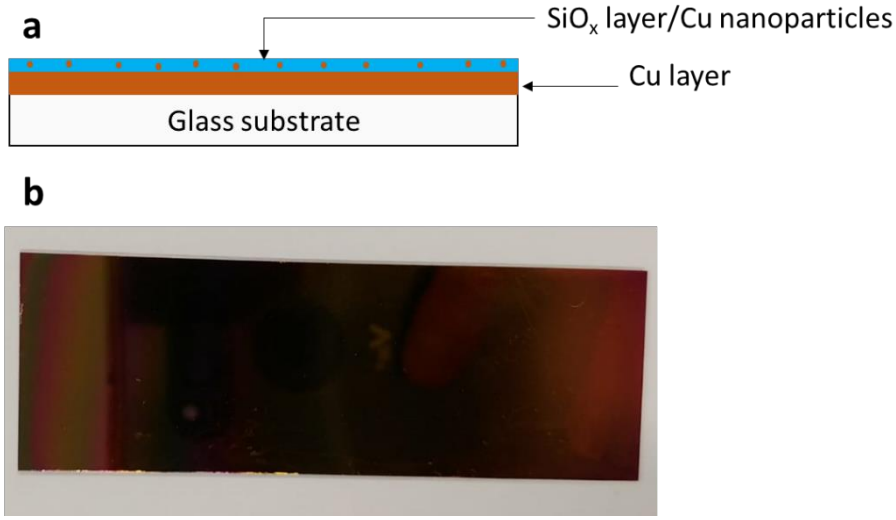

Figure 48: Schematic double layer structure (a) and effective result (b).

The structure of the samples, as exposed in Figure 48-a, involves a first layer in pure copper obtained, for both the samples, with a magnetron sputtering deposition, by using 200 W, as radio-frequency power at a frequency of 13.56 MHz. A copper target with 99.995% of purity was involved for the deposition for a total amount of time of 20 minutes. During such deposition, the discharging gas was composed by 50 sccm and 10 sccm of Argon and Hydrogen respectively. The latter is a reducing gas, used in order to avoid the formation of oxidised compounds. Therefore, in this case, no reactions occur inside the discharging atmosphere during the deposition but it involves only the target sputtering.

The second layer was obtained by means of PECVD as described in Figure 49. While for the realization of Nb_2O_5 sensors, in chapter 2, a reactive deposition method was exploited, in this case the deposition passes through a third reagent. As a matter of fact, for the realization of SiO_x layer an organic monomer is required and in this work TetraEthyl OrthoSilicate (TEOS) was used.

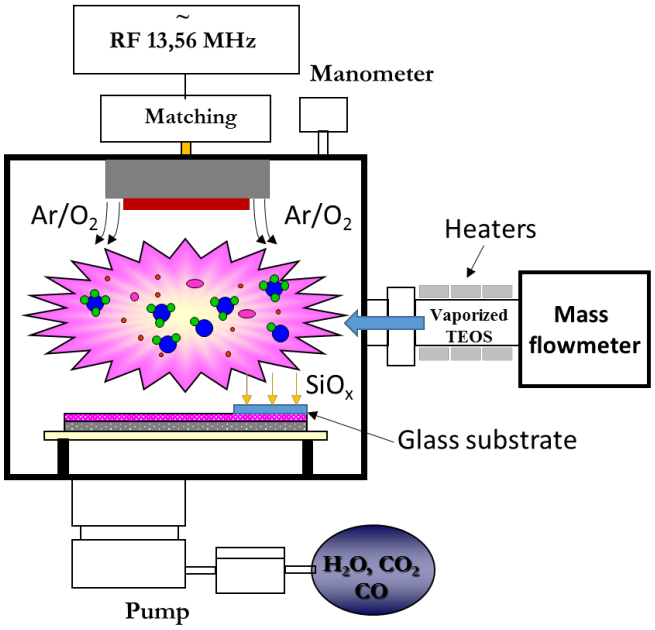

Figure 49: Schematic representation of PECVD involved for SiO_x deposition.

The vaporized TEOS flow was controlled by the mass flowmeter (model: MKS400-PR4000) located at the deposition chamber side (Figure 12). Unlike the other involved gases, such monomer needs to be heated since at room temperature it is a liquid. Therefore, the used mass flowmeter works at 90 °C, allowing the TEOS to evaporate and subsequently to flow inside the deposition chamber. In order to avoid the condensation of the vapour before it reaches the chamber, the gas inlet is heated by means of resistive heaters connected by a bench power supply. The necessity to keep the vapour in temperature along the entire path to the chamber does not allow to locate the gas inlet on the top (as for the other gases) but only from the lateral side, as exhibited in Figure 49. Such apparatus geometry creates a preferential SiO_x deposition zone inside the chamber, affecting the film thickness, which can be higher close the TEOS, as the reactive deposition starts as soon as the monomer flows inside the chamber. For this reason, the glass substrate is placed on the bottom anode as close such inlet as possible, as showed in Figure 49.

Several different reactions occur during the reactive deposition and a schematic outline is showed in Figure 50. The TEOS molecules are disintegrated by the electron bombardment inside the plasma glow forming three principal macromolecule groups:

- *Organic molecules:* they are created by the organic fraction presents in TEOS structure, they can react with both oxygen and hydrogen (the latter is obtained from CH_3 groups) forming gaseous organic molecules which are eliminated from the chamber by the vacuum pump
- *Inorganic Si-composed molecules:* they create the main structure of the SiO_x lattice.

- *Organic Si-composed molecules:* they can modulate the SiO_x film chemistry.

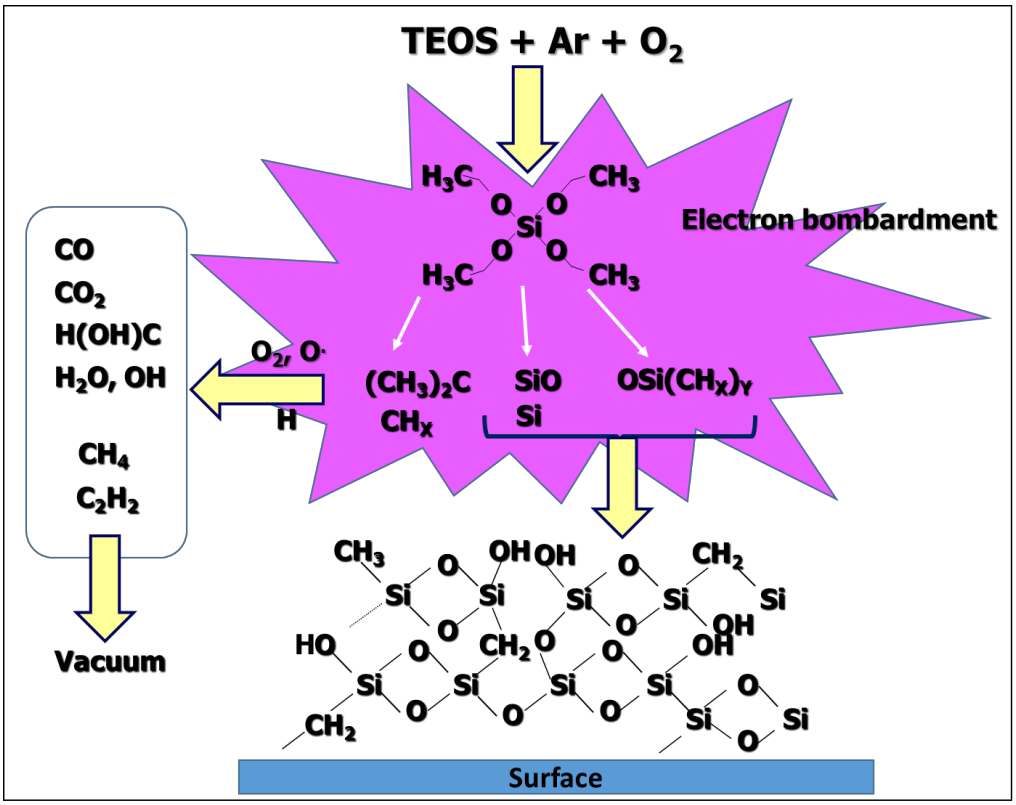

Figure 50: Schematic reactions that occur during PECVD processes for the deposition of SiO_x.

The radio-frequency power plays an important role on the deposited film properties, because higher power lead to a better TEOS disintegration forming less organic Si-composed molecules. Therefore, the organic fraction inside the SiO_x lattice is lower with respect to a film obtained at lower RF-power, obtaining a diamond-like film having higher corrosion properties. Furthermore, during the reactive deposition a sputtering effect on the Cu target is obtained, leading to the dispersion of Cu nanoparticles inside the SiO_x film. The results is a nanostructured thin film composed by Cu nanoparticles embedded in a SiO_x matrix.

In this dissertation, two coatings were studied at different RF-power and deposition time, as exposed in Table 20.

Table 20: Deposition parameters employed for PECVD processes to obtain SiO_x thin films.

Sample	RF-power (W)	Time (min)	Ar (sccm)	O_2 (sccm)	TEOS (sccm)
1	200	20	80	20	1
2	100	30	80	20	1

The obtained films were characterized in term of microstructure, by means of FESEM analyses (the same apparatus described previously), and chemistry, by means of Fourier transform infrared (FTIR) spectroscopy in attenuated total reflectance (ATR) mode and are performed by a Nicolet iS 50 spectrometer. The data are exposed in transmission mode.

3.2.2. Electrochemical impedance Spectroscopy measurements

This technique is widely exploited for the assessing of the corrosion protection provides by protective coating. The approach is based on measuring the frequency response of the working electrode to a small amplitude sinusoidal potential perturbation. The current response results in a sinusoidal signal with same frequency but characterized by different phase and magnitude compared to the perturbation, as showed in Figure 51.
The responses are generally represented in literature by two different plots:

- Nyquist plot - characterized by a real (Z_{re}) and an imaginary (Z_{im}) component.
- Bode plot – the module and the phase shift of the impedance in function of the frequencies are reported.

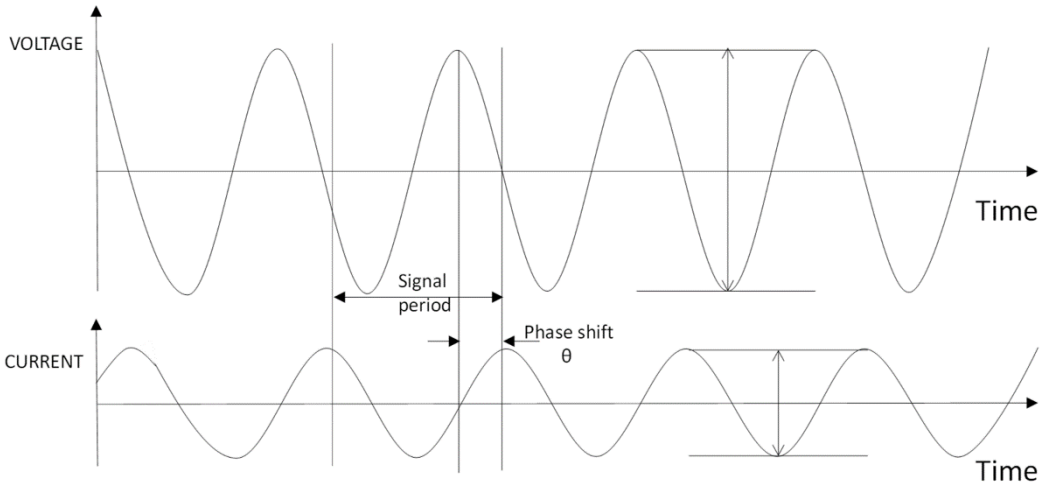

Figure 51: Representation of the current and voltage in function of time [84].

Given the small perturbation applied, EIS measurements are not considered as destructive techniques, for this reason multiple scans are generally performed over time on the same sample, obtaining a real-time monitoring.

From the obtained data, converting the frequencies response to corrosion properties is required by means of equivalent circuits that can describe the surface reactions between the electrolyte and the working electrode. The circuit can be either in series or in parallel and it is formed by resistors (R), capacitor (C), constant phase element (CPE), inductors (L) and Warburg impedance (W). The equivalent

circuit must be chosen according to the specific reactions that occur in order to describe in best way the entire system. Some examples of equivalent circuit are exposed in Figure 52.

The simplest case deals with an impedance characterized by a single capacitive loop (in Nyquist plot). The equivalent circuit can be represented by a capacitor and a resistance in Figure 52-a. A particular case arises when non-uniform corrosion processes occurs onto the surface, a CPE capacitor is required in order to better describe the inhomogeneity current flow distribution (Figure 52-b). The impedance of a constant phase element is represented by:

$$Z = \frac{1}{(j2\pi fC)^n} \qquad \text{eq. 41}$$

where n is a coefficient ranging between 0 and 1; this element is a generalization of a classic capacitor, which becomes a specialized case of a CPE, when n = 1.

In some cases, a straight line with a slope of 45° is observed at low frequencies. This phenome is related to a complex corrosion mechanism, which is no longer only controlled by a charge transfer process, but also by the presence of diffusion of charged species from the corrosion species. In this case, the circuit is characterized by the presence of a Warburg diffusional impedance element (Figure 52-c) described as follow:

$$Z = \frac{A_W}{\sqrt{\omega}} + \frac{A_W}{j\sqrt{\omega}} \qquad \text{eq. 42}$$

Where A_w is the Warburg coefficient, j is the imaginary unit and ω is the angular frequency.

When a second time constant appears, two capacitive loops are exhibited and the circuit needs to be more complex with other two capacitor and resistance elements in parallel.

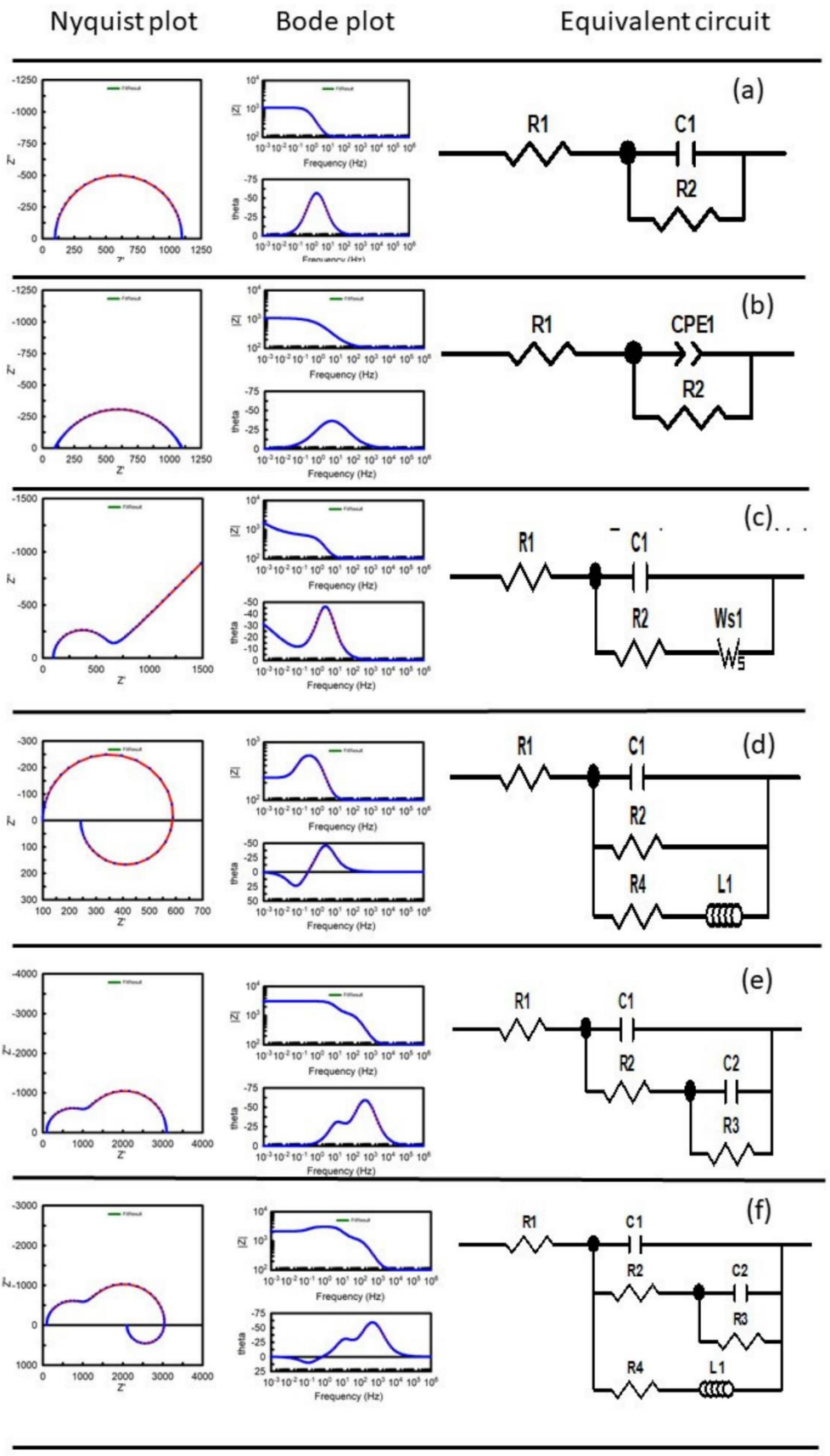

Figure 52: Typical equivalent circuits and relative Nyquist and Bode plots shapes [84].

EIS measurements were carried out by using a cosutumized 3 electrodes cell made by blow glass, suitable to clamp the sample on the bottom (Figure 53) by means of a rubber O-ring having an inner diameter of 10 ± 1 mm, which corresponds to an equivalent surface of about 3.14 cm^2. Such cell was filled with about 0.2 l of Hank's balanced salt solution, in order to simulate a biologic environment. The counter electrode was a platinum wire, while the reference was a Ag/AgCl electrode. The measurements were controlled by a commercial potentiostat (IviumStat) appling a stimulating voltage of 0.01 V in a frequency range from 0.01 Hz to 100 kHz. First measurement was obtained after 6 h of immersion then every 24 h for 5 days. After every measurement, 1 ml of solution was collected from the cell in order to assess the Cu concentration over time and to compare it with the EIS results. The Cu ion concentrations were obtained by means of Inductively Coupled Plasma (ICP) coupled with a mass spectroscopy sensor. This analisis is extremely sensitive since it can reveal concentration in part-per-billion level making it perfectly suitable for the required measurement.

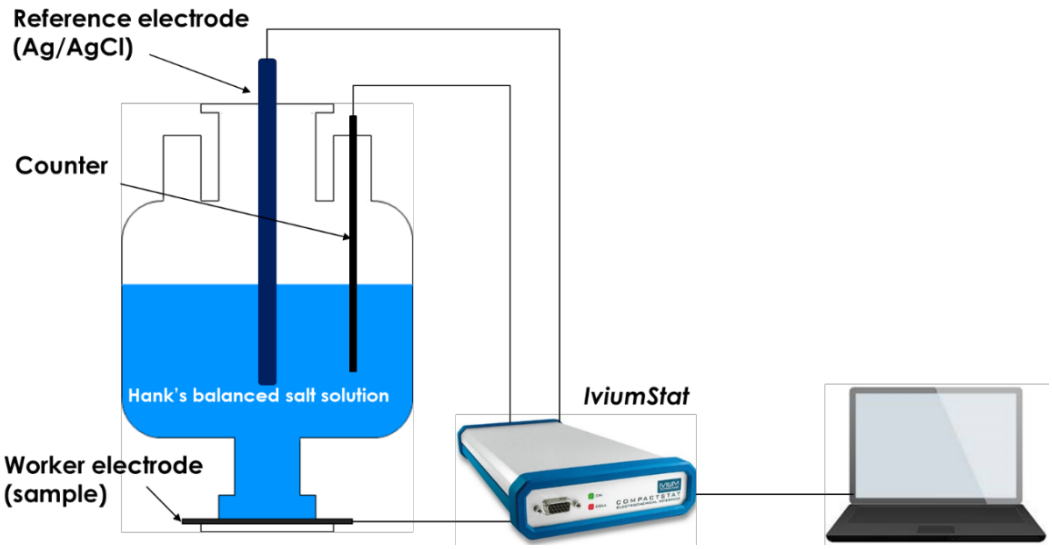

Figure 53: Schematic EIS measurement setup.

3.3. Results and discussion

3.3.1. Films characterization

SEM images related to the superficial microstructure and thickness of the samples are showed in Figure 54. In particular, Figure 54-A shows the Cu layer microstructure, which is characterized by grains with dimension lower than 1 µm. Such layer shows also the higher thickness of 1.3 µm after the second deposition. Regarding the SiO_x films, they exhibit a finer microstructure (Figure 54-B and Figure 54-C), formed by circular shape grains having diameters that not exceed 200 nm, which are suitable for a good coverage of the Cu layer. In fact, it is possible to observe from the cross section images (Figure 54-E and Figure **54**-F) a good

adhesion by the two layers. Always in figures Figure 54-E and Figure **54**-F, an important difference between the two SiO_x layers can be observed, actually a noticeable thickness difference is measured. In fact, despite the longer deposition time for the samples obtained at 100 W, the film shows a thickness of about 30 μm, lower than 3 times with respect to the one obtained at 200 W for 20 minutes, which shows a thickness of about 100 μm. Such results define the importance of the RF-power as more influent parameter for the film thickness growth with respect to the deposition time.

Anyway, the SiO_x thickness achieved by sample 1 remains drastically lower with respect to the copper one, despite both of them are obtained with the same deposition parameters (200 W for 20 minutes). The reason behind this large difference is due to the used deposition techniques. In fact, for the Cu layer the magnetron sputtering deposition was involved, allowing a higher deposition kinetics, then to a higher quantity of deposited material. Regarding the reactive plasma deposition, it is limited by the monomer presence inside the chamber. For these depositions the TEOS flows was set at 1 sccm, does not allowing to reach high film thickness, anyway obtaining a nanostructured layer.

Furthermore, the layers chemistry was assessed by means of infrared analysis and the results are showed in Figure 55. Such curves compare the different behaviour among samples obtained at difference RF-powers. In particular, they highlight the evolution of the infrared spectra of 4 different SiO_x obtained at deposition powers, from 50 W to 300 W. Observing the spectra, it is clear that the inorganic fraction, correlated to the SiO_2 lattice has the more intense peak (red arrow) meaning that the lattice is mainly formed by Si-O bridges, typical for the SiO_2 system. Regarding the organic fraction, it is characterized by the bending and stretching peaks related to $Si(CH_3)_x$ groups (highlighted by the black arrows). Such fraction is less intense than the inorganic one and it decreases increasing the RF-power until almost disappears at 200 W. The same behaviour can be observed for the oxydril groups peak. Actually, such peak can be observed only for low power depositions (until 100 W). As explained before (section 3.2.1.), the RF-power has an important role on the SiO_x chemistry since by higher power it is possible to obtain a better bombardment effect on the monomer, resulting in a more compact layer with a marked diamond-like behaviour.

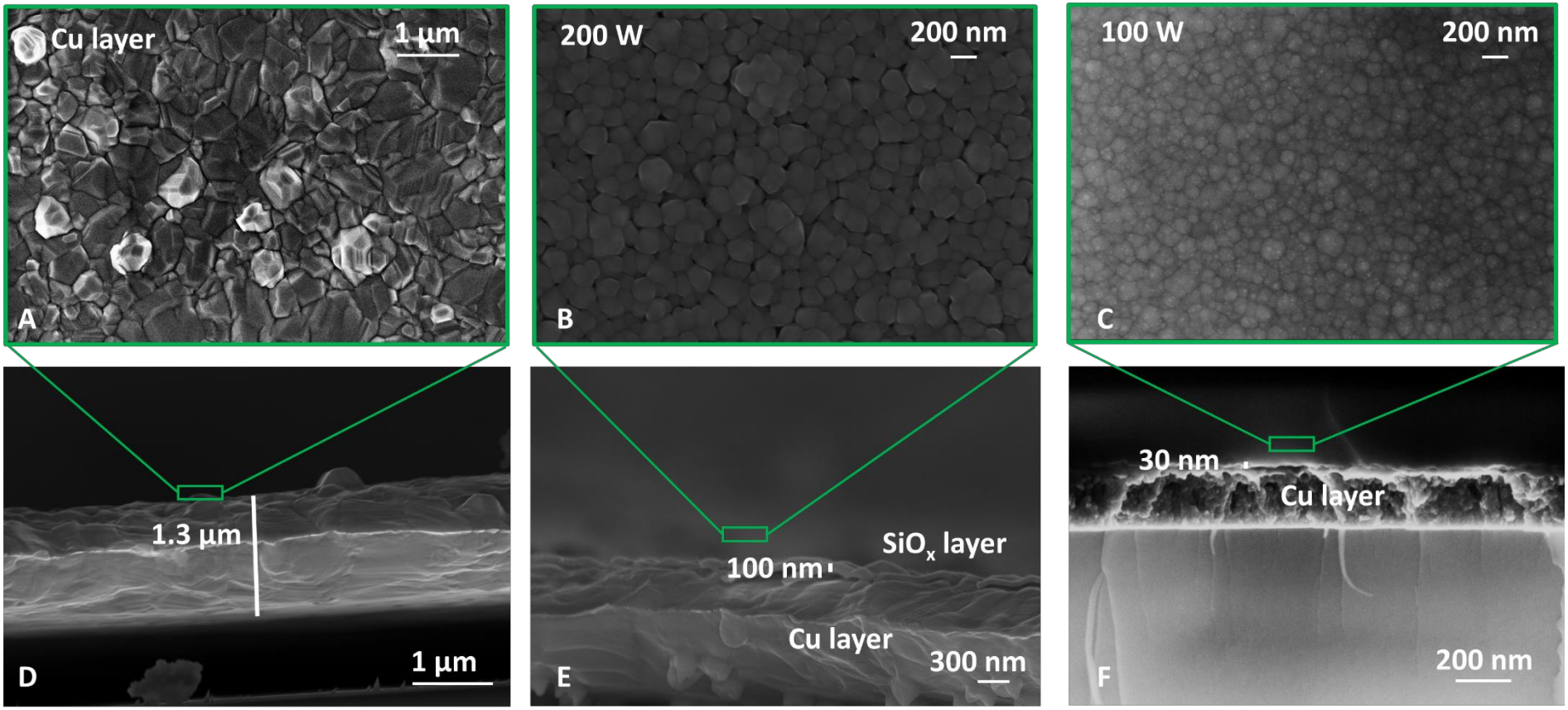

Figure 54: Cross-sections and morphologies for bare Cu layer (A and D), SiO_x obtained at 200 W (B and E) and SiO_x obtained at 100 W (C and F)

On the contrary, at lower RF-powers the organic fraction is more marked making the coating less protective in organic environment because of the high compatibility among these groups and biological environments. Moreover, the oxydril groups play an important role on the coating chemistry; in fact, they improve the coating hydrophilic behaviour making it more affine to the aqueous electrolyte.

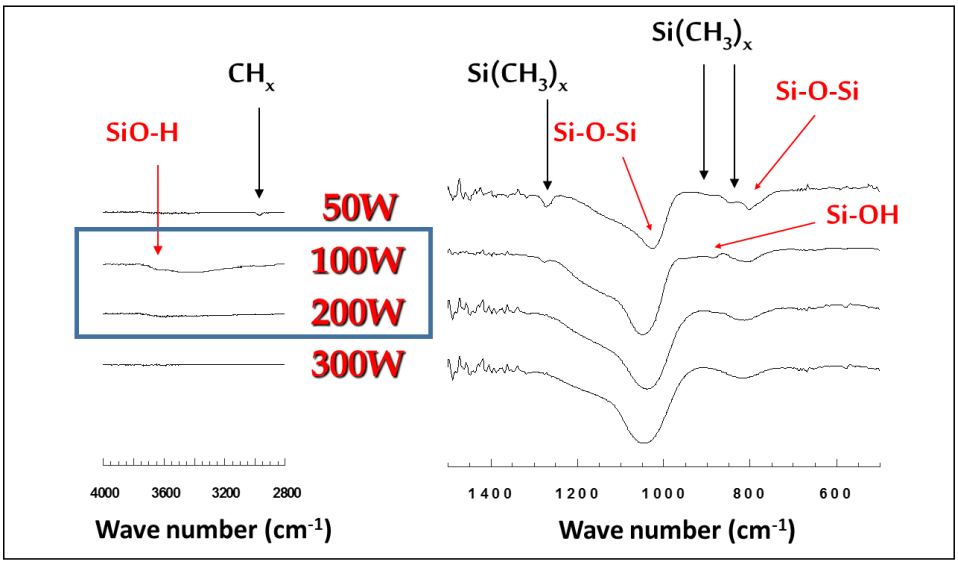

Figure 55: ATR spectra of SiO_x obtained at different RF-powers

3.3.2. Anti-fungi and anti-bacteria properties – correlation between EIS results and Cu ion concentration

The main peculiarities of the obtained coating can be summarized as follow:

- A protective effect from corrosion of the eventual metallic substrate,
- A controlled Cu^{2+} release in order to prevent bacteria and fungi infection.

In fact, such coatings are proposede as proctetive layers for biomedical devices and for bioreassorbable implants. Especially for the latter, they are adressed to have a high corrosion protection in the early stage of use, then gradually degradate in order to release a controlled and continuos amount of Cu^{2+} ion toward the enviroments obtaining the anti-bacteria effect.

The SiO_x layers are characterized by a DC resistivity highly depended on the composition ranging from $\rho = 10^{13}$ Ωm for an SiO_2 layer to about $\rho = 10^{2}$ Ωm for an oxygen free layer [85]. The resistance of a film can be calculated taking in consideration its thickness and the considerated surface, according to eq. 21. Taking as exaple sample 1, the thickness l is about100 nm and the surface s is 3.14 cm^2. Therefore, the expected coating DC resistance lie in the range from 0.1 Ω to 10 GΩ and its measurement can be a interesting method to asses the quality of the produced coating.

The SiO_2 is characterized by an electrical rigidity of about 10^7 V/m, for this reason in this case study, where the film thickness is about 100 nm, it is necessary to apply a voltage less than 1V for a SiO_2 layer and much less in the case of an SiO_x layer, making the impedance measurement not easy to perform. However, appling a time variable voltage it is possible to overcome such problem obtaining further information even on the layer defectivities from the impedance phase results.

For all these reasons, EIS measurements are an important tool to assess the effective corrosion protection of surface coatings. It allows to obtain information about the effective protection granted by the coating and the possible presence of defects. Furthermore, it provides information about the properties evolution over time therefore it is possible monitoring the coating degradation.

The EIS results over 5 days are exposed in Figure 56 and show the bode diagrams, related to the Impedence magnitude and phase. To extrapolate informations about the coating resistance from the magnitude, it is necessary to focus on the results at low frequencies, in particular at 10^{-2} Hz. Actually, at higher frequencies the resistance is correlated to the electrolyte one. The sample obtrained at 100 W shows higher magnitude at 10^{-2} Hz in the early stage of immersion, of about 233.1 $k\Omega.cm^2$. Such results are almost costant for the first 3 days, reaching 200.9 $k\Omega.cm^2$ after 48 h of immersion. After this point the resistance decrease more rapidly until reach 101.7 $k\Omega.cm^2$ after 96 h. Regarding the sample obtained at 200 W the situation is quite different; actually in the early stage of immersion the magnitude at 10^{-2} Hz is about 24.8 $k\Omega.cm^2$ then decrease rapidly to 11.3 $k\Omega.cm^2$ after 24 h and 6.6 $k\Omega.cm^2$ after 5 days. It is worthy to note that sample 1, obtained at 200 W, reach a magnitude one order lower with respect to sample 2. It is a controversery result since it would expected a better behavior for samples obtained at higher RF-frequencies, in relation to their diamond-like properties. An explenation can be given by the FESEM images collected at the end of the EIS measurements exposed in Figure 58-B and Figure **58**-D. A coating obtained at higher RF-power results more compact and stiffer, therefore more fragile. For this reason, it is easy cracking the film during the preparation of the test, due to its rigidity and its lower conformability to the underneath Cu layer rough surface. In fact, as showed in Figure 58-B, the SiO_x layer results completely cracked, exposing the Cu layer to the electrolite. Actually, sample 2 shows better adhesion to the Cu layer impling better magnitude results thanks to its organic fraction wich lead to the formation of a less rigid layer. Such behavior can be also observed in Figure 58-D. After the exposition of the samples to the electrolites several cracks appeared but in different way with respect to sample 1. As a a matter of fact, the two layers (Cu and SiO_x) are intimately overlaped resulting in a laceration effect. In this way, the substrate and only a few portion of Cu layer is exposed to the electrolite granted higher EIS magnitude.

Regarding Bode diagram. It is also important investigate the phase plots for both the investigated samples. Starting form sample 1 in Figure 56, a costant phase plateu is recorded in the mid-low frequencies range of the order of 30° - 40°. This result suggest that the diamond-like SiO_x layer can be considered reasonably

compact. Regarding the sample 2, obtained at 100 W, the phase for low frequencies shows results in the range of 20°, meaning that the film is characterized by higher presences of porosities making them more resistive. Nevertheless, the high conformability achieved by the SiO_x layer obtained at 100 W, with respect to the underneath Cu layer, guarantees better results in term of protection and durability despite its more resistive behaviour.

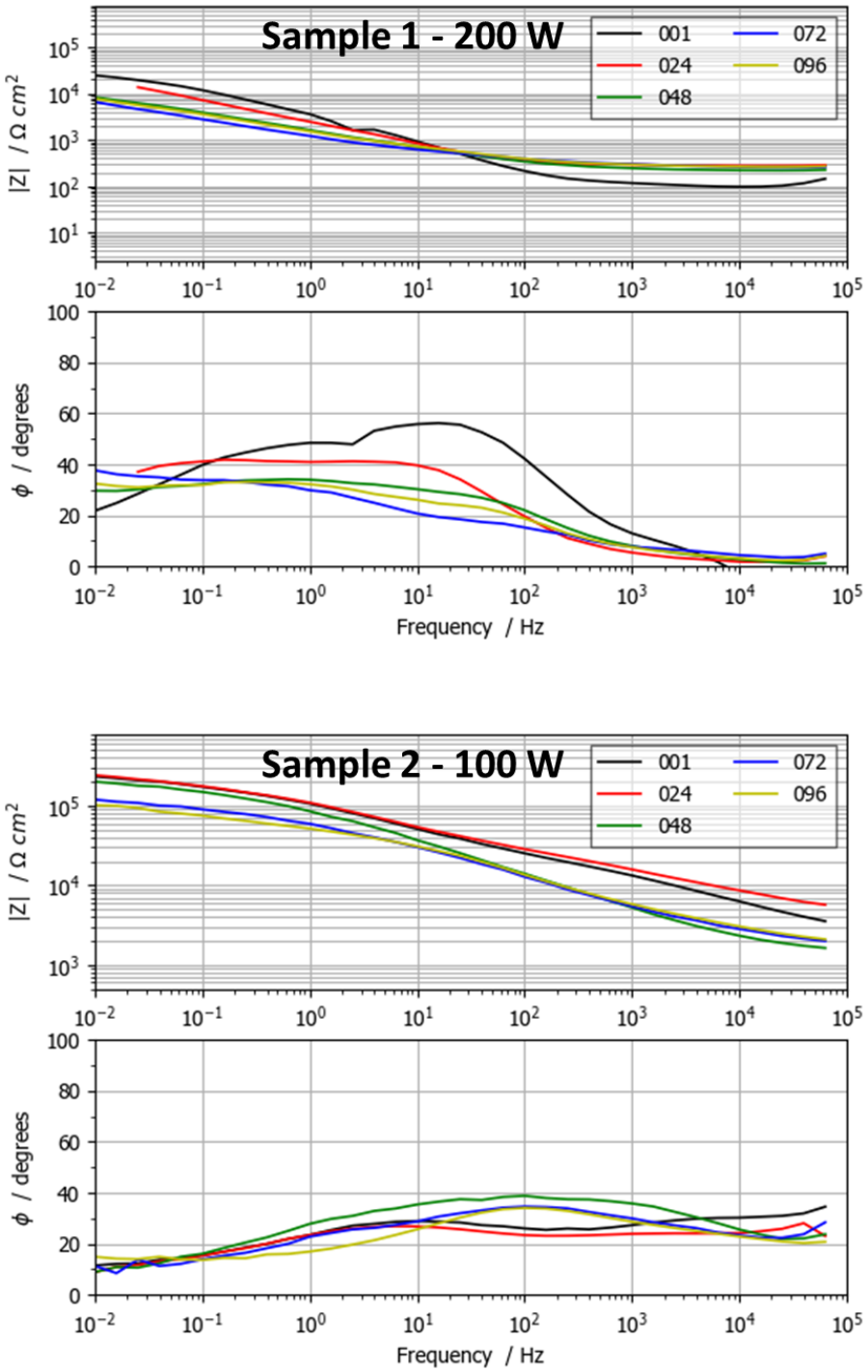

Figure 56: Bode plots representation of the EIS measurements carried out on samples 1 and 2 for 96 h

The proposed circuit for describing the samples EIS behaviour is exposed in Figure 57-E. The proposed circuit is formed by two branches. The first one is formed by a constant phase element CPE_1 and by a resistance R_2, related to the bi-layer impedance, while the second one formed by CPE_2 and R_3 is related for the double time constant behaviour showed by both samples. Completes the circuit R_1 accounts the solution resistance.

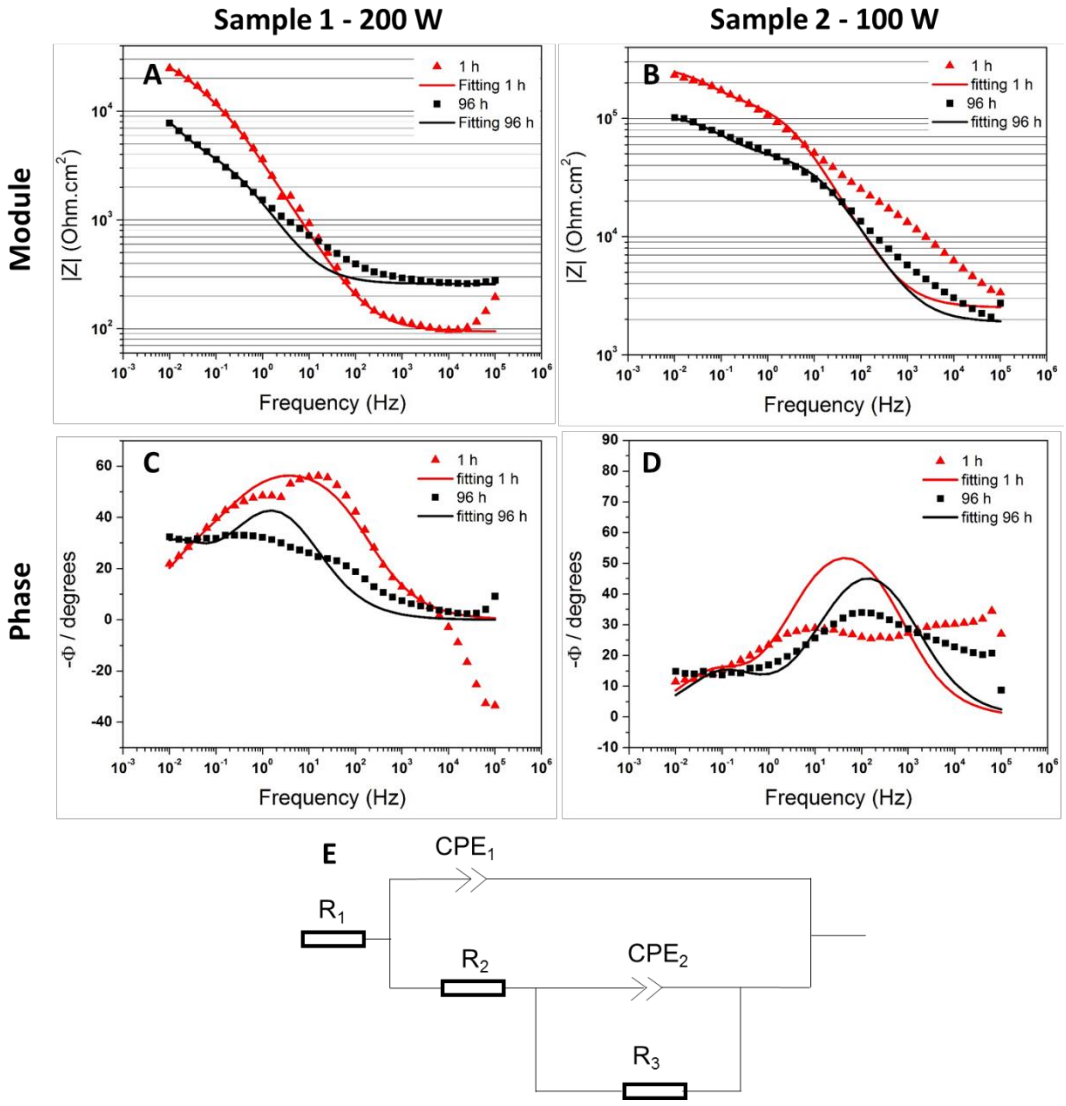

Figure 57: module and phase plots and relative fittings for samples 1 (A and C) and 2 (B and D) after 1 h and 96 h. Proposed equivalent circuit for describing the films behaviour (E)

The proposed circuit was used to fit the EIS plot obtained after 1 h and 96 h of immersion for both sample 1 and 2 and the results are showed in Figure 57, while the extrapolated values are listed in Table 21. Even if a not perfect overlapping is detected, especially for sample 2, the circuit provides a good approximation with respect to the measured data. A reason behind such not perfect overlapping can be explained by the double layer high complexity, which is not completely described by a two constant circuit but it needs a more complex one. Anyway, for the research

goal, the proposed circuit describes in good way the obtained data. The effective film resistance can be obtained by summing the two-resistance contributions, obtaining the polarization resistance (R_p).

Such values are comparable to the measured impedance magnitude at 10^{-2} Hz, in fact, for sample 1 it starts (after 1 h of immersion) at 33902.6 Ω.cm^2 reaching, after 96 h 18020.5 Ω.cm^2, while for sample 2 R_p starts from 273 kΩ.cm^2 to reach 108 kΩ.cm^2.

Table 21: Data extrapolated from the equivalent circuit for both sample 1 and sample 2

	Sample 1 – 200 W		**Sample 2 – 100 W**	
	1 h	**96 h**	**1 h**	**96 h**
R_1 (Ω·cm^2)	94.2	257.48	2512	1884
R_2 (Ω·cm^2)	13395.24	13511.42	130372.8	59251.8
R_3 (Ω·cm^2)	20507.34	4509.04	142273.4	48984
Q_1 (µF·cm^{-2})	64.93631	184.2357	0.941401	0.941401
N_1	0.7	0.71	0.72	7.00E-01
Q_2 (µF·cm^{-2})	300.9236	1121.656	22.20064	34.49045
n_2	0.75	0.75	0.73	7.00E-01
R_p (Ω·cm^2)	33902.6	18020.5	272646.2	108235.8

The anti-fungi and antibacterial effects are provided by the Cu nanoparticles and ions release by the obtained double layer. In this work, such effects were assessed by the conjunction of the EIS measurements with the Cu released analysis obtained by ICP. The results are showed in Figure 58-A and Figure **58**-C.

By a first approach, it is worthy to be noted that there is effectively a similar trend between the EIS module at 10^{-2} and the Cu ions release value over time for both the samples. In particular, at higher module a lower Cu ions value are assigned then, decreasing the module over time, a constant release of Cu is observed. This means that in the early stage of immersion, the SiO_x provides a sufficient stability for releasing low Cu concentration and protecting the underneath substrate. Over time, the protective effect decreases, as observed by the measured module, and consequently an important Cu release is assessed.

Such behaviour is important for those applications where a tailored degradation is needed, in particular for bio-reabsorbable implants (e.g. implants made in Mg) where a controlled degradation is studied [86]. In this particular case, the controlled

Cu release can also prevent the eventual fungi and bacteria proliferation, which would arise during invasive surgery and general operations [87].

From a more detailed point of view, it is clear that the two samples achieved two different behaviours. As explained before, sample 1 achieved a more diamond-like property, due to the higher RF-power used during the deposition. However, the EIS results show worst results with respect to sample 2 obtained at lower RF-power. This was explained by the higher fragility achieved by sample 1, which lead to the formation of premature cracks onto the film surface. For this reason, after 1 h the released Cu is about 22 ppm then it increases sharply until reaches the maximum value of 75 ppb after 96 h. The SiO_x film diamond-like nature has less propensity to degrade; therefore the measured Cu ions are released by the first Cu layer that is exposed after the SiO_x cracking.

A different situation is observed for sample 2. In fact the low RF-power lead to the formation of a more organic coating with better conformability to the Cu under layer. After 1 h, the released Cu is about 17.5 ppb and it is quite stable for the first 3 days, then it increases sharply. In this case, the coating has better corrosion properties toward the under layer and the constant released Cu is from the nanoparticles embedded to the surface layer. After 3 days, the EIS modulus decreases, meaning that the layer is breaking down and subsequently the released Cu concentration increases until reach the value of 32 ppb after 96 h. Such result is lower than half with respect to the one obtained for sample 1 after 96 h, confirming a better controlled release of the Cu nanoparticles. In fact, in this case the concentration of Cu ions released by the Cu layer is lower since the coating achieve a better stability e conformability on it.

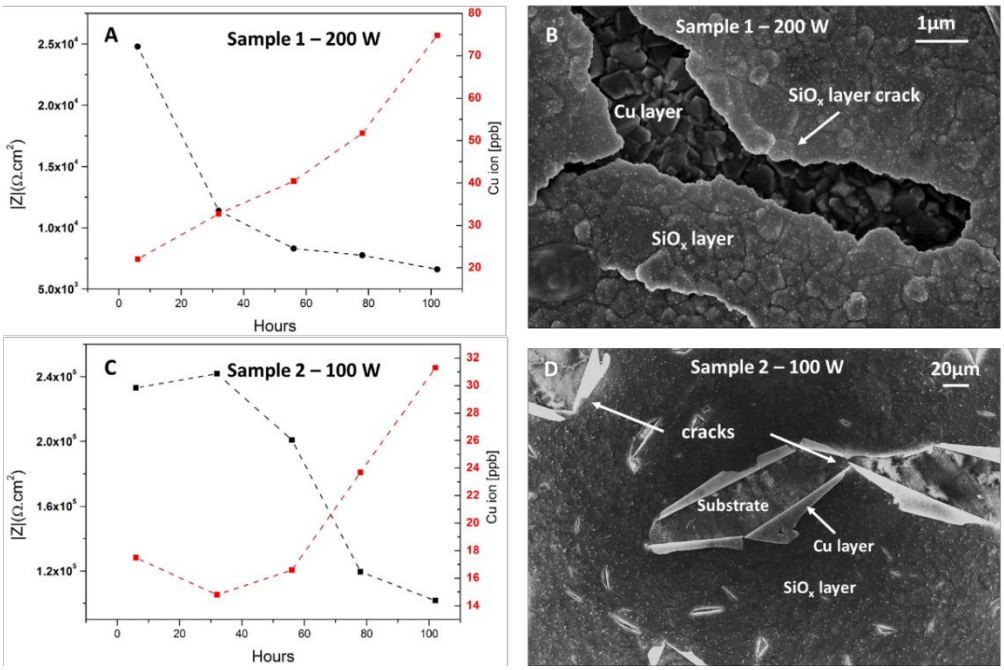

Figure 58: Correlation between EIS modulus at 10^{-2} Hz and Cu ions released over time (A and C) and the film surface morphologies after 96 h of exposition in Hank's balanced salt solution (B and D).

3.4. Conclusion and future works

The results presented so far in this dissertation show an interesting method to develop and assess bioactive coatings for biomedical applications, in particular for the prevention of fungi and bacteria outbreaks involving two different measurement techniques.

The project is still under develop and the showed data represent a proof of concept with interesting results. In particular, the behaviour of two different protective films is exposed and the correlation between two different measurements is confirmed.

EIS measurements are a well-established method to assess the effective protection effect achieved by protective coating and in this work. Actually it was possible to compare such measurement with the Cu released by the protective film over time. In fact, a close correlation has been observed between the impedance module at low frequencies and the effective Cu ions concentration for both the investigated samples.

Furthermore, it has been possible to evaluate the efficiency in term of protection and Cu release in function of the applied RF – power during the deposition process. From such preliminary results, a low RF - power allows to achieve a more organic and hydrophilic film, characterized by a higher conformability with respect to the underneath substrate. On the contrary, a higher RF – power generates a diamond like coating but more fragile and this leads to a premature cracking of the coating itself.

In conclusion lower RF – powers are suggested to obtain a SiO_x coating with a tailored degradation and the combination of EIS measurements and Cu ions concertation measurements is a perfect method to evaluate the gradual protection and the anti-bacteria effects of such films.

The results so far are promising but not enough for real applications, in fact, the corrosion protection should be improved in order to achieve better results in a longer exposure time (at least one week before starting to degrade). Moreover, in order to achieve a higher and more controlled Cu release, a multilayer formed by 3 layers is ongoing. In this case, the coating will be formed by a $SiO_x/Cu/SiO_x$ sandwich structure. The first layer will need to protect from the corrosion the substrate, for such reason it will be more compact and resistant before degrading gradually. The second layer, composed by Cu will act as antibacterial and antifungal barrier and then the second SiO_x layer, the last one, will degrade more rapidly with respect the first one. In this way, it is possible to control the Cu release by modulating the second SiO_x layer nature by means of the deposition power. The double layer and the sandwich layer, actually, are studied for medical devices and packaging, which are applications where the possibility to get in contact with bacteria is higher[88].

Last part of this project will effort a real case study, applying such coating onto a magnesium sample (in order to simulate an implant). Even this case will be monitored by the already established EIS – ICP measurements method described in

this chapter. For such purpose, only the SiO_x is required, since a second Cu layer can lead to an excess of Cu ions accumulations inside the human body causing disease.

Chapter 4

Effect of CO_2 on the corrosion of magnesium alloy WE43 in minimum essential medium

This chapter faces the effect of a controlled CO_2 atmosphere on the corrosion of WE43 magnesium alloy in a minimum essential medium (MEM) for biomedical applications. A considerable amount of works is present in literature regarding the assessment of magnesium bio corrosion for implants purposes, but a non-defined methodology agreement among the experiments set-up leads to a non-confrontable results. This work highlights the importance to carry out *in-vitro* experiment in presence of 5 vol. % of CO_2 in order to simulate in the best way the buffering system of the human body. Such aspect covers an important role for obtaining realistic results for both long-term experiments (immersion test), as well as short-term experiments (polarization), therefore having useful information for the prediction of an eventual corrosion behaviour *in-vivo.*

In literature is already known the importance of a buffered system to simulate human body fluids but to the best of the author knowledge, specific study on the role of CO_2 and relative carbonates have been assessed only in inorganic environments.

4.1 Introduction

Magnesium and its alloys have raised the researcher's interest in the last years thanks to their unique properties. First of all, magnesium is the lightest engineering metal with a density of about 1.7 g/cm^3, which combined with its low Young modulus (about 45 GPa), makes it a suitable material for implant application [89]–[92]. Actually, human bone tissues have a density of 0.74 g/cm^3 and a Young modulus of about 10-15 GPa, such similar values are a crucial factor for avoiding eventually stress shielding caused by implants made by material with higher modulus values than the bones one [93]. But the real outstanding properties which characterize Mg are its biocompatibility and bioresorbable capabilities [94], [95], which can make possible the realization of temporary implants (e.g. stents [96], [97] or orthopaedic implants [98] avoiding, further stress and pain for the patients, since they do not need to be removed by means of a second surgery. Furthermore, the Mg ions released inside the body during the implant bioreabsorbtion, not only are not

the cause of local metallosis intoxication, like the others metallic ions, but also they can promote the formation of new bone tissues, reducing the healing time [89], [99], [100]. In fact, Mg is an essential element for the human metabolism, being the fourth most abundant cation in the human body, and more than half of its presence is stored inside the bone tissues. Additionally, it is involved in several biological pathways, as cofactor of different enzymes required e.g. for the DNA synthesis and repair, and its role in preventing oxygen stress and regulating processes as cell cycle and apoptosis is well reported [101]. Despite the over-accumulation of Mg cations can be dangerous for the human health, such condition is rare since the Mg^{2+} in excess are easily filtered and eliminated by urines [99], [102].

Unfortunately, Mg has an important drawback, which limits its application in several fields: low corrosion properties, in particular in aqueous environments.

Generally, Magnesium alloys are characterized by low thermodynamic stability (E° about -2.4V vs SHE), which lead to a readily oxidation in aqueous environment, thus the formation of a compact $Mg(OH)_2$ layer. The overall reaction is described herein:

$Mg\ (s) \rightarrow Mg^{2+} + 2e^-$ (Anodic reaction) eq. 43

$H_2O\ (l) + 2e^- \rightarrow H_2 + OH^-$ (Cathodic reaction) eq. 44

$Mg^{2+} + OH \rightarrow Mg(OH)_2\ (s)$ (Corrosion Products reaction) eq. 45

$Mg\ (s) + H_2O\ (l) \rightarrow Mg(OH)_2\ (s) + H_2\ (g)$ (Overall reaction) eq. 46

Such superficial $Mg(OH)_2$ layer is stable and can provide a good corrosion protection, but only in alkaline environments and in absence of aggressive anions. Actually, body fluids are rich of Cl ions that can break the superficial oxide layer forming $MgCl_2$ without any protective properties. Although the main concept for a bioreasorbable implant is a complete dissolution, several concerns are related to a fast implant degradation. As a matter of fact, a temporary implant must provide a suitable structural integrity and guarantee a correct functionality until the damaged tissue have reached a sufficient healing. That is not possible whether the aggressive environment lead to a fast corrosion reducing the implant mechanical properties then causing a premature failure.

Another concern related to biomedical applications is that the corrosion of magnesium is always coupled with a high generation of H_2 gas, due to the cathodic decomposition of the water, as described in eq. 44. Such gas generation is negligible for sufficient slow rate production, since it can be efficiently removed from the organism, avoiding a large accumulation of H_2 in a single site. Otherwise, a high corrosion rate can cause a massive gas production that can be accumulate forming local bulge leading embolus, and generally tissue damages [89], [92], [100].

In addition, the magnesium corrosion releases, according to eq. 44, OH^- anion, which lead to a alkalization of the electrolyte, if this one is non-buffered, till reach high values of pH (about 11-12). A buffered solution, otherwise, can stabilize the pH of the solution to a determinate value (same situation for the body fluids) but in proximity of the magnesium surface a modest pH increasing can be detected. As

said before an alkaline environment can guarantee higher corrosion protection then decrease the magnesium dissolution rate, but in biological application it can generate a harmful situation for the surrounded tissue.

The first clinical report regarding the employment of magnesium for biomedical applications, as orthopaedic implants, was given in 1907, where a pure magnesium plate was used to fix a bones fracture. Unfortunately, the attempt failed because the implant corroded too fast causing a structural failure after 8 days from the surgery, and an elevated amount of H_2 was detected in the surrounded tissues. In the following years, few others attempts were carried out using pure magnesium but its poor corrosion properties caused a loss of interest on such material. The situation changed in the last 15 years, where a renewed interest on magnesium for bio-implants grew up and several efforts have been carried out in order to investigate the corrosion mechanism of such material *in-vitro* and how to decrease its corrosion rate the in biological environment. Generally, the magnesium corrosion assessment for biomedical application is still challenging since it is not easy to simulate a biological environment, reproducing the complex reactions that occur *in-vivo*. Actually, the human body fluids are characterized by several compounds, such as amino acids, proteins, carbonates and several others, and all the system is kept at pH 7.3 by an efficient buffering due to carbonates. For this reason, several precautions are mandatory in order to set-up the experiments in a better way. First of all, it is important to employ an electrolyte with a formulation as close as possible to the human body fluids. In general there is not a clear agreement on which one use, in fact in literature several different simulated body fluids have been employed such as Hank's balanced salt solution [103][104][105][106], Kokubo solution [107], MEM (Minimum essential medium) [106][108][109]. The principal components of such electrolytes are showed in tab. 19. In particular, MEM solution is characterized by the presence of a sufficient amount of carbonates, which allows an accurate pH maintaining during the Mg dissolution. As explained before, during Mg dissolution OH^- ions are released from the decomposition of the water increasing drastically the pH until reaching about 11. Such scenario is absolutely not realistic therefore the solution needs to be buffered. In literature, generally, acid reagents, e.g. cloridric acid (HCl) or 4-(2-hydroxyethyl)-1-piperazineethanesulfonic acid (HEPES), are used as buffers to maintain the physiologic pH, but such substances can lead to a different situation with respect to the human body fluids one. Despite the presence of carbonates, dissolved inside the electrolyte generates both an acidification of the solution and a decrease of solution resistance, which could affect the magnesium corrosion behaviour, the importance of such carbonates has not received the right attention to date. Actually, only few studies in literature face the role of CO_2 and all of them regard the corrosion of magnesium in non-biological environments [110][111][112]. As far of author knowledge, only a work deal the Mg corrosion in MEM electrolyte in open air and in incubator [113] but it is focused more on the formation of the protective layer than the corrosion mechanism achieved by the

presence of CO_2. Furthermore, the experiments in open air were carried out at room temperature while this work deal on the effect of CO_2 in a biological environment.

In this work the effective effect of CO_2 and relative carbonates dissolved inside the electrolyte, is assessed by means of potentiodynamic polarisation, electrochemical impedance spectroscopy (EIS) and immersion test.

4.1.1 Magnesium corrosion mechanisms in aqueous environment

In order to better understand the CO_2 effect on Mg corrosion, it is important focusing on the magnesium corrosion behaviour in aqueous environment. As described before, the immersion of Mg alloys in an aqueous electrolyte leads to the formation of a soluble $Mg(OH)_2$ surface layer, passing through the two cathodic (eq. 44) and anodic (eq. 43) semi-reactions. Such layer does not offer a high corrosion protection since it is soluble in most aqueous environments, especially at low pH and in presence of Cl^- ions, which make the dissolution accelerated.

The corrosion is also degenerated by the presence of noble particles onto magnesium surface, which act as cathodic regions enhancing the water reduction therefore the H_2 evolution. Such particles can be impurities (usually Fe island segregated during the cast process) or second phases. While the Fe impurities are undesired and it is always important reducing their concentration, the second phases are generated by alloying Mg with other elements in order to obtain suitable alloys for specific applications. In fact, pure magnesium shows low mechanical properties, such as ultimate tensile stress (UTS) hardness etc., then for obtain their improvement alloying is required in order to extend the engineering application fields of Mg. While the mechanical properties are always enhanced by the Mg alloying, the corrosion behaviour is often compromised by the generation of cathodic second phases. Generally only few elements and at low concentration are able to create a solid solution with Mg (eg Al and Zn) then avoiding the formation of second phases. As said before. Mg is characterized by a lower thermodynamic stability then the cathodic particles have always-higher potential leading the formation of micro galvanic couples. The result of this assumption is that pure Mg achieve the best corrosion properties with respect to its alloys since these have always a higher presence of second phases.

Hydrogen evolution (HE) is related to the cathodic semi reaction (eq. 44) and it takes place spontaneously in aqueous environments at open circuit potential (OCP) condition. However, regarding to the Mg and its alloys corrosion, it is worthy to mention an anomalous HE effect, which occurs when such metals undergo to anodized polarization, causing higher dissolution rate. Actually, the HE should decrease in exponential way by increasing the Mg polarization potential, according to Butler-Volmer equation (eq. 47).

$$i_{HER} = i_{0,h,mg} \left[\exp\left(\frac{E-E_{rev,H}}{b_a}\right) - \exp\left(-\frac{E-E_{rev,H}}{b_c}\right)\right] \quad \text{eq. 47}$$

where i_{HER} is the current density related to the HER (A/cm^2), $i_{0,H,Mg}$ is associated with the exchange current density for the evolution of H_2 on Mg (A/cm^2), E is the electrode potential (V), $E_{rev,H}$ is the reversible potential for the HER (V), b_a is the value of the anodic Tafel slope and b_c is the absolute value of the cathodic Tafel slope (V/dec).

The effect anomalous HE effect is reported in Figure 59. The calculated current density obtained at different cathodic and anodic points are plotted in function of the measured potential for two different alloys. According to eq. 47 the current density should follow the dash line after reaching the OCP. Actually, an increase is observed in the anodic region.

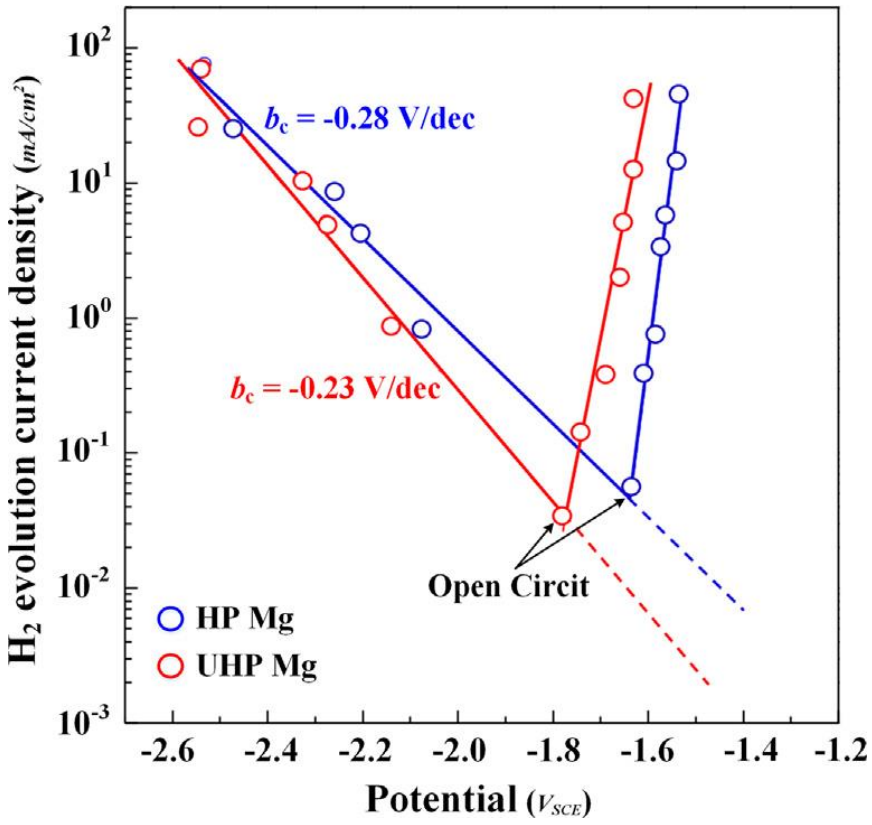

Figure 59: Correlation between current density and relative HE obtained from two different Mg purities [114].

A consequence of this anomalous effect is the invalidation of the Faraday's Law on magnesium cases thus, it is not possible to estimate the magnesium concentration during anodic dissolution by using only electrochemical methods since a portion of electrons released during the polarization do not flow toward the counter electrode but are involved in the generation of hydrogen.

4.1.2. Magnesium corrosion mechanisms in biological environments

In section 4.1.1. a general aspect related to the magnesium corrosion in aqueous environment is exposed., but the situation is more complex in simulated body environment. To assess Mg corrosion for biomedical applications a classic 0.1 M NaCl solution is not enough to obtain a confident and realistic response by the results. For this reason, simulated body fluids are required as electrolytes actually; the human body environment is formed by several different organic and inorganic species like amino acids, Ca^{2+}, PO_4^{3-}, and HCO_3^-. The latter can react with the OH^- generated by the Mg degradation forming a hydroxyapatite precipitation layer onto Mg surface, improving the barrier effect thus reducing the Mg corrosion. In other hand, the human body is characterized by an efficient buffering effect, which keep the pH at the constant value of 7.3 avoiding eventual local alkalinisation, which can inhibit the Mg dissolution. In conclusion, more complex reactions occur taking in account a biological environment and part of them are not already recognized making the data interpretation challenging. A schematic Mg corrosion in biological environment representation is exposed in Figure 60. Moreover, the body temperature of 37 °C affects the Mg corrosion, accelerating its reactions with respect to the room temperature. The high temperature can also influence the precipitation of several type Ca-phosphates. In fact, such precipitates solubility is temperature dependent.

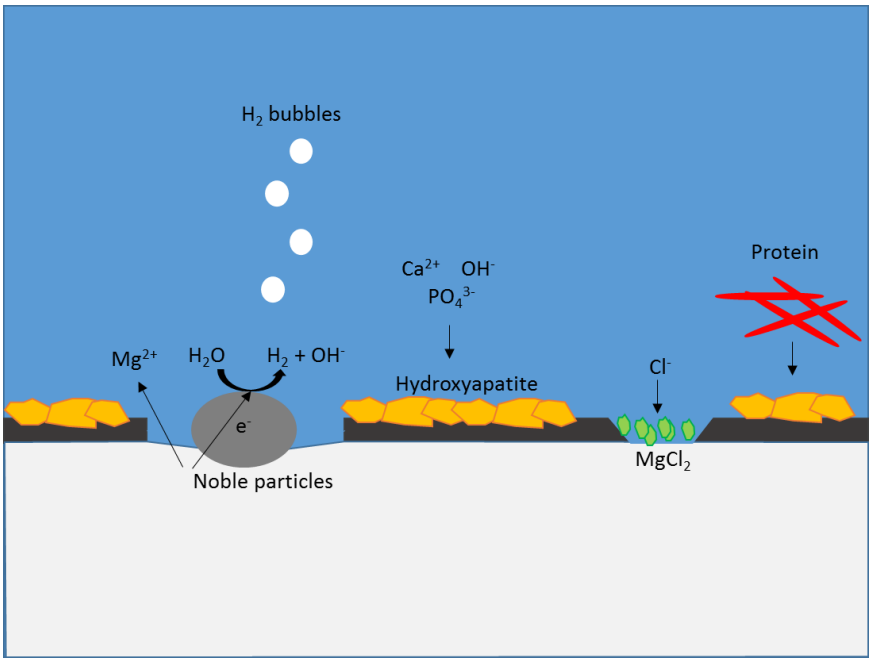

Figure 60: Schematic representation of Mg corrosion in biological environment.

To simulate the body fluids, several different electrolytes are present in literature but, unfortunately, there is not a clear agreement about which one is better

to use. The principal difference among these electrolytes is the formulation and the chosen can be driven by the experimental necessities. Some examples are reported in Table 22. Ringer's solution is a cheap solution that can be easily produced in lab since it is obtained by sodium chloride, potassium chloride, calcium chloride and sodium bicarbonate. Another solution widely used in literature, having a formulation more complex and closer to the human fluids one is Hank's balanced salt solution. Different formulations are commercially available and they can be a passing compromise between the cost and the human fluids simulation. Regarding minimum essential medium (MEM) is so far the formulation closest to the human fluids one. It is characterized by the presence of organic fraction (amino acids) and it is commonly used as substrate for cellular culture adding 10% of fetal bovine serum (FBS). The main drawbacks are the cost (expensive) and the challenging to handle. In fact, being characterized by an organic fraction, it requires an accurate preparation and cleaning in order to avoid infections and fungi proliferation that can lead to undesired results. Actually, both the samples and the equipment that have to be in contact with the MEM need to be disinfected with a solution formed by 70 vol. % ethanol before the use and keep in sterile environment. Furthermore, MEM formulation is characterized by a high presence of carbonates, which allows to control the solution pH over time. However to guarantee such pH autoregulation at about 7.3, a constant CO_2 environment is necessary in order to achieve a CO_2-HCO_3^- buffer system, thus a biological incubator is required to perform analyses involving MEM solution

Table 22: Comparison between the principal components of the human blood with respect to different simulated body fluids.

	Component	Blood plasma	Ringer' solution	HBSS (H1387)	MEM	DMEM GlutaMAX™
Inorganic ions (mM)	**Cl^-**	100-103	164.2	145	124.34	117.46
	HCO_3^-	22-30	2.4	4.2	26.19	44.05
	$H_2PO_4^-$	0.0-0.08	-	0.44	1.01	0.91
	HPO_4^-	0.0-1.0	-	0.34	-	-
	SO_4^-	0.5	-	0.81	0.81	0.81
	Mg^{2+}	1.0-1.5	-	0.81	0.81	0.81
	Ca^{2+}	2.5	2.4	1.26	1.80	1.80
	Na^+	140-142	156.4	1.42	144.44	155.29
	K^+	5	5.6	5.81	5.33	5.33
Organic compounds (g/l)	**Proteins**	35-80	-	-	-	-
	Amino acids	0.25-0.4	-	-	871	1884
	Vitamins	µg–mg	-	-	8.1	31.6
	Glucose	0.9-1.1	-	1	1	4.5

4.2 Measurements techniques for magnesium corrosion assessment

The corrosion assessment of Mg and its alloys pass through several different measurements designed for the estimation of certain corrosion aspects, thus to provide model for predicting and controlling its corrosion. Actually, it is very important being able to determine corrosion parameters (e.g. corrosion rate) and correlating them to the microstructure and composition of the studied system. As already exposed, the Mg and its alloys corrosion involves several complex reactions, making its characterization challenging. Therefore, different techniques are required for a complete assessment and obtaining enough data for a suitable corrosion behaviour modelling.

This chapter deal with the characterization of magnesium corrosion in presence of CO_2 for biomedical applications. These particular cases are assessed by *in-vitro* tests. For this reason, in this section, a special focus will be effort toward the analyses that are common employed for biomedical application and this involves aqueous environment at 37 °C.

The available techniques, for a direct magnesium corrosion assessment, can be grouped in two main categories:

- *Non-electrochemical measurements* - no driving-force is applied during the test (OCP condition).
- *Electrochemical measurement* – a driving force is applied (e.g by potentiostat).

Both of them are generally involved since they provide complementary results. Moreover, additional surface analyses are required for the characterization of the corrosion products generated during the corrosion test. Such post analyses have high importance since can provide information about the reactions that occur between the alloy and the electrolyte, e.g. by the corrosion products composition, and how they are correlated to the alloy microstructure. It is obvious that a suitable storage and handling are required in order to avoid any sort of undesired modification a contamination of the Mg corrosion products. In fact, Mg can also react with the atmospherical humidity undergoing further dissolution and alteration. Therefore, after the corrosion test the storage in controlled atmosphere (e.g dry or in vacuum) is strongly suggested.

Such test are generally non-destructive and can be easily performed. The main important are:

- *SEM analyses* – Surface observation via SEM is a common and easy way to obtain information about the corrosion mechanism. By SEM, it is possible to assess the superficial corrosion morphology as well as the corrosion products one. Furthermore, SEM instruments are generally coupled with EDS equipment, which allows to collect information about the corrosion products composition.

- *Infrared spectroscopy* – the analysis can provide corrosion products compositional information by the interaction of infrared radiation and the corrosion products themselves. In particular, it is useful to estimate the carbonates precipitation during the *in vitro* corrosion test.
- *X-ray diffraction (XRD)* – this analysis allows to obtain information about the phases formed during the corrosion process. This technique is the more difficult to perform since it is generally performed for bulk characterization. For this reason, accurate process parameters are required and the corrosion products layer would be thick enough to be analysed.

4.2.1 Electrochemical measurement techniques

As electrochemical measurement are referred all those techniques, which involves a potentiostat in order to measure and/or apply an electrochemical driving force. The main important are:

- *Potentiodinamic polarization (PDP)*
- *Electrochemical impedance spectroscopy (EIS)*

These are widely involved in Mg corrosion assessment and in literature, it is possible to find several studies related to the corrosion mechanism and the spectral interpretation of the obtained results. Such tests are performed by using a three electrode cell formed by a counter electrode (usually is a platinum wire), a reference electrode (e.g. Ag/AgCl or satured calomel) and the working electrode (the sample).

4.2.1.1. Potentiodinamic polarization tests

. This test is the most common electrochemical technique employed for *in-vitro* corrosion assessment.
Before the test, a certain immersion time, at OCP condition, is required in order to obtain a stable potential on Mg surface. Actually, when a metallic samples is exposed to an electrolytes, it takes a certain amount of time to create the electrical double layer (EDL). Performing the PDP test before the redistribution of the species between the sample surface and the electrolytes can generate an inconsistent result in term of sample kinetic. Given the Mg high reactivity in aqueous environment, usually no more than 10 minutes of OCP are necessary. At this point, the voltage is swept at a controlled rate between pre-set potential values. Usually, the polarization sweep starts from lower potential vs OCP (cathodic branch) and gradually increase to higher potential until reach positive values (anodic branch). The results provide several information about the corrosion kinetic (by the observation of the cathodic and anodic branches) as well as corrosion rate. The latter is possible by means of Tafel extrapolation, which provide information regarding the corrosion potential (E_{corr}) and corrosion current density (i_{corr}) [115]. An important aspect provided by PDP is the possibility to have a quantification of the relative anodic and cathodic

rates in the range of a certain potential. This means that, taken two alloys having same i_{corr}, it is possible to quantify the cathodic reaction by the lower potential branches. This is an important feature for an engineering point of view since it is possible to discriminate the alloy with the worst cathodic behaviour (related to the hydrogen evolution). Actually, by PDP, it is possible to evaluate the contribution of the alloying on the corrosion kinetics. For example in Figure 61, two polarization curves are exposed and both shows a similar i_{corr} value. However, the presence of Zr in alloying can increase the cathodic branch, shifting the curve on the right at higher corrosion density since they promote the cathodic semi reaction, and the E_{corr} can shift at more noble value [90].

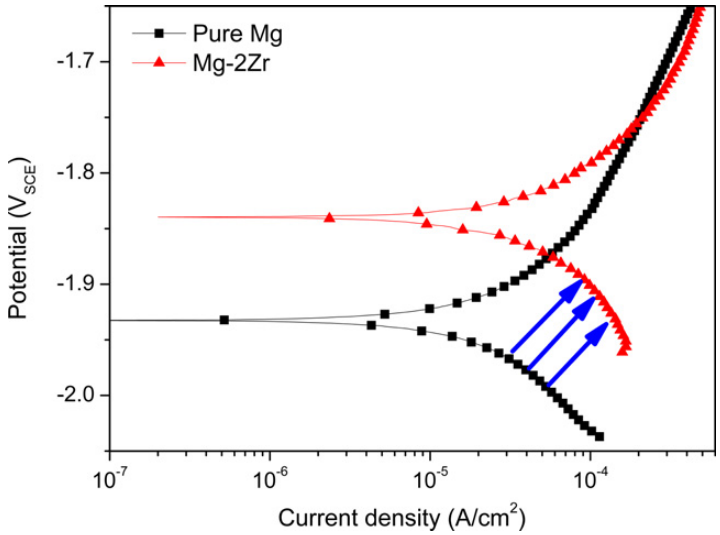

Figure 61: Example of polarisation curves obtained for two different Mg alloys [90].

From PDP curves it is also possible to assess the effect of different electrolyte formulation on corrosion behaviour, for example the effect of a different NaCl concentration or the presence of organic components.

PDP is an instantaneous test that can provide results in little time, a complete scan indeed can be obtained in less than 10 minutes, but it is representative at the time it is performed. In fact, this is a destructive test, which creates high perturbation onto the sample surface, making impossible to perform more than 1 scan every time. This means that the results are related to the early stage of immersion. Nevertheless, such techniques is still effective for the corrosion mechanism assessment and provides useful data for comparing multiple variables.

4.2.1.1. Electrochemical impedance spectroscopy

This technique allows to obtain information regarding the corrosion protection provided by the surface corrosion layer, formed during the corrosion processes. The basis of this measurement has already been described in chapter 3.2.2.

While PDP analyses are considered destructive since the sample surface undergoes high perturbations, EIS measurements involve small perturbations allowing to monitor the sample behaviour in real-time [84].

The principal EIS feature is to provide information regarding the surface layer formed during the corrosion process over time. In particular, in the case of samples immersed in simulated body fluids, the generation of passivating layer by the precipitation of hydroxyapatite and CaP compounds and their contribution on the Mg corrosion protection.

The electrochemical response at the sample surface can be assessed by fitting the data with an equivalent circuit, in order to correlate the frequency response data to corrosion properties such as corrosion resistance and corrosion impedance. In literature several different circuits are proposed [84] and it is not easy to choose the right one, since it is necessary to know exactly the reactions that occur on the sample surface. Moreover, magnesium alloys impedance is often characterized by an inductive behaviour at low frequencies and the relative mechanism still debated.

EIS can also provide information about the polarization resistance (R_p) and the relative corrosion rate by using the Stern-Geary relationship (Tafel coefficient are required) as follow:

$$J_{corr} = \frac{B}{R_p} = \frac{\beta_\alpha \beta_c}{2.303 R_p \ (\beta_\alpha + \beta_c)} \qquad \text{eq. 48}$$

Where β_α and β_c are the anodic and cathodic Tafel coefficients respectively.

4.2.2 Non-electrochemical measurement techniques

Non-electrochemical measurements techniques are generally based on sample immersion inside the electrolyte in order to estimate:

- *Mass loss*
- *Hydrogen evolution*

Generally, the two measurements are carried out at the same time by the well-known inverted funnel set-up [90][114] exhibited in Figure 62. They are relatively easy to set up and no complex and expensive equipment are required. Such test provides information about the alloy corrosion rate but, unlike the electrochemical test, none corrosion mechanisms are highlighted.

Some works highlight the possibility to combine both the electrochemical tests with the unpolarised ones by the realization of a specific connection of the sample to the potentiostat [116][117]. In several works, the pH is also reported in order to provide qualitative results. As already mentioned, it is extremely important for *in-vitro* tests to keep the pH at 7.3 in order to avoid undesired Mg passivation that can affect the measured magnesium corrosion rate.

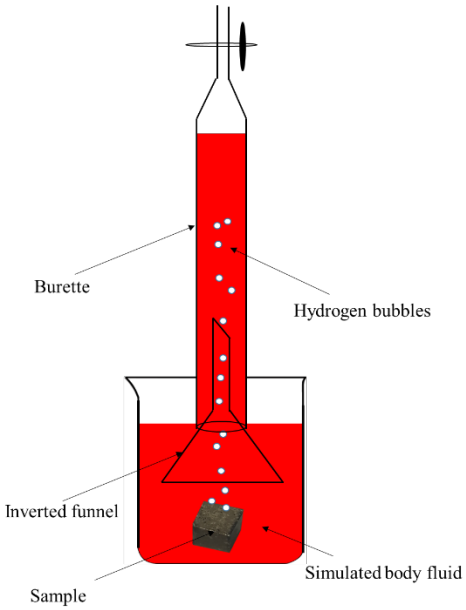

Figure 62: Common set-up employed to assess mass loss and HE at the same time.

4.2.2.1. Mass loss test

This test is the simplest in-vitro method reported in literature for assessing the Mg corrosion rate and consists in the sample immersion in the corrosive electrolyte for a period that can be hours or days. Prior the test it is important preparing the sample, usually polishing it with SiC paper, then measuring the volume and weighting the sample with a high sensitive and accurate balance. The Mg corrosion leads to the formation of OH^- ions causing the electrolyte alkalization, thus a decrease of the corrosion rate is gradually observed due to the improvement of the surface layer passivation effect. For this reason, an accurate pH buffering is required in order to avoid eventual overestimation of the effective Mg alloy corrosion properties. Another critical step regards to the corrosion products removal. Actually, to appreciate the mass loss, an accurate corrosion products cleaning is required in order to avoid corrosion overestimation or underestimation due to an insufficient or excessive cleaning respectively. Such removing is obtained by immersion of the sample in a chromic acid solution. For a proper cleaning, a first short time immersion followed by the sample weight is suggested, then perform a second short time immersion and so on, until reach a stable mass value, meaning that all the corrosion products are removed avoiding eventual sample over corrosion. For accurate results, at least three repetitions are required.

4.2.2.2. Hydrogen evolution

For this test, an inverted funnel and burette filled with electrolyte are required, as exposed in Figure 62, in order to collect the H_2 bubbles evolved by the Mg corrosion by the cathodic reaction. The hydrogen evolution can be assessed by the electrolyte displacing on the top of the burette. The main difference with the mass loss one is the possibility to obtain multiple points over time. In fact, for obtaining points at

different time with mass loss test, different experiments have to be set-up. In addition, the corrosion products formation does not affect the corrosion rate estimation.

4.3 Materials and methods

The following work has been carried out in the laboratory of Nick Birbilis at Monash University, Melbourne Australia.

4.3.1 WE43 magnesium alloy preparation and microstructure analysis

The used WE43 magnesium alloy was obtained by means of direct chill casting obtaining the following alloy composition: 4 wt % Y, 3wt % rare earth (RE) mished metal, 0.2 wt % Zr, balance Mg. From the obtained ingot, a rectangular shape sample was cut and mechanical polished by using a 4000 grid SiC paper and with 0.5 μm colloidal silica until the microstructure was revealed. No chemical etching was needed for revealing the microstructure. After each step, the samples were sonicated for 5 minutes in pure ethanol. The magnesium morphology was assessed by means of a FEI Quanta 3D FEG Scanning Electron Microscopy coupled with EDAX Pegasus and TEAM X-ray analysis system and 10mm2 SDD with ultra-thin window. The images were taken via secondary electron employing 15 Kv as extraction voltage.

4.3.2 Used electrolytes and environments

The chosen electrolytes, involved in this work, are:

- *Minimum Essential Medium (MEM, Gibco®) with Earle's salt (ThermoFisher™),*
- *Dulbecco's Modified Eagle Medium (DMEM, Gibco®) +GlutaMAX™ with 4.5 g/l D-Glucose and 110 mg/l sodium pyruvate (ThermoFisher™).*

The formulation of such formulations are reported in Table 22.

All the corrosion measurements were performed both inside an incubator (5 vol. % CO_2 and about 95% of relative humidity), and in open-air environment for the purpose of comparing the effective CO_2 effect on the corrosion mechanism of WE43 magnesium alloy. Before performing the test in CO_2 controlled atmosphere, the electrolyte was left overnight in the incubator in order to allow the CO_2 adsorption until reach the equilibrium. In order to better simulate the human body environments, all the tests were performed at 37 ± 0.5 °C.

4.3.3 Electrochemical measurements

In Figure 63 the set-up used for the electrochemical measurements is showed. It involves a Biologic potentiostat linked to a three-electrode flat cell with a Saturated Calomel Electrode (SCE) as the reference, a platinum mesh as the counter electrode and filled with 200 ml of electrolyte. The working electrode was obtained mounted a rectangular shape samples in epoxy resin with a copper wire stuck with a conductive copper tape on the back. Total surface exposed is about 0.5 cm^2. Before each measurement, the working electrode is polished using Sic paper, up to 2000 grit, then sonicated for 5 min. in pure ethanol.

Regarding the potentiodynamic polarization measurements,an overpotential of ±0.25V *vs* OCP was applied, with a scan rate of 1 mV/s. Such test were performed after 10 minutes of open circuit potential (OCP) in order to reach the equilibrium potential.

From the obtained curves the Tafel-type fitting was assessed in order to extrapolate the corrosion current density (i_{corr}) and corrosion potential (E_{corr}) by using EC-lab® Software (version 11.27). In order to have a statistical significance, all measurements were replicated at least three times.

The electrochemical impedance spectroscopy (EIS) measurements were performed applying a voltage of 0.01V *vs* OCP in a frequency range from 10mHz to 100kHz. In this case, the working electrode (the sample) was polished until reaching a mirror-like surface by using 0.5 µm colloidal silica suspension. Even in this case the recorded EIS spectra were fitted by EC-lab Software (version 11.27) and the equivalent circuit models were defined.

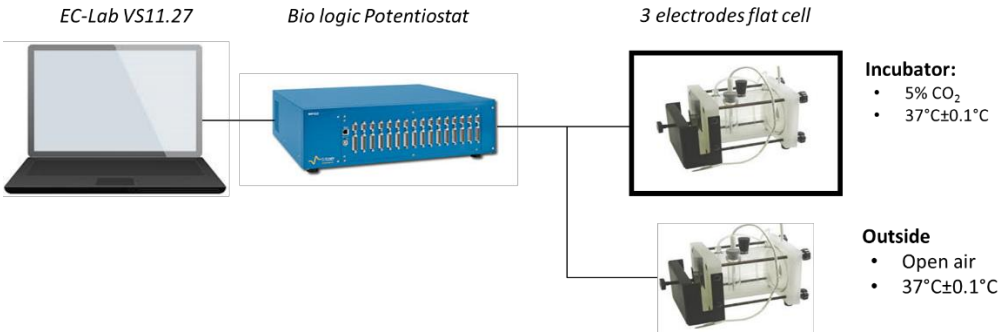

Figure 63: Measurement set-up employed for electrochemical tests.

4.3.4 Immersion test

For the immersion test, three samples (for each condition) were placed in three different beckers filled with 200 ml of electrolyte solution. Before the test the samples, with a total superficial area of 1 cm^2 were grinded with SiC paper up to 4000 grit, sonicated for 10 minutes in ethanol and weighed by high sensitive balance.

During the immersion, the pH was monitored as function of time. First measurement was collected before the samples immersion thereafter in the first 3 h

of immersion and then after 6 h and 24 h. Reached the 24 h the samples were removed from the solution and sonicated in ethanol for 3 min. From the samples corroded surfaces, it was possible assessing the corrosion morphology and characterizing the corrosion products by means of SEM and EDAX. Additional composition analyses were carried out by means of ATR, as described in section 3.2.1.

After the morphology characterization was possible removing the corrosion products, in order to assess the mass loss. In this case, the samples were treated with chromic acid for 10 minutes and weighed. Chromic acid is not aggressive for the metal surface, allowing therefore to remove the corrosion products without affecting the final result. The mass loss values are obtained using the follow equation:

$$M_{loss}\left(\frac{g}{cm^2}\right) = \frac{M_{initial}(g) - M_{final}(g)}{Surface\ Area(cm^2)} \qquad \text{eq. 49}$$

where M_{loss} is the mass loss in grams normalized by the surface area, $M_{initial}$ is the mass at the beginning of the immersion test, M_{final} is the final mass (following surface cleaning in chromic acid cleaning.

4.4 Results and discussion

4.4.1 Microstructure

Figure 64 shows the microstructure and the chemical composition map of the WE43 magnesium alloy obtained by means SEM and EDAX analyses. Such alloy exhibits two different phases:

- *First phase*: magnesium α-grains that is the main constituent observed in the microstructure, it is highlighted by the red dash line in the zoomed image
- *Second phases*: Intermetallic precipitation, they are the white phase indicated by the black arrows, they surround the magnesium α-grains and are formed mainly by Y and Nd. According to the literature such phases are formed by irregular precipitates of $Mg_{41}Nd_5$, longitudinal precipitates of β ($Mg_{14}Nd_2Y$) compounds, $Mg_{24}Y_5$ particles and by MgY particles having rectangular shape [118][119][120][121]

It is important assessing the alloy microstructure since the presence of the second phases have a great importance inasmuch they are cathodic particles with higher potential with respect to the α-grains magnesium matrix and therefore they promote the formation of galvanic corrosion.

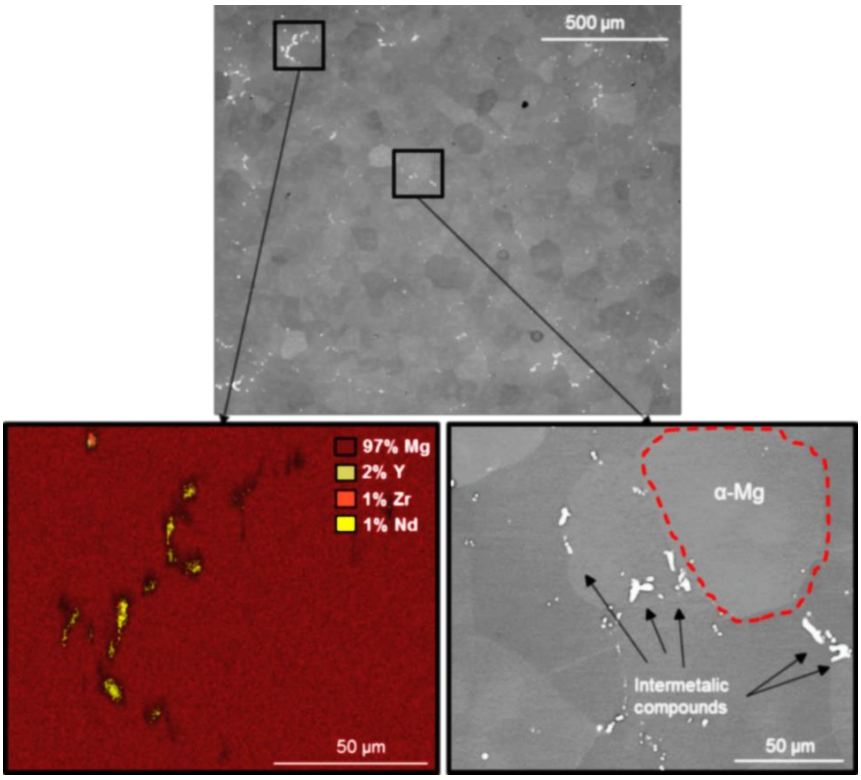

Figure 64: Microstructure of the WE43 alloy and relative EDAX measurement.

4.4.2 Potentiodymanic polarisation measurements

The results of the polarization measuements carried out in open air and in controlled atmosphere for MEM and DMEM electroytes are exposed in Figure 65-a and Figure **65**-b respectivelly. Figure 65-c actually, shows the OCP evolution for the first 20 minutes of immersion for all the test conditions.

It is clear that the presence of CO_2 affects the magnesium alloy corrosion kinetic in both the electrolytes, in fact it is possible to observe a similar curve's shifting for both cases. An explanation of such shifting can be connected to the CO_2 saturation, which leads the accumulation of of CO_3^- and H^+ ions, inside the electrolytes until the equilibrium is reached. As a matter of fact, the presence of carbonates promotes a fast precipitation of calcium carbonates and magnesium carbonates, which have an inhibition effect towards the cathodic particles. Such cathodic inhibition can be observed by both the shifting on the left, toward lower current density, of the cathodic branches (as showed in Figure 65) and by the lower OCP recorded for the samples tested in controlled atmosphere. Actually, the cathodic particles have higher potential with respect the magnesium matrix one therefore their inhibition lead to a decrease of the overall measured potential.

On the other hand, the presence of H^+ ions decreases the electrolyte pH value improving its aggressiveness against the Mg alloy then increasing its dissolution toward the solution. Actually, the anodic branches are shifted on the right causing a worst corrosion behaviour of the material.

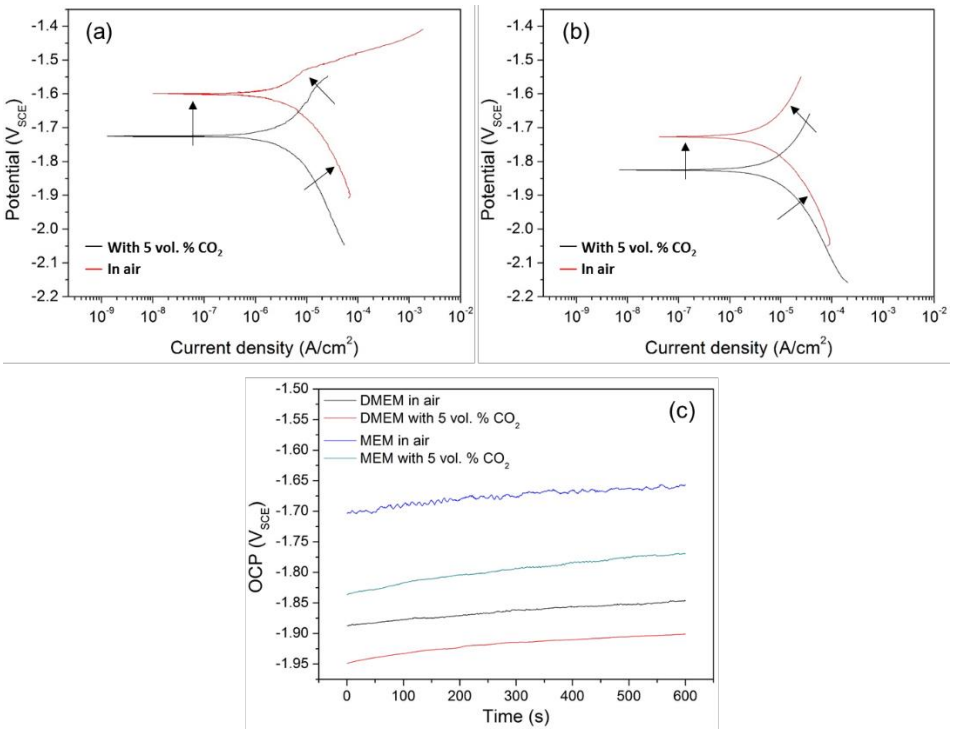

Figure 65: Polarization curves for WE43 immersed in MEM (a), in DMEM (b) and relative OCP measured within 600 s (c).

The i_{corr} and E_{corr} extrapolated by means of Tafel extrapolation are exhibited in Table 23 and it is clearly that the DMEM electrolytes is more aggressive than the MEM one since it is always the higher i_{corr} values. Moreover, the results show lower corrosion currents for the samples treated in air in both electrolyte, standing for a less detrimental environment. The reason behind such better results is due to the cathodic inhibition caused by the carbonates, which reduce the corrosion current of the Mg alloy.

Regarding the E_{corr}, even in this case the values are lower for the samples measured inside the incubator meaning that the cathodic particles were inhibited decreasing the overall OCP vs V_{sce} of the alloy.

Table 23: i_{corr} and E_{corr} extrapolated by the polarization curves.

	i_{corr} (µA/cm²)	E_{corr} (V_{SCE})
MEM in air	12±5.4	-1.62±0.04
MEM 5 vol. % CO_2	10.4±3.8	-1.67±0,05
DMEM-in air	23.1±3.3	-1.77±0.03
DMEM 5 vol. % CO_2	21.7±2.2	-1.84±0.02

4.4.3 Electrochemical impedance spectroscopy

In Figure 66, the Nyquist plots recorded after 1 h and 24 h of immersion in both electrolytes (DMEM and MEM) are exhibited. For both cases, a similar trend is observed between the two atmospheres (in open air and with vol. % CO_2), in fact

after 24 h of immersion the capacitive loops, recorded for each sample, are characterized by a larger diameter than the ones obtained after 1 h of exposition. Such increase means that the corrosion protection increases over time, due to the formation of a protective layer on the alloys surface.

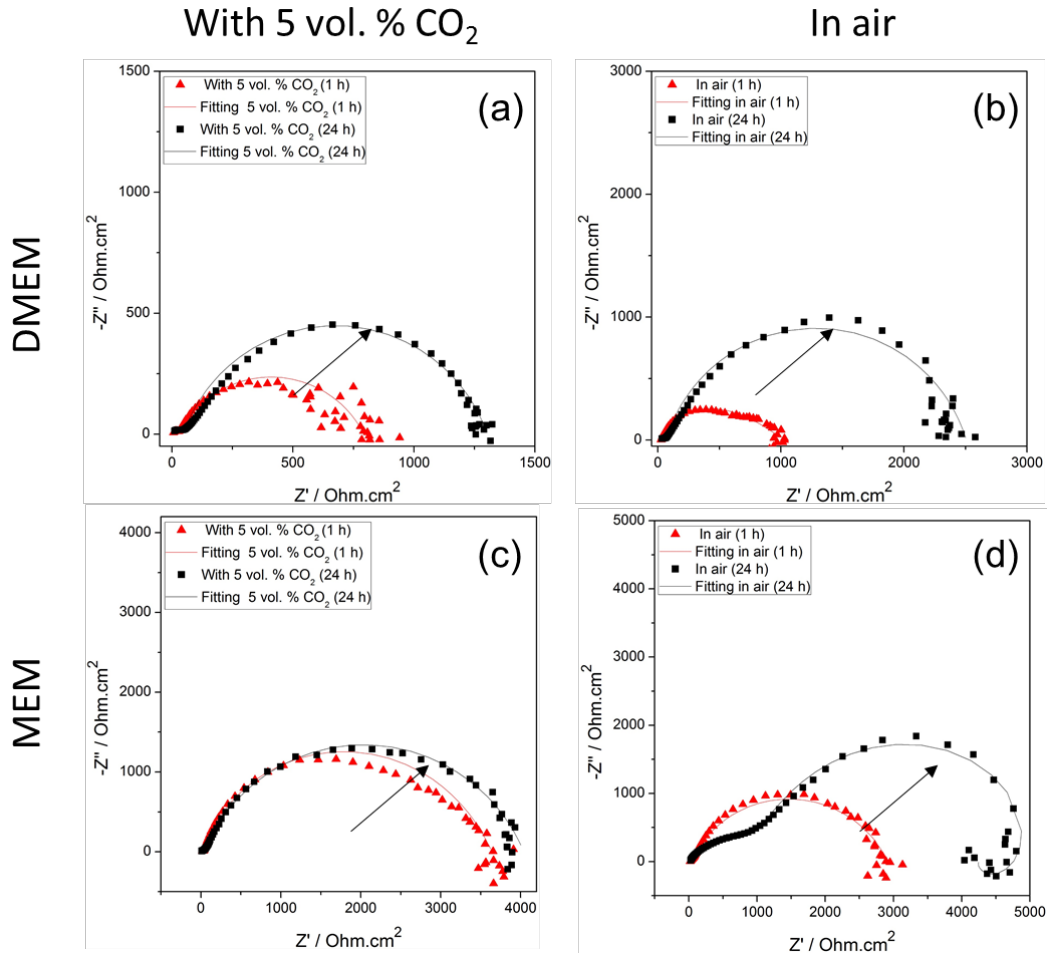

Figure 66: Nyquist plots obtained after 1 h and 24 h of immersion in DMEM in controlled atmosphere (a) and in air (b) and in MEM in controlled atmosphere (c) and in air (d).

The Nyquist plots are characterized by two capacitive loops:

- *A small capacitive loop at high frequencies:* it is correlated to the charge transfer resistance (R_{ct}) and double layer/oxide effects. Only for MEM in air case, such capacitive loop shows a larger diameter than the other cases, this means that the surface film provides a better corrosion protection.
- *A large capacitive loop at mid-low frequencies:* such loop can be correlated to mass transport relaxation. Such phenomena can be caused by diffusion of Mg^{2+} through the corrosion layer toward the electrolyte and can be correlated to the capability to protect the underneath metal from the corrosion by the protective film.

Furthermore, the MEM in open air case achieved an inductive loop at low frequencies, a typical features frequently reported in literature [84] that is related to the formation of localized corrosion on the metallic surface. In general, larger capacitive loops are recorded for the samples immersed in MEM electrolytes with respect to DMEM, implying that in MEM solution the corrosion products formed on the surface allow a better corrosion protection.

In order to better understand the electrochemical behaviour recorded by EIS measurements, two equivalent circuit models are proposed in Figure 67, able to fit the plots obtained in all conditions. The corrosion reactions, which occur onto metallic surface, do not lead to a homogeneity system; therefore, a CPE (constant phase element) was chosen instead of a pure capacitive element.

The first resistor element (Rs) represents the electrolyte resistance that is clearly affect by the presence of CO_2. In fact, the high presence of carbonates leads to a drastic decrease of the resistance recorded for the solution, as exposed in Table 24. The high frequencies capacitive loops are described by CPE_{dl} and R_{ct}, which represent the charge transfer resistance and electric double layer capacitance respectively. CPE_f and R_f, actually, represent the mass transport relaxation at the mid-low frequencies capacitance loop. Only for MEM in air case (circuit in figure 68-a) it is present R_l and L which describe the inductive loop at low frequencies.

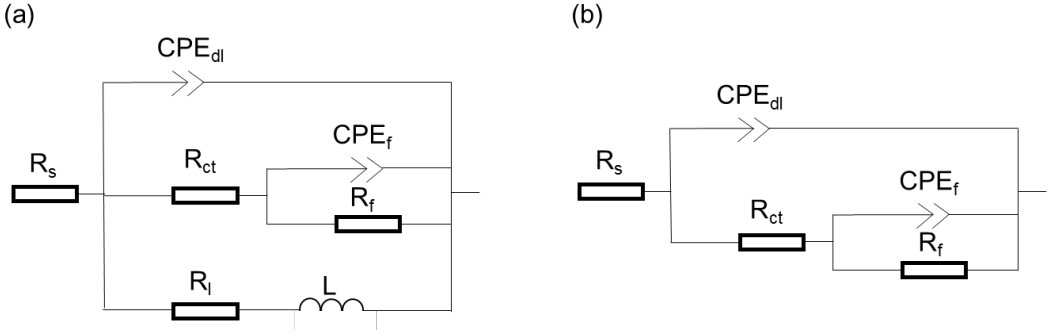

Figure 67: Proposed equivalent circuits.

The results in Table 24 show that for both the employed electrolytes, higher value of R_f are obtained after 24 h of immersion, with about 4500 $\Omega.cm^2$ and 2433.6 $\Omega.cm^2$ for MEM and DMEM, respectively. Such results confirm that in open air the corrosion products create a more protective surface layer.

The equivalent circuit can provide further information about the alloys corrosion behaviour by means of the $1/R_P$ ($\Omega^{-1}.cm^{-2}$) values, which can be extrapolated by the follow equations

$$\frac{1}{Rp} = \frac{1}{R_f + R_{ct}} + \frac{1}{R_L} \qquad \text{eq. 50}$$

$$\frac{1}{Rp} = \frac{1}{R_f + R_{ct}} \qquad \text{eq. 51}$$

For the equivalent circuit that exhibits an inductive behaviour and for the circuits without inductive behaviour respectively. $1/R_P$ is correlated to the corrosion

current of the samples. The results are exhibited in Table 24 and it is observed that, after 1h of immersion, the sample immersed in MEM in controlled atmosphere, shows a lower $1/R_P$ value with respect the one obtained in open air, implying that the corrosion layer achieved good protective capabilities in the early stage of immersion with the presence of carbonates inside the solution but the situation is inverted after 24 h of immersion. As a matter of fact, the samples in air reaches the lower $1/R_P$ value, meaning that the protective layer gains higher protection capability, while for the one in controlled atmosphere, such value decreased a little bit. By using DMEM electrolyte, the results show a quite different situation. Even if the trend is similar, after 1 h the sample treated in CO_2 atmosphere has $1/R_p$ value slightly higher than the in air one (only 0.4 points of difference) while after 24 h the difference is more marked, then the absence of a controlled atmosphere allows the formation of a surface layer more protective over time.

Table 24: Values extrapolated by the equivalent circuits for all the samples.

	MEM In air		MEM 5 vol. % CO_2		DMEM In air		DMEM 5 vol. % CO_2	
	1 h	**24 h**	**1 h**	**24 h**	**1 h**	**24 h**	**1 h**	**24 h**
R_S ($\Omega \cdot cm^2$)	18	21	5	3.7	14.4	25.4	3.1	3.1
CPE_{dl} ($\mu F\ cm^{-2}s^{(n-1)}$)	0.5	5	0.13	9.4	0.02	3.6	1.9	0.13
n_{dl}	0.7	0.71	0.64	0.7	0.4	0.78	0.8	0.8
R_f ($\Omega \cdot cm^2$)	48	1200	32.5	44.6	16.8	46.8	27.5	48.8
CPE_f ($\mu F\ cm^{-2}s^{(n-1)}$)	0.33	0.26	9.3	0.3	0.15	0.31	0.64	0.03
nf_l	0.75	0.83	0.86	0.72	0.9	0.82	0.7	0.79
R_f ($\Omega \cdot cm^2$)	2850	4500	3600	3906	998.4	2433.6	762.5	1250.5
L ($H \cdot cm^{-2}$)	-	7500	-	-	-	-	-	-
R_l ($\Omega \cdot cm^2$)	-	15000	-	-	-	-	-	-
$1/R_P$ ($\Omega^{-1} \cdot cm^{-2}$)	$3.5x10^{-4}$	$2.4x10^{-4}$	$2.8x10^{-4}$	$2.5x10^{-4}$	$9.8x10^{-4}$	$4x10^{-4}$	$1.3x10^{-3}$	$7.7x10^{-4}$

4.4.4 pH monitoring

Figure 68 exhibits the pH variation of the solution up to 24 h during the immersion test in each environment. The first point was taken before the immersion of the samples inside the solutions and, for the controlled atmosphere cases, after the overnight exposure in CO_2 environment. The high CO_2 pressure generates the formation of CO_3^- and H^+ ions by means of the following reactions:

$$CO_{2\,(g)} \rightarrow CO_{2\,(aq)} \qquad \text{eq. 52}$$

$$CO_{2\,(aq)} + H_2O \rightarrow H_2CO_{3\,(aq)} \rightarrow H^+_{\,(aq)} + HCO_3^-{}_{(aq)} \qquad \text{eq. 53}$$

$$HCO_3^-{}_{(aq)} \rightarrow H^+ + CO_3^- \qquad \text{eq. 54}$$

Therefore, the overnight saturation leads to lower pH values for both MEM and DMEM electrolytes (about 0.2 points each) due to the release of H^+ ions (eq. 44). After the immersion of the samples, a slow and negligible increase pH increase was recorded within the first 6 h for both cases, after that they reach the stable pH value where are not possible to be appreciate its further changing.

A different situation was obtained for the monitoring performed in open air environment, actually the pH sharply increases during the first 6 h until reaching the value of 8.7 within the 24 h. Such different behaviour is caused by the absence of a buffer effect of the carbonates inside the solution that allows the pH values to not change, without their substantial growths.

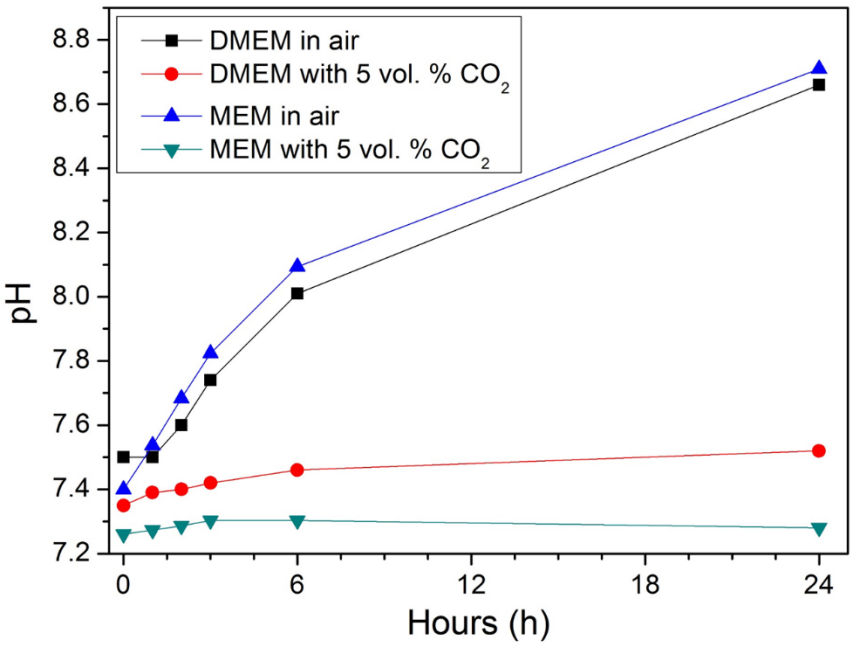

Figure 68: pH variation within 24 h of immersion in both DMEM and MEM, with and without a controlled atmosphere.

4.4.5 Mass loss rate

The mass loss results are put in correlation with the results obtained by EIS measurements after 24 h of immersion ($1/R_P$) and potentiodynamic polarization (i_{corr}) curves in Figure 69. The mass loss test highlights the following corrosion rate ranking:

1. *DMEM (5 vol. % CO_2)*
2. *DMEM (air)*
3. *MEM (5 vol. % CO_2)*
4. *MEM (air).*

Moreover, the results suggest that the long-term tests (immersion and EIS) are less detrimental for the magnesium corrosion when performed in open air environment. Generally, it is clear that DMEM solution is more aggressive than MEM one in both controlled and not controlled atmosphere.

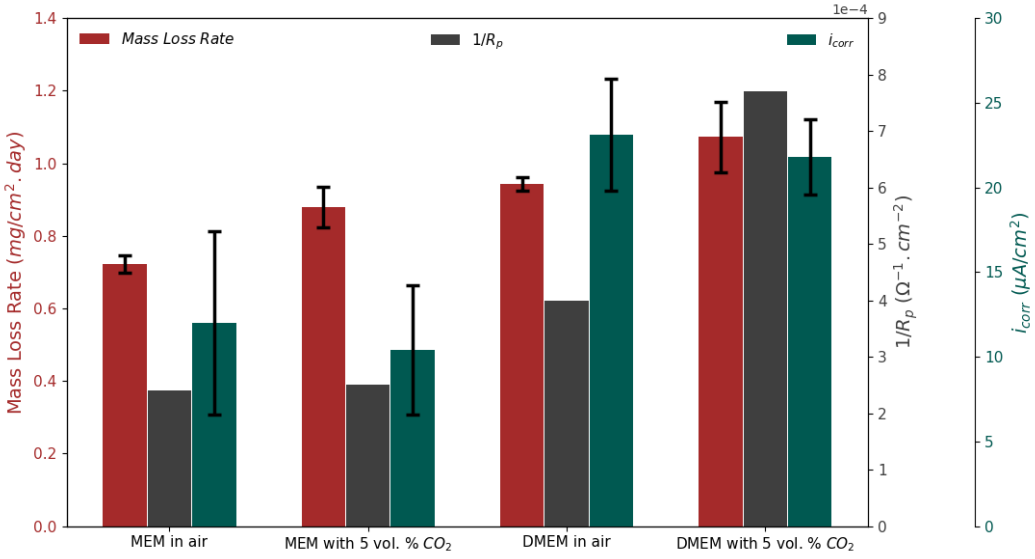

Figure 69: Mass loss rate, $1/R_p$ and i_{corr} obtained for each sample in each environment.

4.4.6 SEM and EDAX Measurements

Before treating the immersion test samples with chromic acid, the corrosion products were characterized by means of SEM and EDAX analyses in order to assess their morphology and composition. The obtained results are showed in Figure 70 and Figure 72 respectively. The morphological characterization highlights a high corrosion products coverage on the surface of the samples immersed in both MEM and DMEM solutions in controlled environment with 5 vol. % CO_2. Such corrosion layers are not uniform but show cracks, which form a chip-like morphology that are caused by the sample dehydration during the drying process. Moreover, high Ca and P precipitations and agglomerations were detected

in delimitated spots (red arrows) surrounded by corrosion-less zones, where the corrosion processes were inhibited (Figure 70-a and Figure **70**-b). Regarding the samples immersed in open air, it is possible to observe two different cases. In MEM electrolyte only few and sporadic corrosion products were detected, even if the Ca and P agglomerations are always present. For the DMEM case, actually, a higher presence of corrosion products was detected on its surface, but the coverage is not so well defined as for the samples exposed in the CO_2 environment.

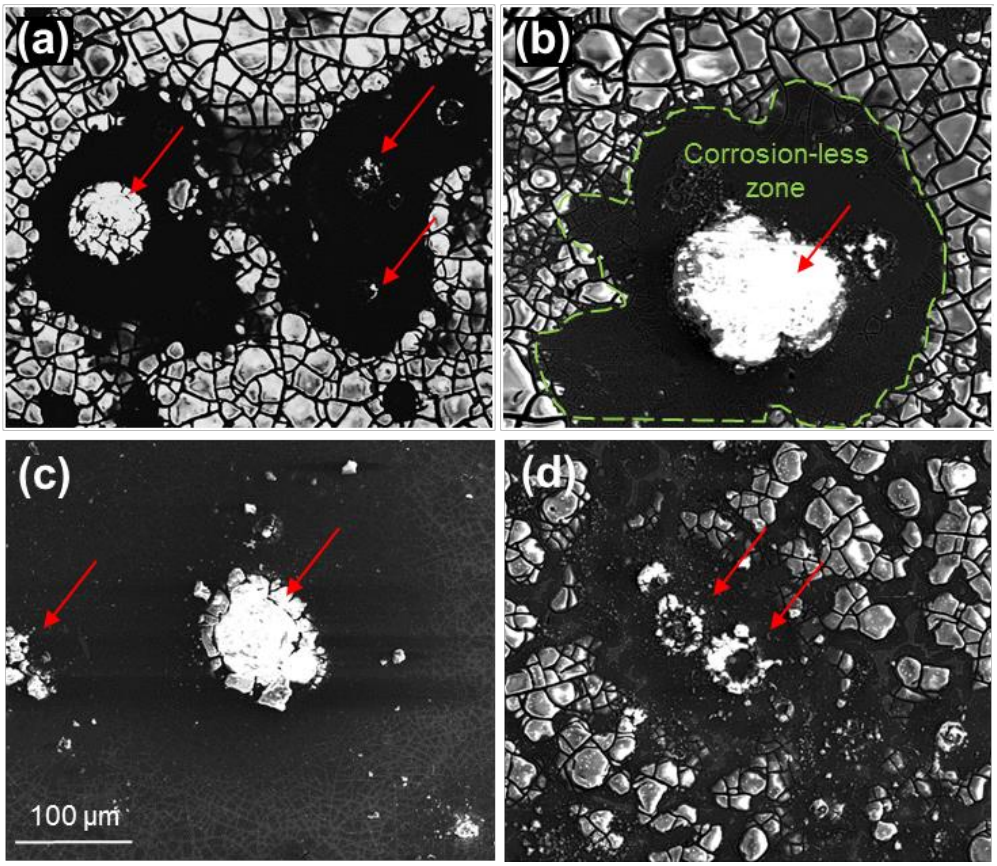

Figure 70: Corrosion morphologies collected after 24 h of immersion test.

The samples surface composition maps are exposed in Figure 72 and it is highlighted that the corrosion products are constituted by O, Ca, P, Cl, C and S, suggesting that they are mainly composed by inorganic compounds. In particular the high presence of Ca and P can be related to the precipitation of hydroxyapatite as well as to other undissolved CaP compounds such as $Ca_3(PO_4)_2$. It can be confirmed by the infrared analyses in Figure 71, which highlight the presence of phosphate (PO_4^{3-}) group peaks at 1170 cm^{-1} and 560 cm^{-1} for ν_3 and ν_2 mode respectively [122]. The peaks related to the carbonate group (CO_3^{2-}) are detected at 1170 cm^{-1} and 560 cm^{-1} that is in line with the presence of carbonate groups as well as the hydroxyapatite

DMEM and MEM solutions are characterized by the presence of relevant concentration of organic compounds as amino acids. Which can be absorbed by the corrosion products on the samples surface. For this reason, high presence of C is

detected on their surface. In addition, the presence of CO_2 promotes the formation and precipitation of carbonates (e.g. $CaCO_3$). As explained before, the WE43 sample, immersed in the MEM electrolyte in air, not shows corrosion products on its surface. In this case, a thin layer that can be attributed to hydroxyapatite (EDAX analysis shows an important presence of Ca and P), can be observed onto the alloy surface. It can be justified by the high pH, which is able to stabilize this layer, not allowing to the corrosion process to move forward as fast as on the sample exposed to the CO_2 environment.

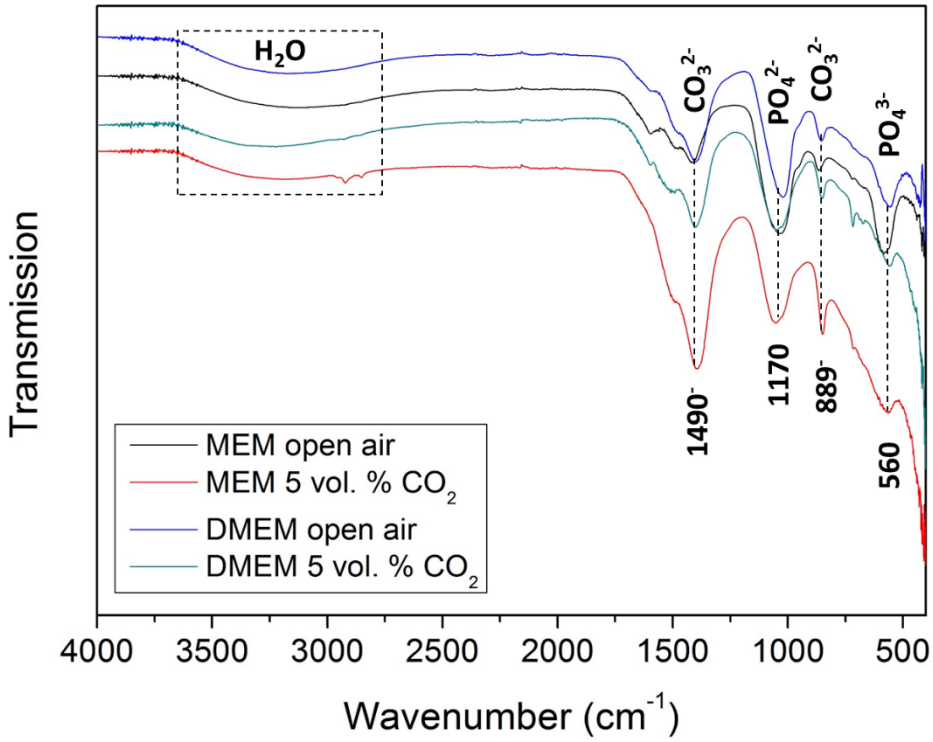

Figure 71: Infrared spectra of the surface corrosion products after 24 h of immersion.

Regarding the sample immersed in DMEM solution in air, the morphology shows a non-uniform corrosion patina on its surface, but anyway the corrosion products are more marked with respect the sample treated always in open air but in MEM solution. The reason can be correlated to the higher presence of amino acids in DMEM formulation, which can cause a lower stability of the surface film increasing the Mg dissolution.

The precipitation of the Ca-P rich zones can be generated by a local pH increase. In particular, the high presence of second phases in the WE43 microstructure can promote the cathodic processes in their proximity therefore increase locally the formation of OH^- ions. The results of such pH increase generate a suitable environment for the precipitation of these Ca-P agglomerations that are also called volcano-like deposits due to the presence of holes caused by the formation of H_2 during the cathodic reaction. The local pH increase can also explain

the presence of a corrosion-less zone; in fact, the high pH can inhibit the Mg dissolution reducing the corrosion process in such zones.

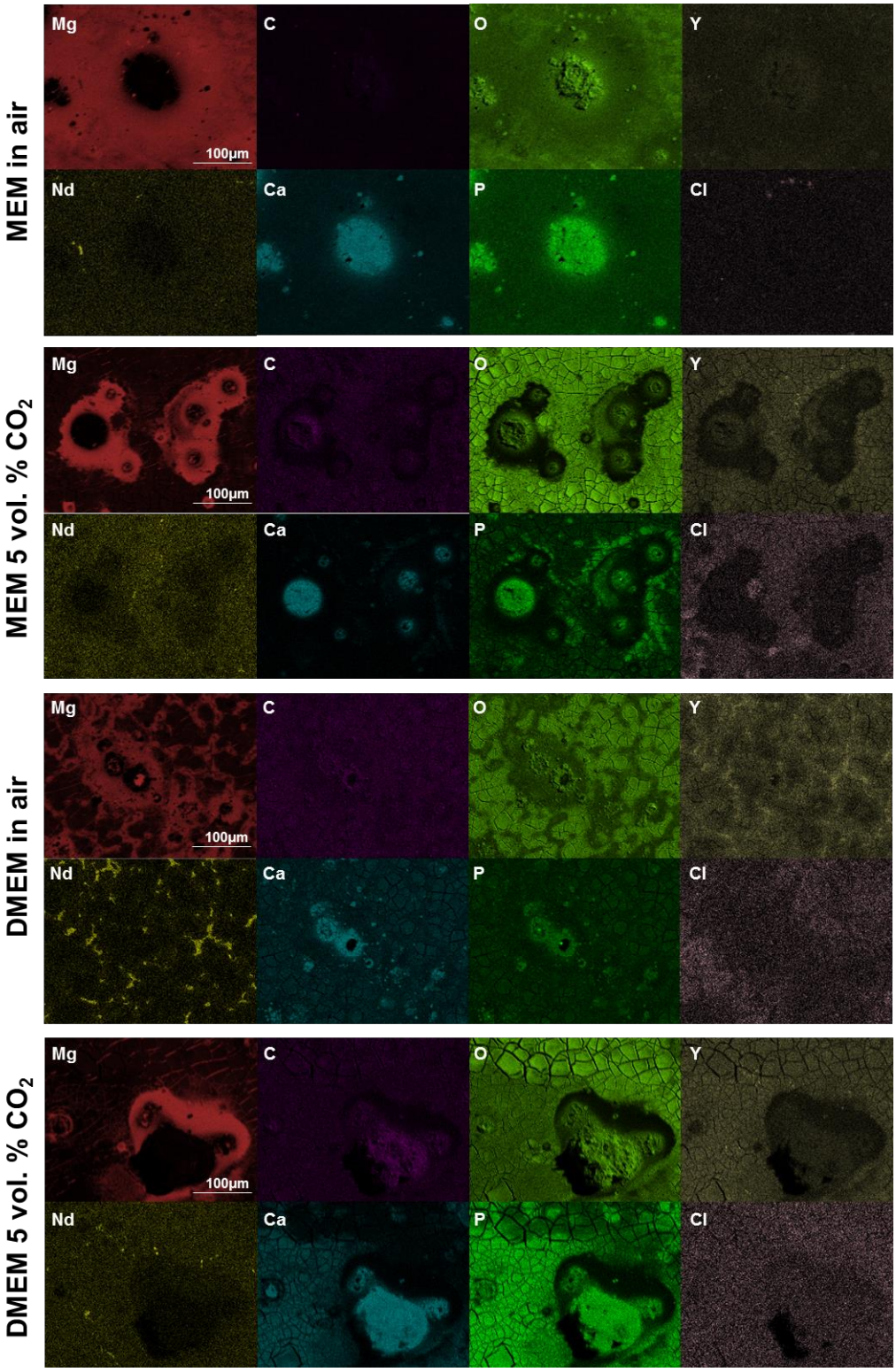

Figure 72: EDAX composition analysis obtained after 24 h of immersion. Analysed areas of Figure 70.

4.5 Discussion

Aim of this work is to assess the effect of CO_2 atmosphere on the corrosion of magnesium WE43 alloy for biomedical application in MEM and DMEM electrolyte. Such investigation is led by the necessity to keep the electrolyte pH at the constant value of about 7.3; since higher value can be harmful for the human body then it is not realistic scenario. MEM and DMEM are two solutions that are characterized by a formulation close to the human one and the high presence of carbonates allows to control and buffer the own pH in presence of 5 vol. % CO_2 environment. The absence of such controlled atmosphere causes a drastic pH increase inside the electrolytes, from about 7.3 to 8.6 and 8.7 for DMEM and MEM, respectively. Besides the harmful effects caused by high pH value, such increase can also overestimate the magnesium corrosion properties, as observed by the performed test in this work (EIS and mass loss). The main reasons behind such overestimation corrosion properties are:

- *Promotion of hydroxyapatite onto magnesium surface*
- *$Mg(OH)_2$ stability for pH value higher than 8.5*

MEM and DMEM electrolyte formulations present noteworthy amount of calcium and phosphate components that, in presence of OH^- ions promote the formation and the precipitation of hydroxyapatite, which can cover the magnesium surface generating a protective layer. Furthermore, they are also characterized by the presence of organic compounds, which can be absorbed by the $Mg(OH)_2$ layer, with the effect to improve the protective barrier.

The second reason that leads to a corrosion overestimation in absence of buffering, according to Pourbaix diagram, is that for pH higher than 8.5 the corrosion processes are blocked by the presence of insoluble $Mg(OH)_2$. In fact, in alkaline solution it is possible to obtain a more stable and compact magnesium hydroxide layer that improve the corrosion protection of the underneath metal.

From the results, it is clear that DMEM solution is more aggressive than the MEM one, and it can be elucidated by the different formulation. In fact, MEM electrolyte is composed by the presence of Earle's Salts, which bring higher concentrations of Ca and P, making easier the precipitation of insoluble $Ca_3(PO_4)_2$ salts onto the Mg alloy surface improving the corrosion resistance when the pH increases. Furthermore, DMEM has higher concentration of amino acids which can improve the dissolution of magnesium dissolution toward the solution.

It is important to say that the results highlight a beneficial effect about the corrosion behaviour of WE43 magnesium alloy in presence of a constant pressure of CO_2 during the early stage of immersion. As a matter of fact, polarization test reveals lower current density for the correlated to the cathodic reaction for the samples treated inside the incubator, as well as lower E_{corr} and OCP were recorded. The reason of such results can be associated to the inhibition of the cathodic particles, present inside the microstructure, by the carbonates generated by the high

pressure of CO_2. This means that for the early stage of immersion the cathodic kinetic is strongly affected by the carbonates, resulting in better corrosion properties. However, the corrosion processes generate high concentration of OH^- ions, causing a pH increase for the solution in open air without buffering. The results show that such increase causes a reduction in term of corrosion rate for the samples immersed in open air with respect to the ones immersed in controlled atmosphere. This suggests that the pH increase has an important effect with respect the cathodic inhibition, therefore the absence of buffered CO_2 electrolytes can lead to an underestimation of the corrosion rate for long-term analysis.

4.6 Conclusions

The results obtained in this work highlight how the presence of CO_2 can affect the corrosion behaviour of the WE43 magnesium alloy in both long-term and short-term analyses, in particular:

- A controlled CO_2 atmosphere can reduce the magnesium alloy cathodic kinetic and concomitantly decreases the E_{corr}. Such effect can be attributed to the inhibition of the cathodic particles due to the presence of carbonates inside the solution that causes lower i_{corr}. The results of such observation suggest that for the early stage of immersion the corrosion behaviour is marked affected by the second phase inhibition
- The results obtained by mass loss rate highlight higher corrosion rate when the samples are exposed in controlled CO_2 atmosphere. Therefore, the absence of buffering and subsequently increase of pH as an important effect on magnesium alloy corrosion with respect to cathodic inhibition in time. These results suggest that for long-term analyses the solution alkalization effect has an important role on Mg corrosion mechanism, leading to an overestimation of the effective corrosion properties of the studied alloy.
- The surface morphologies show lower presence of corrosion products on samples immersed in MEM electrolyte in open air after 1 day of immersion. While the sample immersed in DMEM electrolyte, always in open air, shows higher corrosion products. Such results suggest that DMEM formulation is more aggressive than MEM one due to the presence of higher concentration of amino acids. The results are confirmed by mass loss test.

Conclusions

In this dissertation, results obtained about three different topics concerning to biomedical applications are presented.

The first topic deals with the realization of conductometric gas sensors for breath test analysis and the results were discussed in chapter 2 and 3. It has been chosen Nb_2O_5 as sensing film for the realization of sensors for acetone and ethanol sensing, while Nb_2O_5 enriched with Pt particles thin film for H_2 detection. Niobium oxide films were deposited by reactive sputtering and XPS analyses confirm the presence of niobium with oxidation number 5. Three different deposition parameters were employed affecting the obtaining morphologies and thicknesses. The Pt enrichment was obtained by a second sputtering deposition of a pure Pt followed by a heat treatment. The sensors characterized only by Nb_2O_5 exhibit sensing responses strictly correlated with the film morphology and the achieved thickness. Starting with acetone detection, sensor 1 and 3, having compact with thickness of 200 nm and 160 nm respectively, present the best results at 350 °C as working temperature with responses of about 3.99 and 2.73 respectively, toward 5 ppm of acetone. On the contrary, sensor 2, characterized with a columnar morphology with a thickness of about 900 nm, exhibits the best results at 300 °C with a maximum response of 1.8, drastically lower with respect to the responses of sensor 1 and 3. This means that thin layers play an important role in order to obtain best responses toward acetone. The morphology has a key role also for the sensor response time, since compact layers guarantee a fast reaction toward the target gas with respect to a columnar morphology where the gas requires time to diffuse inside the film. Actually, sensor 1 and 3 achieve about 3.6 s and 5 s respectively as response time, while sensor 2 reach the steady state only after 46.1 s. Regarding the sensitivity, the sensors guarantee responses toward 1 ppm of acetone and a linear response within 3 ppm. The columnar morphology allows to detect higher concentration since higher surface is exposed. Even the selectivity shows quite good results since the only interefernt gas is the ethanol but fortunately, it is present inside the human breath only after the consumption of alcoholic beverage. For this reason, such sensors can be also employed for ethanol sensing. At this scope, sensor 1, which achieved the best sensing responses toward acetone, has been characterized toward ethanol sensing. The results exhibit excellent sensitivity and stability making such sensor a suitable candidate to be implemented in measurement system devices.

Regarding Nb_2O_5 sensing film enriched with Pt agglomerates, it has been observed that it is possible to detect high H_2 concentrations obtaining noteworthy results in terms of sensor responses and stability. In particular, both proposed

sensors exhibits excellent results at low temperature (about 200 °C) with an immediate response time of about 3.6 s for both sensors. Even the selectivity exhibit outstanding results since the sensors react only toward hydrogen and no interfers were detected. Unfortunately, such sensors show low sensitivity since they do not exhibit responses at low H_2 concentrations. Therefore, they cannot be implemented for breath analysis where the concentrations in play do not exceed 40 ppm.

The second topic, presented in chapter 3, is a proof of concept about the combination of two measurements (EIS and ICP-AES) in order to characterize SiO_x thin films enriched with Cu nanoparticles in term of both corrosion protection and Cu release for an antifungal effect. The interested films were obtained by coupling PECVD and sputtering deposition at the same time onto glass substrates. The proposed approach shows an interesting correlation between the Cu concentration measured daily by ICP-AES and the evolution of the EIS measured module. Furthermore, it was possible to observe how the deposition RF-power has an important role for obtaining a suitable thin film. In fact, lower RF-powers allow the realization of coatings characterized by lower stiffness, which guarantee a better cohesion and conformability toward the underneath substrate. On the contrary, higher RF- powers generate fragile film with low conformation capability with can lead to premature breakdown.

The third and last topic, described in chapter four, faces the effect of CO_2 on the magnesium corrosion. In particular, a WE43 alloy has been involved for biomedical corrosion measurements in two different MEM formulations where used as electrolyte, with and without a controlled CO_2 atmosphere. Polarization test highlights that the carbonates, formed by the presence of CO_2, inhibit the cathodic particles present into WE43 microstructure reducing the cathodic reaction. At the same time, such inhibition affects also the recorded OCP, shifting it toward lowers values. On the contrary, the pH increases over time in absence of the buffering effect by the CO_2 atmosphere. Therefore, long-term measurements show an increase in term of corrosion rate for the samples treated in presence of CO_2. To conclude, in order to better simulate a biological environment, it is necessary involve an incubator in order to guarantee a controlled CO_2 atmosphere for the characterization of magnesium alloys for biomedical applications.

In conclusion, in this dissertation interesting results have been achieved in different biomedical applications, highlighting the importance of the employment of appropriate measurement techniques for the characterization of sensing devices as well as materials for biomedical tools.

References

[1] L. Lombardo *et al.*, "High Sensitive and Selective Minisensor for Acetone Monitoring," *IEEE Trans. Instrum. Meas.*, vol. 69, no. 6, pp. 3308–3316, 2020.

[2] L. Lombardo *et al.*, "Nb 2 O 5 thin film-based conductometric sensor for acetone monitoring," in *IEEE International Symposium on Medical Measurements and Applications - Instambul 2019*, 2019.

[3] A. Gullino *et al.*, "Employment of Nb 2 O 5 thin-films for ethanol sensing," in *IEEE International Instrumentation and Measurement Technology Conference 2020 - Dubrovnik*, 2020, pp. 2–6.

[4] D. Rosenfeld, P. E. Schmid, V. Demarne, and A. Grisel, "Electrical transport properties of thin-film metal-oxide-metal Nb205 oxygen sensors," *Sensors Actuators B*, vol. 37, no. 1996, pp. 83–89, 1996.

[5] C. Wang, L. Yin, L. Zhang, D. Xiang, and R. Gao, "Metal Oxide Gas Sensors: Sensitivity and Influencing Factors," *Sensors*, vol. 10, pp. 2088–2106, 2010.

[6] L. Chambon, A. Pauly, J. P. Germain, C. Maleysson, V. Demarne, and A. Grisel, "A model for the responses of Nb 2 O 5 sensors to CO and NH 3 gases," *Sensors Actuators B. Chem.*, vol. 43, no. 1–3, pp. 60–64, 2007.

[7] R. Ab, R. Abdul, A. Sabirin, and J. Zhen, "Nb 2 O 5 Schottky based ethanol vapour sensors : Effect of metallic catalysts," *Sensors Actuators B. Chem.*, vol. 202, pp. 74–82, 2014.

[8] K. Kim, S. A. Jahan, and E. Kabir, "A review of breath analysis for diagnosis of human health," *Trends Anal. Chem.*, vol. 33, pp. 1–8, 2012.

[9] T. L. Mathew, P. Pownraj, S. Abdulla, and B. Pullithadathil, "Technologies for Clinical Diagnosis Using Expired Human Breath Analysis," *Diagnostics*, vol. 5, pp. 27–60, 2015.

[10] C. Ghosh, V. Singh, J. Grandy, and J. Pawliszyn, "Recent advances in breath analysis to track human health by new enrichment technologies," *J. Sep. Sci.*, vol. 43, no. 1, 2020.

[11] R. A. Dweik and A. Amann, "Exhaled breath analysis: the new frontier in medical testing," *J. Breath Res.*, vol. 2, no. 3, 2008.

[12] M. Phillips, J. Herrera, S. Krishnan, M. Zain, J. Greenberg, and R. N. Cataneo, "Variation in volatile organic compounds in the breath of normal humans," *J. Chromatogr. B*, vol. 729, pp. 75–88, 1999.

[13] R. Mukhopadhyay, "Don't waste your breath," *Anal. Chem.*, vol. 76, pp. 273–276, 2004.

[14] W. Miekisch, J. K. Schubert, and G. F. E. Noeldge-schomburg, "Diagnostic potential of breath analysis — focus on volatile organic compounds," *Clin. Chim. Acta*, vol. 347, pp. 25–39, 2004.

[15] Z. Wang and C. Wang, "Is breath acetone a biomarker of diabetes ? A historical review on breath acetone measurements," *J. Breath Res.*, vol. 7, 2013.

[16] A. Gasbarrini *et al.*, "Methodology and indications of H 2 -breath testing in gastrointestinal diseases : the Rome Consensus Conference," *Aliment. Pharmacol. Ther. Methodol.*, vol. 29, no. 1, pp. 1–49, 2009.

[17] M. Di Stefano and G. R. Corazza, “Role of hydrogen and methane breath testing in gastrointestinal diseases,” *Dig. Liver Dis. Suppl.*, vol. 3, no. 2, pp. 40–43, 2009.
[18] S. Bevc *et al.*, “Measurement of breath ammonia for detection of patients with chronic kidney disease,” *Clin. Nephrol.*, vol. 88, pp. 14–17, 2017.
[19] P. Keyur, “Noninvasive tools to assess liver disease,” *Curr. Opin. Gastroenterol.*, vol. 26, no. 3, pp. 227–233, 2010.
[20] H. Awad, M. M. Khamis, A. El-aneed, H. Awad, and M. M. Khamis, “Mass Spectrometry , Review of the Basics : Ionization,” *Appl. Spectrosc. Rev.*, vol. 50, no. 2, pp. 158–175, 2015.
[21] W. Cheng and W. Lee, “Technology development in breath microanalysis for clinical diagnosis,” *J. Lab. Clin. Med.*, vol. 133, no. 3, pp. 218–228, 1999.
[22] T. Holm, “Aspects of the mechanism of the flame ionization detector,” *J. Chromatogr. A*, vol. 842, pp. 221–227, 1999.
[23] S. Armenta, M. Alcala, and M. Blanco, “A review of recent , unconventional applications of ion mobility spectrometry (IMS),” *Anal. Chim. Acta*, vol. 703, no. 2, pp. 114–123, 2011.
[24] R. S. Blake, P. S. Monks, and A. M. Ellis, “Proton-Transfer Reaction Mass Spectrometry,” *Chem. Rev.*, vol. 44, pp. 861–896, 2009.
[25] A. Boschetti, F. Biasioli, M. Van Opbergen, C. Warneke, and A. Jordan, “PTR-MS real time monitoring of the emission of volatile organic compounds during postharvest aging of berryfruit,” *Postharvest Biol. Technol.*, vol. 17, pp. 143–151, 1999.
[26] B. Henderson *et al.*, “Laser spectroscopy for breath analysis : towards clinical implementation,” *Appl. Phys. B*, vol. 124, no. 8, pp. 1–21, 2018.
[27] A. Ponzoni *et al.*, “Metal Oxide Gas Sensors, a Survey of Selectivity Issues Addressed at the SENSOR Lab , Brescia (Italy),” *Sensors*, vol. 17, p. 714, 2017.
[28] G. Korotcenkov and B. K. Cho, “Metal oxide composites in conductometric gas sensors : Achievements and challenges,” *Sensors Actuators B. Chem.*, vol. 244, pp. 182–210, 2017.
[29] G. Korotcenkov and B. K. Cho, “Engineering approaches for the improvement of conductometric gas sensor parameters Part 1 . Improvement of sensor sensitivity and selectivity (short survey),” *Sensors Actuators B. Chem.*, vol. 188, pp. 709–728, 2013.
[30] P. T. Moseley, “Progress in the development of semiconducting metal oxide gas sensors : a review,” *Meas. Sci. Technol. Top.*, vol. 28, p. 082001 (15pp), 2017.
[31] J. Cerd *et al.*, “Micromachined twin gas sensor for CO and O 2 quantification based on catalytically modified nano-SnO 2,” *Sensors Actuators B. Chem.*, vol. 114, pp. 881–892, 2006.
[32] R. Godbole, V. Godbole, and S. Bhagwat, “Palladium enriched tungsten oxide thin films : an efficient gas sensor for hazardous gases,” *Eur. Phys. J. B*, vol. 92, no. 78, 2019.
[33] G. Korotcenkov, “Conductometric gas sensors based on metal oxides modified with gold nanoparticles : a review,” *Microchim. Acta*, vol. 183, pp. 1033–1054, 2016.
[34] T. Tesfamichael, C. Piloto, M. Arita, and J. Bell, “Fabrication of Fe-doped WO 3 films for NO 2 sensing at lower operating temperature,” *Sensors Actuators B. Chem.*, vol. 221, no. 2, pp. 393–400, 2015.

[35] N. S. Ramgir *et al.*, "Room temperature H 2 S sensor based on Au modified ZnO nanowires," *Sensors Actuators B. Chem.*, vol. 186, pp. 718–726, 2013.
[36] L. Zhu and W. Zeng, "Room-temperature gas sensing of ZnO-based gas sensor : A review," *Sensors Actuators A. Phys.*, vol. 267, pp. 242–261, 2017.
[37] Q. A. Drmosh, Z. H. Yamani, A. K. Mohamedkhair, A. H. Y. Hendi, and A. Ibrahim, "Room-temperature detection of hydrogen by platinum-decorated tin oxide thin fi lms augmented by heat-treatment," *Vacuum*, vol. 156, pp. 68–77, 2018.
[38] P. J. Kelly and R. D. Arnell, "Magnetron sputtering : a review of recent developments and applications," *Vacuum*, vol. 56, pp. 159–172, 2000.
[39] J. Greene, "Review Article : Tracing the recorded history of thin-film sputter deposition : From the 1800s to 2017," *J. Vac. Sci. Technol.*, vol. A 35, no. 05C204, 2017.
[40] B. Szyszka, M. Vergo, R. Bandorf, and G. Bra, "Magnetron sputtering – Milestones of 30 years," *Vacuum*, vol. 84, pp. 1354–1359, 2010.
[41] I. Chang, S. Woo, M. Hwan, J. Hyung, and Y. Piao, "Characterization of porous Pt films deposited via sputtering," *Appl. Surf. Sci.*, vol. 282, pp. 463–466, 2013.
[42] A. Lacoste, S. Miraglia, and L. Laversenne, "MgH 2 thin films deposited by one-step reactive plasma sputtering," *Int. J. Hydrogen Energy*, vol. 9, pp. 8–15, 2014.
[43] J. Alami, K. Sarakinos, F. Uslu, and M. Wuttig, "On the relationship between the peak target current and the morphology of chromium nitride thin films deposited by reactive high power pulsed magnetron," *J. Phys. D. Appl. Phys.*, vol. 42, no. 1, p. 015304, 2008.
[44] H. Kawasaki, T. Ueda, Y. Suda, and T. Ohshima, "Properties of metal doped tungsten oxide thin films for NO x gas sensors grown by PLD method combined with sputtering process," vol. 100, no. x, pp. 266–269, 2004.
[45] K. H. Nam and J. G. Han, "Reactive magnetron sputtering of thin films : present status and trends," *Thin Solid Films*, vol. 475, pp. 208–218, 2005.
[46] S. Venkataraj, R. Drese, O. Kappertz, and R. Jayavel, "Characterization of Niobium Oxide Films Prepared by Reactive DC Magnetron Sputtering," *Phys. status solidi*, vol. 188, no. 3, pp. 1047–1058, 2001.
[47] L. Lombardo, S. Grassini, M. Parvis, N. Donato, and A. Gullino, "Ethanol breath measuring system," in *IEEE International Symposium on Medical Measurements and Applications - Bari 2020*.
[48] N. Alizadeh, H. Jamalabadi, and F. Tavoli, "Breath Acetone Sensors as Non-Invasive Health Monitoring Systems : A Review," *IEEE Sens. J.*, vol. 20, no. 1, pp. 5–31, 2020.
[49] S. Xu, H. Zhang, L. Qi, and L. Xiao, "Conductometric acetone vapor sensor based on the use of gold-doped three-dimensional hierarchical porous zinc oxide microspheres," *Microchim. Acta*, vol. 186, p. 342, 2019.
[50] X. Li *et al.*, "Design of Au @ ZnO Yolk − Shell Nanospheres with Enhanced Gas Sensing Properties," *Appl. Mater. Interfaces*, vol. 6, pp. 18661–18667, 2014.
[51] F. Hellegouarc, F. Arefi-Khonsari, R. Planade, and J. Amouroux, "PECVD prepared SnO 2 thin films for ethanol sensors," *Sensors Actuators B. Chem.*, vol. 73, pp. 27–34, 2001.
[52] A. Labidi, E. Gillet, R. Delamare, M. Maaref, and K. Aguir, "Ethanol and ozone sensing characteristics of WO 3 based sensors activated by Au and

Pd," *Sensors Actuators B. Chem.*, vol. 120, pp. 338–345, 2006.
[53] B. Sharma, A. Sharma, and J. Kim, "Recent advances on H 2 sensor technologies based on MOX and FET devices : A review," *Sensors Actuators B. Chem.*, vol. 262, pp. 758–770, 2018.
[54] U. C. Ghoshal, "How to Interpret Hydrogen Breath Tests," *J. Neurogastroenterol. Motil.*, vol. 17, no. 3, pp. 312–317, 2011.
[55] R. Abdul, A. Sabirin, J. Zhen, M. R. Field, M. Austin, and K. Kalantar-zadeh, "Nanoporous Nb 2 O 5 hydrogen gas sensor," *Sensors Actuators B. Chem.*, vol. 176, pp. 149–156, 2013.
[56] Z. Wang *et al.*, "Fast and highly-sensitive hydrogen sensing of Nb 2 O 5 nanowires at room temperature," *Int. J. Hydrogen Energy*, vol. 37, no. 5, pp. 4526–4532, 2011.
[57] R. K. Joshi and Æ. S. Krishnan, "Pd Nanoparticles and Thin Films for Room Temperature Hydrogen Sensor," *nanoscale Res. Lett.*, vol. 4, pp. 1191–1196, 2009.
[58] R. S. Gottam, C. Tsai, L. Wang, C. Wang, and C. Lin, "Applied Surface Science Highly sensitive hydrogen gas sensor based on a MoS 2 -Pt nanoparticle composite," *Appl. Surf. Sci.*, vol. 506, p. 144981, 2020.
[59] T. Hübert, L. Boon-brett, G. Black, and U. Banach, "Hydrogen sensors – A review," *Sensors Actuators B Chem.*, vol. 157, pp. 329–352, 2011.
[60] S. Mao, H. Zhou, S. Wu, and J. Yang, "High performance hydrogen sensor based on Pd / TiO 2 composite film," *Int. J. Hydrogen Energy*, vol. 43, no. 50, pp. 22727–22732, 2018.
[61] J. Moon, H. Hedman, M. Kemell, and A. Tuominen, "Hydrogen sensor of Pd-decorated tubular TiO 2 layer prepared by anodization with patterned electrodes on SiO 2 / Si substrate," *Sensors Actuators B. Chem.*, vol. 222, pp. 190–197, 2016.
[62] J. Chen, J. Zhang, M. Wang, and Y. Li, "High-temperature hydrogen sensor based on platinum nanoparticle-decorated SiC nanowire device," *Sensors Actuators B Chem.*, vol. 201, pp. 402–406, 2014.
[63] V. Shroeder and K. Holtappels, "Explosion Characteristics of Hydrogen-Air and Hydrogen-Oxygen Mixtures at Elevated Pressures," 2005.
[64] C. K. Yao, A. Rotbart, J. Z. Ou, K. Kalantar-zadeh, J. G. Muir, and P. R. Gibson, "Modulation of colonic hydrogen sulfide production by diet and mesalazine utilizing a novel gas- profiling technology," *Gut Microbes*, vol. 9, no. 6, pp. 510–522, 2018.
[65] A. Gullino, M. Parvis, E. Angelini, and S. Grassini, "Electrochemical measurements to predict the antifungal properties of nanostructured thin films," in *MeMeA 2018 - 2018 IEEE International Symposium on Medical Measurements and Applications, Proceedings*, 2018.
[66] K. Graf *et al.*, "Surgical site infections-economic consequences for the health care system," *Langenbeck's Arch. Surg.*, vol. 396, no. 4, pp. 453–459, 2011.
[67] D. Méheust, P. Le Cann, and J. P. Gangneux, "Rapid quantification of viable fungi in hospital environments: Analysis of air and surface samples using solid-phase cytometry," *J. Hosp. Infect.*, vol. 83, no. 2, pp. 122–126, 2013.
[68] C. Kuehn *et al.*, "Economic implications of infections of implantable cardiac devices in a single institution," *Eur. J. Cardio-thoracic Surg.*, vol. 37, no. 4, pp. 875–879, 2010.
[69] P. Scopece, A. Viaro, R. Sulcis, I. Kulyk, and A. Patelli, "SiOx - Based Gas Barrier Coatings for Polymer Substrates by Atmospheric Pressure Plasma Jet

Deposition," *plasma Process. Polym.*, vol. 6, no. August, 2009.
[70] F. Fracassi, R. Agostino, F. Palumbo, E. Angelini, S. Grassini, and F. Rosalbino, "Application of plasma deposited organosilicon thin films for the corrosion protection of metals," vol. 175, pp. 107–111, 2003.
[71] B. Jia, Y. Mei, L. Cheng, J. Zhou, and L. Zhang, "Preparation of copper nanoparticles coated cellulose fi lms with antibacterial properties through one-step reduction," *Appl. Mater. Interfaces*, vol. 4, pp. 2897–2902, 2012.
[72] C. C. Trapalis, M. Kokkoris, G. Perdikakis, and G. Kordas, "Study of Antibacterial Composite Cu / SiO 2 Thin Coatings," *J. Sol-Gel Sci. Technol.*, vol. 26, pp. 1213–1218, 2003.
[73] N. Cioffi *et al.*, "Copper Nanoparticle / Polymer Composites with Antifungal and Bacteriostatic Properties," *Chem. Mater.*, vol. 17, no. 7, pp. 5255–5262, 2005.
[74] H. Tapiero, D. M. Townsend, K. D. Tew, and F. Chase, "Trace elements in human physiology and pathology. Copper," *Biomed. Pharmacother.*, vol. 57, pp. 386–398, 2003.
[75] M. Kawashita, S. Tsuneyama, F. Miyaji, T. Kokubo, H. Kozuka, and K. Yamamoto, "Antibacterial silver-containing silica glass prepared by sol - gel method," *Biomaterials*, vol. 21, pp. 393–398, 2000.
[76] P. Innocenzi, "Methyltriethoxysilane-derived coatings for optical applications," *Proceeding spie*, 1994.
[77] S. Gerullis *et al.*, "Thin antimicrobial silver , copper or zinc containing - SiO x films on wood polymer composites (WPC) applied by atmospheric pressure plasma chemical vapour deposition (APCVD) and sol – gel technology," *Eur. J. Wood Wood Prod.*, vol. 76, no. 1, pp. 229–241, 2018.
[78] O. Akhavan and E. Ghaderi, "Cu and CuO nanoparticles immobilized by silica thin fi lms as antibacterial materials and photocatalysts," *Surf. Coat. Technol.*, vol. 205, no. 1, pp. 219–223, 2010.
[79] L. Bedel, C. Cayron, M. Jouve, and F. Maury, "Embedded layer of Ag nanoparticles prepared by a combined PECVD/PVD process producing SiO xC y-Ag nanocomposite thin films," *Nanotechnology*, vol. 23, no. 1, 2012.
[80] A. Daniel, C. Le Pen, C. Archambeau, and F. Reniers, "Use of a PECVD – PVD process for the deposition of copper containing organosilicon thin films on steel," *Appl. Surf. Sci. J.*, pp. 82–85, 2009.
[81] M. Parvis, F. Ferraris, S. Grassini, E. Angelini, and D. Fulginiti, "Biodegradable metallic materials : a measuring approach to predict the corrosion rate," in *IEEE international symposium in medical measurements and applications*, 2014.
[82] M. S. M. Yeganeh, "Investigation of corrosion behaviour of nanostructured copper thin film produced by radio frequency sputtering," *Micro Nano Lett. IET*, vol. 5, no. 2, pp. 70–75, 2010.
[83] S. Grassini, E. Angelini, M. Parvis, S. Corbellini, and M. Ishtaiwi, "Electrochemical characterization of magnesium bioabsorbable implants," 2014.
[84] S. Feliu, "Electrochemical Impedance Spectroscopy for the Measurement of the Corrosion Rate of Magnesium Alloys : Brief Review and Challenges," *Metals (Basel).*, vol. 10, no. 6, p. 775, 2020.
[85] J. J. van Hapert, *Hopping Conduction and Chemical Structure: a study on Silicon Suboxides*, vol. Ultrecht U. .
[86] M. Song *et al.*, "Recent advances in biodegradation controls over Mg alloys

for bone fracture management : A review," *J. Mater. Sci. Technol.*, vol. 35, no. 4, pp. 535–544, 2019.
[87] D. W. Bratzler, P. M. Houck, and S. Infection, "Antimicrobial prophylaxis for surgery : an advisory statement from the National Surgical Infection Prevention Project," *Am. J. Surg.*, vol. 189, pp. 395–404, 2005.
[88] A. N. Neely and M. M. Orloff, "Survival of Some Medically Important Fungi on Hospital Fabrics and Plastics," *J. Clin. Microbiol.*, vol. 39, no. 9, pp. 3360–3361, 2001.
[89] T. Kraus, S. F. Fischerauer, A. C. Hänzi, P. J. Uggowitzer, J. F. Löffler, and A. M. Weinberg, "Magnesium alloys for temporary implants in osteosynthesis : In vivo studies of their degradation and interaction with bone," *Acta Biomater.*, vol. 8, no. 3, pp. 1230–1238, 2012.
[90] N. T. Kirkland, N. Birbilis, and M. P. Staiger, "Assessing the corrosion of biodegradable magnesium implants : A critical review of current methodologies and their limitations," *Acta Biomater.*, vol. 8, no. 3, pp. 925–936, 2012.
[91] M. Peron, J. Torgersen, and B. Filippo, "Mg and Its Alloys for Biomedical Applications : Mechanical Failure," *Metals (Basel).*, vol. 7, no. 7, 2017.
[92] Z. Li, X. Gu, S. Lou, and Y. Zheng, "The development of binary Mg e Ca alloys for use as biodegradable materials within bone," *Biomaterials*, vol. 29, pp. 1329–1344, 2008.
[93] M. Meischel *et al.*, "Bone-implant degradation and mechanical response of bone surrounding Mg-alloy implants," *J. Mech. Behav. Biomed. Mater.*, vol. 71, no. August 2016, pp. 307–313, 2017.
[94] J. Lee, H. Han, K. Han, J. Park, H. Jeon, and M. Ok, "Long-term clinical study and multiscale analysis of in vivo biodegradation mechanism of Mg alloy," *Proc. Natl. Acad. Sci. U. S. A.*, vol. 113, no. 3, 2016.
[95] M. Dharam, Persaud-Sharma; Anthony, "Biodegradable Magnesium Alloys: A Review of Material Development and Applications," *J. Biomater. Tissue Eng.*, vol. 12, no. 1, pp. 25–39, 2012.
[96] D. Dvorsky *et al.*, "High strength AM50 magnesium alloy as a material for possible stent application in medicine," *Mater. Technol.*, vol. 34, no. 14, pp. 838–842, 2019.
[97] L. Mao *et al.*, "Enhanced biocompatibility and long-term durability in vivo of Mg-Nd-Zn-Zr alloy for vascular stent application," *J. Alloys Compd.*, vol. 720, pp. 245–253, 2017.
[98] M. P. Staiger, A. M. Pietak, J. Huadmai, and G. Dias, "Magnesium and its alloys as orthopedic biomaterials : A review," *Biomaterials*, vol. 27, pp. 1728–1734, 2006.
[99] A. Sato, Y. Shimizu, Y. Imai, T. Mukai, and A. Yamamoto, "Initial organ distribution and biological safety of Mg 2 + released from a Mg alloy implant," 2018.
[100] F. Witte, V. Kaese, H. Haferkamp, E. Switzer, and A. Meyer-lindenberg, "In vivo corrosion of four magnesium alloys and the associated bone response," *Biomaterials*, vol. 26, pp. 3557–3563, 2005.
[101] A. Hartwig, "Role of magnesium in genomic stability," *Mutat. Res. / Fundam. Mol. Mech. Mutagen.*, vol. 475, pp. 113–121, 2001.
[102] J. Vormann, "Magnesium : nutrition and metabolism," *Mol. Aspects Med.*, vol. 24, pp. 27–37, 2003.
[103] W. R. Zhou, Y. F. Zheng, M. A. Leeflang, and J. Zhou, "Mechanical property

, biocorrosion and in vitro biocompatibility evaluations of Mg – Li –(Al)–(RE) alloys for future cardiovascular stent application," *Acta Biomater.*, vol. 9, no. 10, pp. 8488–8498, 2013.
[104] M. Ascencio, M. Pekguleryuz, and S. Omanovic, "An investigation of the corrosion mechanisms of WE43 Mg alloy in a modified simulated body fluid solution : The effect of electrolyte renewal," *Corros. Sci.*, vol. 91, pp. 297–310, 2015.
[105] N. Li *et al.*, "Comparative study on corrosion behaviour of pure Mg and WE43 alloy in static , stirring and flowing Hank ' s solution," *Corros. Eng. Sci. Technol.*, vol. 47, no. 5, pp. 346–351, 2013.
[106] X. Gu *et al.*, "In vitro and in vivo studies on as-extruded Mg- 5 . 25wt .% Zn-0 . 6wt .% Ca alloy as biodegradable metal," *Sci. CHINA Mater.*, vol. 61, no. January, pp. 619–628, 2018.
[107] H. R. Bakhsheshi-rad, M. H. Idris, M. R. Abdul-kadir, A. Ourdjini, M. Medraj, and M. Daroonparvar, "Mechanical and bio-corrosion properties of quaternary Mg – Ca – Mn – Zn alloys compared with binary Mg – Ca alloys," *Mater. Des.*, vol. 53, pp. 283–292, 2014.
[108] L. Yang, Y. Huang, F. Feyerabend, R. Willumeit, K. U. Kainer, and N. Hort, "Influence of ageing treatment on microstructure , mechanical and bio-corrosion properties of Mg – Dy alloys," *J. Mech. Behav. Biomed. Mater.*, vol. 13, pp. 36–44, 2012.
[109] X. Zhao, L. Shi, and J. Xu, "Mg – Zn – Y alloys with long-period stacking ordered structure : In vitro assessments of biodegradation behavior," *Mater. Sci. Eng. C*, vol. 33, no. 7, pp. 3627–3637, 2013.
[110] Q. Qu, J. Ma, L. Wang, L. Li, W. Bai, and Z. Ding, "Corrosion behaviour of AZ31B magnesium alloy in NaCl solutions saturated with CO2," *Corros. Sci.*, vol. 53, no. 4, pp. 1186–1193, 2011.
[111] W. Bai, J. Yu, Y. Yang, Y. Ye, J. Guo, and Y. Zhang, "Effect of CO 2 Saturation on the Corrosion Behaviour of AZ31B Magnesium Alloy in Na 3 PO 4 Solutions," *Int. J. Electrochem. Sci.*, vol. 8, pp. 3441–3453, 2013.
[112] M. Esmaily, J. Svensson, M. Halvarsson, L. Nyborg, Y. Cao, and L. Johansson, "NaCl-Induced Atmospheric Corrosion of the MgAl Alloy AM50-The Influence of CO 2," *J. Electrochem. Soc.*, vol. 161, no. 6, pp. 277–287, 2014.
[113] V. Wagener and S. Virtanen, "Protective layer formation on magnesium in cell culture medium," *Mater. Sci. Eng. C*, vol. 63, pp. 341–351, 2016.
[114] M. Esmaily *et al.*, "Fundamentals and advances in magnesium alloy corrosion," *Prog. Mater. Sci.*, vol. 89, pp. 92–193, 2017.
[115] Z. Shi, M. Liu, and A. Atrens, "Measurement of the corrosion rate of magnesium alloys using Tafel extrapolation," *Corros. Sci.*, vol. 52, no. 2, pp. 579–588, 2010.
[116] A. D. King, N. Birbilis, and J. R. Scully, "Electrochemical Measurement of Magnesium Corrosion Rates ; a Combined Impedance , Mass-Loss and Hydrogen Collection Study," *Electrochim. Acta*, vol. 121, pp. 394–406, 2014.
[117] A. Atrens, M. Liu, N. Ishida, and Z. Abidin, "Corrosion mechanism applicable to biodegradable magnesium implants ☪," *Mater. Sci. Eng. B*, vol. 176, no. 20, pp. 1609–1636, 2011.
[118] R. Arrabal, E. Matykina, F. Viejo, P. Skeldon, and G. E. Thompson, "Corrosion resistance of WE43 and AZ91D magnesium alloys with

phosphate PEO coatings," *Corros. Sci.*, vol. 50, pp. 1744–1752, 2008.
[119] T. Rzychon and A. Kielbus, "Microstructure of WE43 casting magnesium alloy," *J. Achiev. Mater. Manuf. Eng.*, vol. 21, no. 1, pp. 31–34, 2006.
[120] A. E. Coy, F. Viejo, P. Skeldon, and G. E. Thompson, "Susceptibility of rare-earth-magnesium alloys to micro-galvanic corrosion," *Corros. Sci.*, vol. 52, no. 12, pp. 3896–3906, 2010.
[121] M. Esmaily *et al.*, "A detailed microstructural and corrosion analysis of magnesium alloy WE43 manufactured by selective laser melting," *Addit. Manuf.*, vol. 35, no. May, p. 101321, 2020.
[122] H. R. Bakhsheshi-rad, M. Abdellahi, E. Hamzah, A. Fauzi, and M. Bahmanpour, "Modelling corrosion rate of biodegradable magnesium-based alloys : The case study of Mg-Zn-RE- x Ca (x ¼ 0 , 0 . 5 , 1 . 5 , 3 and 6 wt %) alloys," *J. Alloys Compd.*, vol. 687, pp. 630–642, 2016.